MICROSTRUCTURE OF PEROVSKITE OXIDE THIN FILMS GROWN ON MISCUT/SMALL LATTICE-MISMATCHED SUBSTRATES

by

Yanbin Chen

A dissertation submitted in partial fulfillment
of the requirements for the degree of
Doctor of Philosophy
(Materials Science and Engineering)
in The University of Michigan
2008

Doctoral Committee:

Professor Xiaoqing Pan, Chair
Professor Lumin Wang
Professor John W Halloran
Professor Michael D Thouless
Assistant Professor Anton Van der Ven

To my wife Xueqin Han, parents and parents-in-law

ACKNOWLEDGEMENTS

First I'd like to thank my thesis advisor, Professor Xiaoqing Pan, for the financial support, research guidance, and spiritual encouragement throughout my graduate study at the University of Michigan. I am grateful to Professor C. B. Eom for providing the samples studied in this thesis, and his instructive suggestions. I would also like to express my gratitude to the other committee members, Professor Lumin Wang, Professor John Halloran, Professor Michael Thouless and Professor Anton Van der Ven, for their helpful advice on my thesis writing and for sharing their extensive knowledge in materials science.

Thanks go to Dr. K. Sun and Dr. J. Mansfield for all their help on use of TEM at EMAL. Thanks to Professor C. B. Eom, Dr. D. M. Kim, Mr. C. M. Folkman, Dr. H. W. Jong for their kind support of the thin films growth which were studied in this thesis. The help from my previous and current colleagues: Dr. W. Tian (currently in Seagate Inc.), Dr. H. P. Sun (currently in EMAL), Mr. A. Allenic, Ms. W. Guo, Mr. M. B. Katz, Mr. C. T. Nelson and Mr. O. K. Ezekoye are greatly appreciated as well.

TABLE OF CONTENTS

LIST OF TABLES

Table

LIST OF FIGURES

Figure

CHAPTER 1

INTRODUCTION

Perovskite oxides exhibit a wide range of physical properties, such as high dielectric, piezoelectric, pyroelectric, ferroelectric/multiferroic, non-linear optical, ferromagnetic, colossal/giant magnetic resistant and high-temperature superconductoring properties.[1] Some examples are outlined in Table 1.1. Because of the wide spectrum of electronic, optical and magnetic properties of perovskite oxides, these oxides and their hetero-structures / super-lattices will be core-elements of next generation functional devices for sensors, signal processing, electric/optical circuits and energy conversion.[2-5]

With the minimization in the electronic devices, perovskite oxides in thin film morphology are a vital field of research.[3-5] Normally the thickness of oxide thin films is of the sub-micrometer and nano-meter scale. Nano-meter scale oxides could have different properties with respect to their bulk counterparts, because the size effects are dominant at the nano-meter scale.[6-8] It is of equal importance to tailor physical properties through dedicated growth control during thin film deposition. Compared with bulk materials, perovskite oxides are grown on commercially available single crystalline substrates by physical (such as pulsed laser deposition, molecular-beam epitaxial) and chemical methods (for example, metal-organic chemical vapor deposition, sol-gel deposition).[9] Substrates have previously been treated as inert templates to accommodate atoms escaped from vapor/plasma. Currently, however, substrates are being exploited to engineer the physical properties in perovskite oxide thin films.[10] Until now, two-type of the special substrates have been used to control microstructures and physical properties of perovskite oxide thin films. One method uses small lattice-matched substrates. Normally the single crystalline materials must be synthesized as substrates by the Czochralski method.[11,12] The aim of this application is to minimize the misfit strain between the substrates and thin films. The misfit strain comes from the different lattice parameters and the difference in thermal expansion between films and substrates. The other method uses the intentional-miscut commercial substrates. Miscut leads to a series of atomic steps on the substrate surface.[1,5,16] These atomic steps provide the initial growth sites, which probably changes the growth mode in thin film deposition. This, in turn, could improve the physical properties in perovskite oxide thin films.[13-17] The artificially engineered perovskite oxide thin films have chemical and structural variance in the nano-meter scale, which requires precise characterization at a corresponding scale. Conventional and analytical transmission electron microscopy are indispensable for charactering artificially engineered perovskite oxide thin films at the atomic scale.[2,4] The overall objective of this thesis is to study the microstructure of strain relaxation of $BaTiO_3$ thin films grown on two small lattice-mismatched substrates ($GdScO_3$ and $DyScO_3$ substrates), the ferroelectric domain structures of $BiFeO_3$ thin films grown on low (<1°) and high-angle miscut (miscut angle 4°) $SrTiO_3$ substrates, as well as crystallographic domains of $PrScO_3$ thin films grown on low (<1°) and high-angle miscut $SrTiO_3$ substrates using *state-of-the-art* transmission electron microscopy, and then to correlate the structure-property relationships in these oxide thin films.

During the past few years, multiferroics (or called as magneto-electric materials/magnetically ordered ferroelectric materials) have received much attention in materials science community.[18-22] Multiferroic materials show spontaneous electric polarization (electric dipole) and magnetization (electric net spin) simultaneously. The tremendous interest in this field stems from both potential device applications and fundamental research. One potential application of multiferroic materials is their development into novel magnetic-controlled or electric-controlled memory devices.[18] In the fundamental research field, multiferroic materials provide good systems to study the physical coupling mechanism between ferroelectric spontaneous polarization and ferromagnetic magnetization in condensed matter physics.[18,19] Until now, the studies of single phase multiferroic materials have focused on $BiFeO_3$ and $BiMnO_3$.[18-20] $BiFeO_3$ is a typical multiferroic material at room temperature, which becomes ferroelectric below 1200 K and G-type anti-ferromagnetic below 780 K.[20,21] As in ferroelectric thin films, extrinsic effects (such as strain clamping and ferroelectric domains) are critical to the measured physical properties in multiferroic materials.[18] In this thesis, the ferroelectric domain structure in $BiFeO_3$ thin films is engineered by means of miscut $SrTiO_3$ substrates. The domain structure and interfacial structure in $BiFeO_3$ were studied by conventional and analytical transmission electron microscopy. It was found that different domain structures lead to different ferroelectric properties in $BiFeO_3$ thin films.

Recently, new single crystalline rare-earth scandates (such as $GdScO_3$ and $DyScO_3$) have been grown by the Czochralski method for use as substrates.[23-25] Crystallographic study has shown that $GdScO_3$ and $DyScO_3$ substrates provide compressive strain to $BaTiO_3$ thin films, and lattice mismatch between $GdScO_3$ ($DyScO_3$)

and $BaTiO_3$ is as small as 0.56 % and 1.2 %, respectively.[23] In addition, recent *in-situ* x-ray diffraction has shown that the difference in thermal expansion between these two materials and $BaTiO_3$ is relatively small.[24] The average thermal expansion coefficients of $BaTiO_3$, $GdScO_3$ and $DyScO_3$ are 12.7, 8.4 and 10.9 ppm/K, respectively. Coherent $BaTiO_3$ thin films with a $SrRuO_3$ bottom electrode layer grown on $GdScO_3$ and $DyScO_3$ substrates show enhancement of Curie temperature and spontaneous electric polarization.[25] Transmission electron microscopy and thermodynamic calculation are applied to study the strain relaxation in $BaTiO_3/SrRuO_3$ hetero-structure grown on $GdScO_3$, $DyScO_3$ and $SrTiO_3$ substrates.

Unlike $GdScO_3$ and $DyScO_3$ substrates, $PrScO_3$, another rare-earth scandate, exerts tensile stress on $BaTiO_3$ thin film that is grown above. However, $PrScO_3$ is difficult to synthesize using the conventional Czochralski method due to a melting temperature of 2100 °C and non-congruent behavior at the melting temperature.[26] Therefore, a strain-relaxed, single-domain $PrScO_3$ template is an alternative to a single crystal $PrScO_3$ substrate. In this thesis, strain relaxed $PrScO_3$ templates were grown on low ($<1°$) and high-angle ($\geq 1°$) miscut $SrTiO_3$ substrates using pulsed laser deposition. The domain structure, interface structure and defect structure in $PrScO_3$ thin films were characterized by electron diffraction and high resolution transmission electron microscopy.

This thesis is organized in the following way. In chapter 2, experimental methods including transmission electron microscopy, TEM sample preparation and deposition method are described in detail. In chapter 3, the microstructures of $BiFeO_3$ thin films grown on low (miscut angle $<1°$) and high-angle (miscut angle is 4°) miscut $SrTiO_3$

substrates are presented. The different domain structure, in turn, leads to different ferroelectric properties of $BiFeO_3$ thin films. In chapter 4, strain relaxation of the $BaTiO_3$/$SrRuO_3$ hetero-structure grown on compressive-type $GdScO_3$, $DyScO_3$ and $SrTiO_3$ substrates is studied. The different strain relaxation in $BaTiO_3$ with different thicknesses grown on $GdScO_3$, $DyScO_3$ and $SrTiO_3$ substrates were observed. Experimental observation is discussed by means of thermodynamics critical thickness theory. In chapter 5, the crystallographic domain structures, interfacial structure and defect structure of $PrScO_3$ templates grown on low (miscut angle <1°) and high-angle (miscut angle ≥1°) miscut $SrTiO_3$ substrates were studied. Finally, a summary of current work and proposals for future work are presented in chapter 6.

Table 1.1 Examples of perovskite oxides and their physical properties. The materials studied in this thesis are highlighted by italicization

Materials	Physical properties
High dielectric constant (high-k[*]) material- $PrScO_3$[27]	ε_r=29 (Frequency=300kHz)
Ferroelectric material- $BaTiO_3$[1]	P_r=25.0 μC/cm^2
Multiferroic material- $BiFeO_3$[24]	P_r=75μC/cm^2 and M=0.04 μ_B
Conductor- $SrRuO_3$[5]	ρ=210 μΩ·cm (Temperature=300K)
High-temperature superconductor-$YBa_2Cu_3O_{7-x}$[1]	ρ=0 (Temperature<92K)
Colossal magnetoresistant-(La,Sr)MnO_3 [5]	$\Delta R/R_H > 10^4$ (Temperature=6T)
Ferrimagnet-$PrFeO_3$[5]	M_s=0.04 μ_B

[*] High-*k* materials in here represent the materials which have larger dielectric constant than SiO_2. The amorphous SiO_2 has the dielectric constant of 4.[3]

References:

[1] M. P. Marder, *Condensed Matter Physics* (John Wiley & Sons, Inc., New York, 2000).

[2] S. A. Chambers, “Epitaxial growth and properties of thin film oxides,” Surface Science reports, **39**, 105 (2000).

[3] G. D. Wilk, R. M. Wallace, J. M. Anthony, “High-k gate dielectrics: Current status and materials properties considerations,” J. Appl. Phys. **89**, 5243 (2001).

[4] D. G. Schlom, J. H. Haeni, J. Lettieri, C. D. Theis, W. Tian, J. C. Jiang, X. Q. Pan, “Oxide nano-engineering using MBE,” Mater. Sci. & Engin. B. **87**, 282 (2001).

[5] D. P. Norton, “Synthesis and properties of epitaxial electronic oxide thin-film materials,” Materials Science and Engineering R **43**, 139 (2004).

[6] W. D. Si, X. X. Xi, “Epitaxial-strain-induced insulator-superconductor transition in undoped and lightly doped La_2CuO_4,” Appl. Phys. Lett., **78**, 240 (2001).

[7] T. Zhao, Z. H. Chen, F. Chen, W. S. Shi, H. B. Lu, and G. Z. Yang, “Enhancement of second-harmonic generation in $BaTiO_3/SrTiO_3$ superlattice,” Phys. Rev. B, **60**, 1697 (1999).

[8] L. M. Wang, “Anomalous hall effect in $La_{0.7}Sr_{0.3}MnO_3/SrTiO_3$ superlattices: hopping transport and a probe of dimensionality” Phys. Rev. Lett., **96**, 077203 (2006).

[9] Editors: R. W. Schwartz, P. C. Mclntyre, Y. Miyasaka, S. R. Summerfelt, and D. Wouters, Ferroelectric Thin Films VIII, Materials Research Society Symposium Proceedings, **596** (2000).

[10] H. U. Hbermeier, “Substrate surface engineering for functional ceramic thin films growth,” J. Electro-ceramics, **13**, 23 (2004).

[11] Z. R. Dai, S. Y. Son, B. S. Kim, D. K. Choi, and F. S. Ohuchi, “Electrically conducting oxide thin films of $(Sr,Ca)RuO_3$ and structural compatibility with $(Ba,Sr)TiO_3$,” Mater. Rese. Bull., **34**, 933 (1999).

[12] B. C. Chakoumakos, D. G. Schlom, M. Urbanik, and J. Luine, “Thermal expansion of $LaAlO_3$ and $(La,Sr)(Al,Ta)O_3$, substrate materials for superconducting thin-film device,” J. Appl. Phys., **83**, 1979 (1998).

[13] J. C. Jiang, W. Tian, X. Q. Pan, Q. Gan, and C. B. Eom, “Domain structure of epitaxial $SrRuO_3$ thin films on miscut (001) $SrTiO_3$ substrates,” Appl. Phys. Lett., **72**, 2963 (1998).

[14] M. J. Zhuo, Y. L. Zhu, X. L. Ma, and H. B. Lu, “Single [101]-oriented growth of $La_{0.9}Sr_{0.1}MnO_3$ films on vicinal $SrTiO_3$ (001) substrates,” Appl. Phys. Lett., **88**, 071905 (2006).

[15] D. Vassiloyannis, “The effect of substrate vicinal offcut on the morphology and physical properties of $YBa_2Cu_3O_{7-\delta}$ thin films,” IEEE transactions on Applied Superconductivity, **9**, 1638 (1999).

[16] C. P. Flynn, J. A. Eades, “Structural variants in heteroepitaxial growth,” thin solid films, **389**, 116 (2001).

[17] J. C. Nie, H. Yamasaki, Y. Nakagawa, K. D. Bagarinao, M. Murugesan, H. Obara, and Y. Mawatari, “Microcrack-free epitaxy of thick $YBa_2Cu_3O_{7-\delta}$ films on vicinal r-cut sapphire buffered with CeO_2,” Appl. Phys. Lett., **86**, 192507 (2005).

[18] M. Fiebig, “Revival of the magnetoelectric effect,” J. Phys. D: Appl. Phys., **38**, R123 (2005).

[19] R. Ramesh, and N. A. Spaldin, “Multiferroics: progress and prospects in thin films,” Nature materials, **6**, 21 (2007).

[20] C. Michel, J. M. Moreau, G. D. Achenbach, R. Gerson, and W. J. James, “The atomic structure of $BiFeO_3$,” Solid State comm., **7**, 701 (1969).

[21] C. Blaauw, and F. V. D. Woude, “Magnetic and structural properties of $BiFeO_3$,” J. Phys. C, **6**, 1422 (1973).

[22] Y. H. Chu, Q. Zhan, L. W. Martin, M. P. Cruz, P. L. Yang, G. W. Pabst, F. Zavaliche, S. Y. Yang, J. X. Zhang, L. Q. Chen, D. G. Schlom, I. N. Lin, T. B. Wu, and R. Ramesh, “Nanoscale domain control in multiferroic $BiFeO_3$ thin films,” Adv. Mater. (Weinheim, Ger.), **18**, 2307 (2006).

[23] J. Schubert, O. Trithaveesak, A. Petraru, C. L. Jia, R. Recker, P. Reiche, and D. G. Schlom, “Structural and optical properties of epitaxial $BaTiO_3$ thin films grown on $GdScO_3$ (110),” Appl. Phys. Lett., **82**, 3460 (2003).

[24] M. D. Miegalski, J. H. Haeni, S. T. Mckinstry, D. G. Schlom, C. D. Brandle, and A. J. V. En. Graitis, “Thermal expansion of the new perovskite substrates $DyScO_3$ and $GdScO_3$,” J. Mater. Res., **20**, 952 (2005).

[25] K. J. Choi, M. biegalski, Y. L. Li, A. Sharan, J. Schubert, R. Uecker, P. Reiche, Y. B. Chen, X. Q. Pan, V. Gopalan, L. Q. Chen, D. G. Schlom, and C. B. Eom,

"Enhancement of ferroelectricity in strained $BaTiO_3$ thin films," Science, **306**, 1005 (2004).

[26] C. M. Folkman, R. R. Das, C. B. Eom, Y. B. Chen, and X. Q. Pan, "Single domain strain relaxed $PrScO_3$ template on miscut substrates," Appl. Phys. Lett., **89**, 221904 (2006).

[27] H. M. Christen, G. E. Jellison, Jr., I. Ohkubo, S. Huang, M. E. Reeves, E. Cicerrella, J. L. Freeouf, Y. Jia, and D. G. Schlom, "Dielectric and optical properties of epitaxial rare-earth scandate films and their crystallization behavior," Appl. Phys. Lett., **88**, 262906 (2006).

CHAPTER 2

EXPERIMENTAL

2.1. Conventional and analytical transmission electron microscopy

The first transmission electron microscope (TEM) was built by Knoll and Ruska in the early 1930s.[1] The underlying principle of TEM is that the electron is a type of waves, which has wave properties similar to an optical wave. After an electron wave transmits through objectives whose sizes are of the same order of magnitude as the electron wave length, interference and diffraction will occur among the transmitted waves. In addition, a combination of magnetic coils can be used to focus the electron beam. Therefore, a TEM consists of an electron gun and an assembly of electron lenses. TEM has many similarities to an optical microscope.[1] A schematic of the details of microscope and the corresponding ray paths can be found in Hirsch's classic book.[2] The electron microscope is currently a well-established research tool in the materials science community.

Conventional TEM comprises diffraction contrast imaging and electron diffraction. By means of imaging and diffraction, we can study the morphology, planar defects (e.g. ferroelectric/ferromagnetic domain walls, stacking faults), line defects (e.g. screw and edge dislocations) and crystal structures in thin foils with electron transparent areas.[2] Normally, computer-based electron diffraction simulation software (such as Crystalkit or EMS software) is needed to analyze electron diffraction patterns.[3]

Compared with conventional TEM, analytical TEM comprises many tools for structural and chemical characterization of electron transparent thin foils beyond the diffraction contrast and electron diffraction used in conventional TEM.[1,4,5] The chemical analysis in analytical TEM is based on many analytical spectroscopic methods, such as x-ray energy dispersive spectroscopy (EDS), electron energy loss spectroscopy (EELS) and scanning transmission electron microscopy (STEM). The principle of these spectroscopic methods is based on the interaction between the ultra-high speed electron beam and thin foil materials. The interaction generates many useful signals, such as characteristic x-ray generation, Auger electron emission, secondary electron and characteristic electroluminescence. These signals can be used to obtain chemical information about the samples in question. One more interesting point is that in STEM mode, the nano-meter scale electron probe can be formed by precisely controlled electric circuits. The probe is then scanned across the electron transparent thin foils. Combining the aforementioned spectroscopic techniques (such as EDS or EELS) under STEM mode, chemical analysis at the nano-meter scale in thin foil materials is possible. In other word, chemical analysis with spatial resolution at the nano-meter scale can be realized with *state-of-the-art* STEM. Currently, analytical TEM is an indispensable tool in characterization at atomic scale for many materials. An introduction to the basic principle of analytical TEM and examples studied by analytical TEM can be found in the references.[1,4,5,6]

2.2. Thin film growth

All the thin films studied in this thesis were synthesized by Professor Chang-Beom Eom’s group at The University of Wisconsin-Madison in Madison. The perovskite oxide thin films studied in this thesis were grown by either pulsed laser deposition or high-angle offset radio frequency sputtering.

Because the $BiFeO_3$ and $PrScO_3$ thin films studied in this thesis were grown on miscut substrates, it is necessary to discuss the surface conditions of the miscut substrates. Physically, the surfaces of the substrates are not atomically flat. The miscut angle in commercially available substrates is less than 1° (the tolerance of cutting process is less than 1° in industry). There are many steps, terraces and self-organized dimers on the substrate surfaces.[7,8] Characterization of these features is a major great work in the surface science community. However the distribution of atomic steps and terraces are not homogeneous in unintentionally miscut substrates. In contrast to unintentionally miscut substrates, the cutting angle in miscut substrates is normally larger than 1°. Miscut forms a series of parallel atomic steps on the substrate surfaces. [7,8] One of step is illustrated in figure 2.1. There is a simple linear relationship between the height of atomic steps and the terrace length. The ratio of the step height to the terrace length may be obtained from the tangent of the miscut angle. When the miscut angle is smaller than 5°, the tangent of the miscut angle can be approximated as miscut angle α ($\tan(\alpha)\approx\alpha$, angle α must be written in radians). Then relationship between step height h and terrace length L is: $h/L=\tan(\alpha)\approx \alpha$ if α is smaller than 5°. The aforementioned surface morphology on vicinal substrates has been observed by atomic force microscopy (AFM).[7,8] In contrast to the growth of thin films on unintentionally miscut substrates, parallel atomic steps on the miscut substrates probably change the growth mode from two/three-dimensional to step-flow growth in thin films deposition.[8] Previous studies have corroborated that the dominant growth mode in $SrRuO_3$ grown on miscut $SrTiO_3$ substrates is step-flow growth.[8] However, the real process of growth mode change are kinetic controlled, many external factors affect the growth details. Step-flow growth is one of the limiting cases. In this case, the adatom diffusion lengths at growth temperature and pressure are long compared to the mean terrace width on the surface. Then adatom condensation will occur preferentially on steps rather than on terraces. Step flow leads to step-step annihilation and a gradual reduction in step density with increase films thickness.[7,10] From this simplified case, we can see that growth mode in thin film grown on miscut substrate is far from clear. Thus further study for growth mode change on vicinal substrates, such as via *in situ* scanning tunneling microscopy (STM) or reflection high-energy electron diffraction (RHEED) under different temperatures and pressures, is needed.[7]

The background of $BiFeO_3$, $BaTiO_3$ and $PrScO_3$ study was discussed at the literature review part in corresponding chapters. Here we focused on introducing of crystal structures and growth details of these thin films. The crystallographic information of these film and substrate materials is given in tables 2.1 and 2.2, respectively.[7,9] It can be seen that though there are different oxygen octahedron distortions in these materials, they can all be viewed as pseudo-cubic perovskite structures. By means of the pseudo-cubic setting, it is easy to describe defect structures in these materials.

$BiFeO_3$ thin films with thicknesses ranging from 200 nm to 1000 nm were deposited by high-rate off-axis sputtering on 0.8° and 4° miscut (001) $SrTiO_3$ substrates with 100 nm $SrRuO_3$ bottom electrodes.[11] The substrate was miscut along the [010] direction. $SrRuO_3$ bottom electrodes were synthesized by a 90° off-axis sputtering technique.[11] A stoichiometric composite target was used during the growth. $SrRuO_3$ films were deposited at an operating pressure of 200 mTorr (60 % Ar and 40% O_2) and a temperature of 680 °C. After deposition, the $SrRuO_3$ films were cooled down to room temperature under an oxygen pressure of 300 Torr. The $BiFeO_3$ layers were also grown by 90° off-axis radio-frequency (rf) magnetic sputtering. To compensate for Bi volatilization from the films, 5% excess Bi_2O_3 (55% Bi_2O_3 and 45% Fe_2O_3 composite) targets were used in the rf sputtering. During the $BiFeO_3$ film deposition, the substrate was maintained at 600 °C with an oxygen pressure of 400 mTorr. The $BiFeO_3$ films were also cooled down to room temperature under an oxygen pressure of 300 Torr.

During the growth of the $BaTiO_3/SrRuO_3$ hetero-structure on $GdScO_3$ and $DyScO_3$ substrates, $SrRuO_3$ electrodes with different thicknesses were grown by off-axis high-rate rf magnetic sputtering as well. $BaTiO_3$ layers of different thicknesses were deposited at 700 °C and 250 mTorr O_2 atmospheres by pulsed laser deposition with a KrF excimer laser.[12] The wavelength of laser and pulse repetition are 248 nm and 5 Hz, respectively. The laser energy density during the growth is 3.3 J/cm^2. The $BaTiO_3$ thin films were cooled down to room temperature under an oxygen pressure of 300 Torr.

$PrScO_3$ thin films were grown by pulsed laser deposition on (001) miscut $SrTiO_3$ and $(LaAlO_3)_{0.3}$-$(Sr_2AlTaO_3)_{0.7}$ (LSAT) substrates.[13] Substrate miscut was toward [010] in the in-plane with the miscut angles of 0.2°, 1°, 2° and 4°. The miscut angle of LSAT is 2°. The surfaces of the $SrTiO_3$ substrates were TiO_2 terminated using a special etching method.[13] The $PrScO_3$ layers were synthesized by a direct or two-step growth method. In the two-step growth procedure, a 30 nm $PrScO_3$ buffer layer was deposited at 900 °C and 250 mTorr O_2 atmospheres using pulsed laser deposition with KrF excimer laser. The parameters of laser are: the wavelength of the laser and pulse repetition were 248 nm and 5 Hz, respectively. The laser energy density during the growth was 3.3 J/cm^2. This 30 nm $PrScO_3$ buffer layer was annealed *ex situ* at 1200 °C in air for one hour to improve the crystalline quality. Finally, the 100 nm $PrScO_3$ thick film was deposited using the same procedure that is used to grow 30nm buffer layer. In the direct growth method, $PrScO_3$ thin films with thickness of 130 nm were deposited on substrates by pulsed laser deposition using the above-mentioned conditions.[13]

2.3. Microstructure characterization and TEM sample preparation

All TEM studies were carried out on a high-resolution JEOL 3011 microscope operated at 300 kV with optical point-to-point resolution of 0.17 nm, an analytical JEOL 2010F microscope equipped with a energy dispersion spectroscopy (EDS) detector and an electron energy loss spectroscopy (EELS) detector (Gatan imaging filter (GIF)) and a Philips CM12 microscope operated at 120 kV equipped with high-angle tilting (~50°) holder.

TEM sample preparation is the critical step in TEM work. The major difficulty is making the sample thin enough for electron transparency and avoiding artifacts induced by ion-milling. Different methods are applied for different materials, such as metal, ceramics and polymers. A comprehensive list of TEM sample preparation is listed on page 172 in the William and Carters' textbook.[1] In addition, there are many helpful discussions of TEM sample preparation in chapter 2 at Hirsch's classic book.[2]

Cross-sectional and planar-view TEM specimens were prepared by the following procedure. If the substrate was the intentional miscut $SrTiO_3$, the cross-sectional TEM specimens were cut along miscut direction (see figure 2.2). This enables us to observe the effect of the atomic steps on the substrate surface on oxides thin films. The slices were then glued face-to-face with a sacrifice Si piece using M-bond 610^{TM}. Several pieces of approximately 1 mm thickness were cut from a large one. For each small piece, one side of the specimen was polished and polished side was glued to a Mo/Cu-grid with M-bond 610^{TM}. Finally, the other side was mechanically ground, dimpled (Gatan dimple grinder Model 656) and Ar-ion milled (Gatan Precision Ion Polishing system PIPS Model 691) at 4.0 kV to electron transparency. In the planar-view TEM specimen preparation, several 2.5×2.5 mm^2 pieces were cut from a large piece. The thin film's side was glued on a Mo-grid by means of M-bond 610^{TM} as well. Then the substrate side was mechanically ground until the thickness of the sample was about 40 μm. Finally, the substrate side was ion-milled by Ar-ion milling at 4.0 kV to electron transparency.

The TEM micrographs were processed with DigitalMicrograph and Adobe Photoshop software. Electron diffraction simulation was performed by EMS and Crystalkit software. EDS and EELS spectra were processed by EDX and Gatan DigitalMicrograph software, respectively. The details of software can be found in the specific manuals.[15-17]

Table 2.1 Space group symmetry and lattice constants of $BiFeO_3$, $BaTiO_3$ and $PrScO_3$ at room temperature

Materials	Space group symmetry	Lattice constant (Å)	Lattice constant in pseudo-cubic setting (Å)
$BiFeO_3$[18]	*R*3c	a=5.905, α=60°	a_p=3.97
$BaTiO_3$[19]	*P*4mm (room temperature)	a=3.992, b=4.036	a_p=4.0
$PrScO_3$[13]	*P*bnm	a=5.615, b=5.776, c=8.027	a_p=4.01

Table 2.2 Space group symmetry and lattices constants of substrates and electrode used in this thesis at room temperature

Materials	Space group	Lattice constants (Å)	Lattice constant in pseudo-cubic setting (Å)
$SrTiO_3$[19]	$Pm\bar{3}m$	a=3.904	A=3.904
$SrRuO_3$[8]	*P*bmn	a=5.538, b=5.573, c=7.856	a_p=3.930
$GdScO_3$[9]	*P*bmn	a=5.488, b=5.746 c=7.934	a_p=3.970
$DyScO_3$[9]	*P*bmn	a=5.440, b=5.713 c=7.887	a_p=3.940
LSAT[20]	*P*m3m	a=3.87	a_p=3.870

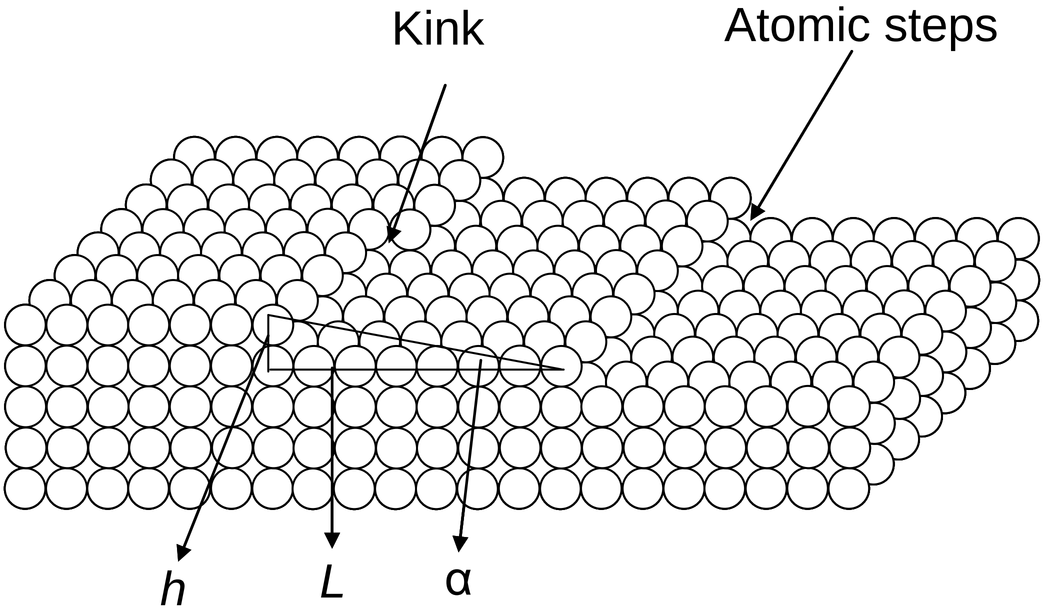

Fig. 2.1 A schematic of surface condition on the miscut substrate. One atomic step on the surface of miscut substrate is highlighted by black lines. Atomic height *h*, terrace length *L* and miscut angle α are labeled in this figure.

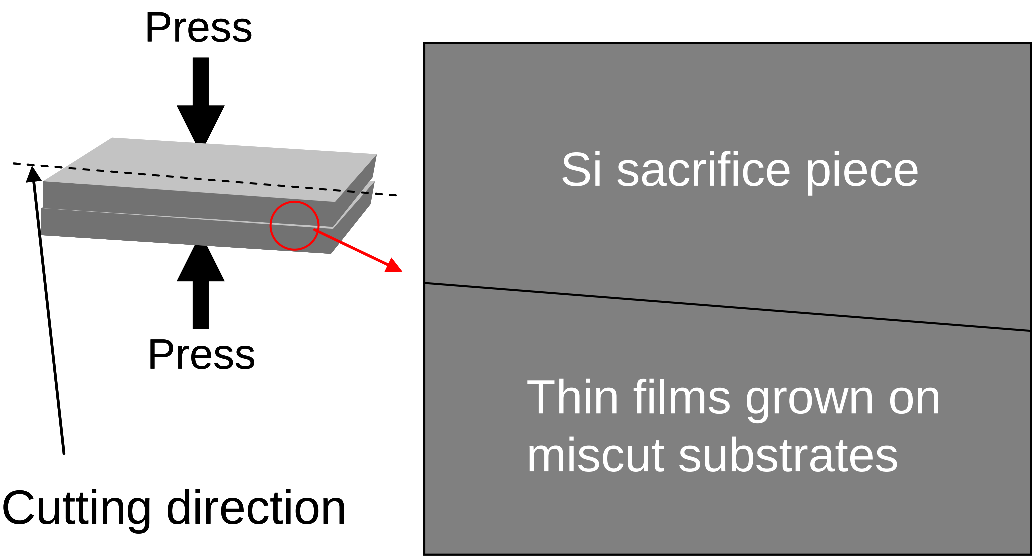

Fig. 2.2 A schematic of the cutting direction in TEM specimen preparation for thin films grown on miscut substrates.

2.4. References

[1] D. B. William, and C. B. Carter, "*Transmission Electron Microscopy-a textbook for Materials Science*," (Plenum Press, New York and London, 1996).

[2] P. Hirsch, A. Howie, R. B. Nicholson, D. W. Pashlely, and M. J. Whelan, "*Electron microscopy of thin crystals*," (Robert E. Kridger Publishing company, Malabar, Florida, 1977).

[3] W. Tian, H. P. Sun, X. Q. Pan, J. H. Yu, M. Yeadon, C. B. Boothroyd, Y. P. Feng, R. A. Lukaszew, and R. Clarke, "Hexagonal close-packed Ni nanostructures grown on the (001) surface of MgO," Appl. Phys. Lett., **86**, 131915 (2005).

[4] D. B. Williams, "*Practical analytical electron microscopy in materials science*," (2nd edition, Philips Electron Optics Publishing Group, Mahwah, New Jersey, 1987).

[5] D. Shindo, and T. Oikawa, "Analytical electron microscopy for materials science," (Springer-Verlag, 1999)

[6] D. A. Muller, N. Nakagawa, A. Ohtomo, J. L. Grazul, and H. Y. Hwang, "Atomic-scale imaging of nano-engineered oxygen vacancy profiles in $SrTiO_3$," Nature, **430**, 657 (2004).

[7] S. A. Chambers, "Epitaxial growth and properties of the thin film oxides," Surface Science reports, **39**, 105 (2000); Z. Y. Zhang, M. G. Lagally, "Atomistic processes in the early stages of thin film growth," Science, **276**, 377 (1997).

[8] R. A. Rao, Q. Gan, and C. B. Eom, "Growth mechanism of epitaxial metallic oxide $SrRuO_3$ thin films studied by scanning tunneling microscopy," Appl. Phys. Lett., **71**, 1171 (1997).

[9] J. Schubert, O. trithaveesak, A. Petraru, C. L. Jia, R. Uecker, P. Reiche, and D. G. Schlom, "Structural and optical properties of epitaxial $BaTiO_3$ thin films grown on $GdScO_3$ (110)," Appl. Phys. Lett., **82**, 3460 (2003). And references cited in this paper.

[10] C. Ratsch, J. Garcia, and R. E. Caflisch, "Influence of edge diffusion on the growth mode on vicinal surfaces," Appl. Phys. Lett., **87**, 141901 (2005).

[11] D. M. Kim, C. B. Eom, V. Nagarajan, J. Ouyang, R. Ramesh, V. Vaithyanathan, and D. G. Schlom, "Thickness dependence of structural and piezoelectric properties of epitaxial $Pb(Zr_{0.52}Ti_{0.48})O_3$ films on Si and $SrTiO_3$ substrates," Appl. Phys. Lett., **88**, 142904 (2006).

[12] K. J. Choi, M. Biegalski, Y. L. Li, A. Sharan, J. Schubert, R. Uecker, P. Reiche, Y. B. Chen, X. Q. Pan, V. Gopalan, L.-Q. Chen, D. G. Schlom, and C. B. Eom, "Enhancement of ferroelectricity in strained $BaTiO_3$ thin films," Science, **306**, 1005 (2004).

[13] C. M. Folkman, R. R. Das, C. B. Eom, Y. B. Chen, and X. Q. Pan, "Single domain strain relaxed $PrScO_3$ template on miscut substrates," Appl. Phys. Lett., **89**, 221904 (2006).

[14] H. P. Sun, Ph.D. thesis, University of Michigan, 2005.

[15] A manual for the Crystalkit software can be found from the website: www.totalresolution.com/CrystalKitManual.pdf

[16] Electron Microscopy image simulation (EMS) can be done online, website address: cecm.insa-lyon.fr/CIOL/

[17] DigitalMicrograph software was developed by Gatan Inc. The details can be found at the website address: www.gatan.com.

[18] C. Michel, J. M. Moreau, G. D. Achenbach, R. Gerson, and W. J. James, "The atomic structure of $BiFeO_3$," Solid State Comm., **7**, 701 (1969).

[19] H. P. Sun, W. Tian, X. Q. Pan, J. H. Hanei, and D. G. Schlom, "Evolution of dislocation arrays in epitaxial $BaTiO_3$ thin films grown on (100) $SrTiO_3$," Appl. Phys. Lett., **84**, 3298 (2004).

[20] Paul Scherrer institution. The detail can be found from the website address: sls.web.psi.ch/view.php/beamlines/ms/sd/sundry/index.html

CHAPTER 3

FERROELECTRIC DOMAIN STRUCTURES OF $BiFeO_3$ THIN FILMS GROWN ON MISCUT $SrTiO_3$ SUBSTRATES

3.1 Introduction

In recent years, there has been an intense focus by the material science community on multiferroic materials.[1-7] Multiferroic materials, as the nomenclature indicates, have ferroelectric (or antiferroelectric) and ferromagnetic (or antiferromagnetic) properties simultaneously. Because of these unique properties, multiferroic materials have strong potential applications in developing electric field controlled or magnetic field controlled memory device.[3] In addition to their potential application, multiferroic materials are also interesting for fundamental science. They provide an ideal system for studying the coupling mechanisms between spontaneous electric polarization (the ferroelectric order parameter) and magnetization (the magnetic order parameter). This is a very important problem in condensed matter physics.[3]

It is well known that the ferroelectric domain structure is the major extrinsic factor to the ferroelectric properties.[3] Up to now, the ferroelectric domain structure of $BiFeO_3$ has been mainly characterized by piezoelectric-force microscopy (PFM).[4,7] Transmission electron microscopy (TEM), however, can be used to determine domain type unambiguously and study the interaction between ferroelectric domains and crystalline defects such as misfit dislocations.[8,9]

In this chapter, we systematically characterized the defects, interface structures and domain structures in $BiFeO_3$ thin films grown on miscut $SrTiO_3$ substrates by TEM. Different ferroelectric domain structures are correlated to measured ferroelectric properties of $BiFeO_3$ thin films.[9]

3.2. Background and literature review

The physical theory of multiferroics involves understanding the origin of magnetic order and ferroelectric order simultaneously, as well as the possible microscopic/macroscopic interactions between ferromagnetic and ferroelectric ordering. This extremely profound problem is beyond the scope of this thesis.[1-7] In this part, we limit the summary to studies on $BiFeO_3$, the possible domain structures of rhombohedral ferroelectric thin films grown on cubic perovskite substrates, and effect of domain structures on physical properties. More details of this field can be found in some comprehensive review articles and special journal focused on multiferroics materials.[1-7]

3.2.1 Multiferroic material-$BiFeO_3$

A. Pure $BiFeO_3$ and doped $BiFeO_3$

Single phase multiferroic materials normally have pseudo-cubic perovskite structures and a general formula ABO_3**,** where A is an easy polarization element (such as Pb, Bi or a rare earth element); B is a transition metal (such as Mn, V and Fe); and O is divalent oxygen forming an O_6 octahedral network.[2] Normally, the 6s electrons of the A-site cation induce ferroelectricity, while the unpaired 3d electrons of the B-site transition metal cations contribute to the ferromagnetic or anti-ferromagnetic properties.[2] The most important multiferroic material at room temperature is $BiFeO_3$, which is ferroelectric below 1100 K and G-type anti-ferromagnetic below 734 K.[10,11] The most impressive property in $BiFeO_3$ is the large spontaneous polarization over 50 $\mu C/cm^2$ in thin film morphology, which is advantage to industrial memory devices.[4] For example, Wang *et al*. reported a large spontaneous polarization (50-60 $\mu C/cm^2$) in $BiFeO_3$ thin films deposited by pulsed laser deposition.[12] Weak ferromagnetism and coupling between ferromagnetic and ferroelectric ordering are also reported. They attributed the ferroelectric properties to mechanical strain. However, later work cases doubts about the origin of measured ferromagnetic property in $BiFeO_3$.[13,14] Thus, the origin of the ferromagnetic properties of $BiFeO_3$ is still an open question. High spontaneous polarization also has been observed in both $BiFeO_3$ bulk and thin films synthesized by metal-organic chemical vapor deposition,[15-20] high rate off-axis radio frequency sputtering[21] and molecular beam epitaxial.[22,23] It is valuable to mention the giant spontaneous polarization observed in $BiFeO_3$ thin films. Yun *et al*. reported a spontaneous polarization as high as 150 $\mu C/cm^2$ in $BiFeO_3$ thin films grown on $Pt/TiO_2/SiO_2/Si$ substrate by pulsed laser deposition.[24] Later first-principles calculations confirm the giant spontaneous polarization in high c/a ratio (~1.26) tetragonal $BiFeO_3$.[25] Giant spontaneous polarization in $BiFeO_3$ thin films is an essential property for ferroelectric dynamic random access memory devices. To couple $BiFeO_3$ thin films with existing II-VI semiconductor materials, Tian *et al*. demonstrated the growth of epitaxial $BiFeO_3$ on (0001) GaN with (111) $SrTiO_3$ / (100) TiO_2 buffer layer. X-ray diffraction (XRD) and TEM measurements show that the $BiFeO_3$ has highly crystalline quality due to the $SrTiO_3$ buffer layer despite the multidomain structure of the underlying TiO_2. The remnant polarization of $BiFeO_3$ thin films was measured as 90 $\mu C/cm^2$.[26] This opens the possibility of integrating the multifunctional $BiFeO_3$ to currently available II-VI semiconductor devices.

As is well known, there is large current leakage in both $BiFeO_3$ thin film and bulk counterpart.[3] Doping different elements (especially transition metal elements) in $BiFeO_3$ is used to decrease leakage current. For example, Shannigrahi *et al*. doped Sc into $BiFeO_3$ thin films grown by sol-gel to decrease leakage current.[27] This, in turn, improves the ferroelectric and ferromagnetic properties in Sc-doped $BiFeO_3$ thin films. Doping with Ti can also decrease leakage current in $BiFeO_3$ thin films, as reported by Wang *et al*.[28] Large enhancements in both remnant and saturated polarization were observed in Ti-doped $BiFeO_3$ thin films, too. Similar results were reported by Qi *et al*.[29] Singh *et al*. studied the ferroelectric properties of Mn-doped $BiFeO_3$ thin films grown by chemical solution deposition.[30] Leakage current density can be decreased even at high electric field (0.6 MV/cm). A well saturated hysteresis loop with remnant polarization of 100 $\mu C/cm^2$ is obtained in Mn-doped $BiFeO_3$ thin films. Kim *et al*. doped Cr into $BiFeO_3$ thin films to decrease the leakage current.[31] The leakage-current density in 3 mol % Cr-doped $BiFeO_3$ thin films is as low as 9.2×10^{-7} A/cm^2 at 100 kV/cm. A large remnant polarization (61 $\mu C/cm^2$) was measured in these films.

In summary, $BiFeO_3$ thin films with large spontaneous polarization (~60 and 90 μC/cm^2 in (001) and (111) $BiFeO_3$ thin films) can be synthesized by chemical and physical methods. The serious current leakage can be remedied by doping different transition metals.

B. Impurity phases in the Bi-Fe-O system

In addition to the relatively high current leakage problem in $BiFeO_3$, impurity phases are also found in $BiFeO_3$ thin films, especially in samples synthesized by chemical solution methods. For instance, Murakami *et al*. demonstrated that the appearance of multiple phases is controlled by adjusting the oxygen pressure during the growth.[32] With this method, the dominant phase in Bi-Fe-O system can be changed from ferroelectric $BiFeO_3$ to the mixture of $BiFeO_3$ and α-type Fe_2O_3 or γ-type Fe_2O_3 phases. Electron diffraction shows that there is a defined crystallographic orientation relationship between $BiFeO_3$ and iron oxides. Tyholdt *et al*. also studied the possible impurity phase in $BiFeO_3$ thin films synthesized by chemical solution deposition on Pt substrates.[33] XRD and TEM analysis confirmed good orientation relationship between $BiFeO_3$ and substrates. To compensate for the volatility of Bi, excess Bi content should be controlled well to have stoichiometric $BiFeO_3$ films. However, in case of highly excess Bi content, Bi-rich phase formed at the $BiFeO_3$/Pt interface. This phase was determined to be Fe substituted high temperature α-Bi_2O_3. TEM results show that the preferential growth plane for this phase is (111) and (001) orientation with respect to the substrate. $BiFeO_3$ grows with (012) coordination to (111) α-Bi_2O_3 as well. The growth of this Bi-rich secondary phase was explained by crystallization theory. Lin *et al*. studied the impurity phase in $BiFeO_3$

ceramics doped with La.[34] This ceramic sample was prepared by conventional solid-state reaction. In La-doped $BiFeO_3$ samples, one phase transition aside from the antiferromagnetic Neel transition was observed. This phase transition was attributed to trace amounts of the impurity phase $Bi_2Fe_4O_9$. Singh *et al*. also reported the generation of the $Bi_2Fe_4O_9$ impurity phase in the $BiFeO_3$ matrix.[35] The volume fraction of the impurity phase decreases with increasing film thickness according to their study.

In this chapter, we also check possible secondary phase formation in $BiFeO_3$ thin films synthesized by off-axis sputtering.

C. The study of ferroelectric domains in $BiFeO_3$

The observation and understanding of ferroelectric domains in $BiFeO_3$ is of vital importance for understanding the physical properties of this material. As early as 1984, Schmid *et al*. characterized the ferroelectric domains in single crystal $BiFeO_3$ by optical microscopy. Some triangular fringes were determined to be 71° or 109° ferroelectric domains.[36] Similar phenomena have been reported by Kubel *et al*.[37] Recently, most of domain structure information of $BiFeO_3$ has been obtained by piezoelectric force microscopy (PFM). For instance, Zavaliche *et al*. studied the polarization switching in $BiFeO_3$ films grown on 0.8° miscut $SrTiO_3$ substrates.[38] Their study shows that polarization rotates by 71° and 109°, while 180° switching is mainly observed at low fields. In their subsequent work, they observed that the 71° domains are the dominant type in $BiFeO_3$ thin films grown on 4° miscut substrate.[39] Chu *et al*. also studied the domain structure in $BiFeO_3$ by piezoelectric force microscopy (PFM). They found the crystal structure of $BiFeO_3$ to be monoclinic and the polarization vector to be close to

<111>.[40] Shafer *et al*. used the PFM to detect and manipulate ferroelectric stripe domain in $BiFeO_3$ thin films.[41] Time-resolved imaging showed 71° and 109° domains switching in a needlelike region growing from one electrode toward the other in a uniform electric field, and reversible rotation of the 71° stripe domain orientation in a non-uniform field. However, pure 180° domain switching was suppressed by the electrode geometry. Zhao *et al*. studied the correlation between anti-ferromagnetic domains and ferroelectric domains under an external electric field.[42] Ferroelectric domains were observed by PFM and anti-ferromagnetic domains were characterized by x-ray photoemission electron microscopy. In addition, antiferromagnetic domain switching induced by ferroelectric polarization switching was observed.

3.2.2 The possible domain structures in rhombohedral ferroelectric thin films grown on cubic perovskite substrates

The study of domain structure is a very important issue in ferroelectric materials, as it is the major factor affecting the measured ferroelectric properties. To completely understand this field, one must consider the crystallographic structures for all possible phases in ferroelectric materials, as well as thermal and electric history in those materials.[43-49] Therefore, a comprehensive review for this field is beyond the scope of this chapter. We will only focus on possible domain configurations in rhombohedral ferroelectric thin films grown on (001) cubic perovskite substrates.[50-57] The four possible spontaneous polarizations in ferroelectric thin films with rhombohedral structure are along $<111>_P$ (where subscription P represent in pseudocubic setting), which is shown in the figure. 3.1.[50] According to classic method proposed by Fousek and Janovec at 60's,[53] the domain wall planes are found where the spontaneous deformations produced by the transformation are matched so as to satisfy mechanical compatibility in the interface plane. The spontaneous strain tensor $\overset{=}{\varepsilon}$ in four types of distinct variants can be written as:[50]

$$\varepsilon_{kl}^{1} = \begin{pmatrix} (Q_{11}+2Q_{12})P_S^2 & \frac{1}{2}Q_{44}P_S^2 & \frac{1}{2}Q_{44}P_S^2 \\ \frac{1}{2}Q_{44}P_S^2 & (Q_{11}+2Q_{12})P_S^2 & \frac{1}{2}Q_{44}P_S^2 \\ \frac{1}{2}Q_{44}P_S^2 & \frac{1}{2}Q_{44}P_S^2 & (Q_{11}+2Q_{12})P_S^2 \end{pmatrix} \tag{3.1a}$$

$$\varepsilon_{kl}^{2} = \begin{pmatrix} (Q_{11}+2Q_{12})P_S^2 & -\frac{1}{2}Q_{44}P_S^2 & -\frac{1}{2}Q_{44}P_S^2 \\ -\frac{1}{2}Q_{44}P_S^2 & (Q_{11}+2Q_{12})P_S^2 & \frac{1}{2}Q_{44}P_S^2 \\ -\frac{1}{2}Q_{44}P_S^2 & \frac{1}{2}Q_{44}P_S^2 & (Q_{11}+2Q_{12})P_S^2 \end{pmatrix} \tag{3.1b}$$

$$\varepsilon_{kl}^{3} = \begin{pmatrix} (Q_{11}+2Q_{12})P_S^2 & \frac{1}{2}Q_{44}P_S^2 & -\frac{1}{2}Q_{44}P_S^2 \\ \frac{1}{2}Q_{44}P_S^2 & (Q_{11}+2Q_{12})P_S^2 & -\frac{1}{2}Q_{44}P_S^2 \\ -\frac{1}{2}Q_{44}P_S^2 & -\frac{1}{2}Q_{44}P_S^2 & (Q_{11}+2Q_{12})P_S^2 \end{pmatrix} \tag{3.1c}$$

$$\varepsilon_{kl}^{4} = \begin{pmatrix} (Q_{11}+2Q_{12})P_S^2 & -\frac{1}{2}Q_{44}P_S^2 & \frac{1}{2}Q_{44}P_S^2 \\ -\frac{1}{2}Q_{44}P_S^2 & (Q_{11}+2Q_{12})P_S^2 & -\frac{1}{2}Q_{44}P_S^2 \\ \frac{1}{2}Q_{44}P_S^2 & -\frac{1}{2}Q_{44}P_S^2 & (Q_{11}+2Q_{12})P_S^2 \end{pmatrix} \tag{3.1d}$$

Where ε_{kl}^{i} is a components of the spontaneous strain tensor for variant i, the Q_{mn} are components of the electrostrictive tensor, and P_S is the magnitude of the spontaneous polarization. The allowed domain boundaries between variants are those that have equivalent spontaneous deformation of the boundary plane. These coherent twin boundaries can be determined by calculating the difference tensor $\overline{\overline{\Delta\varepsilon^{ij}}}$ of spontaneous strains between variants i and j. Then the displacement vector δu^{ij} is calculated as

$$\delta u^{ij} = \overline{\overline{\Delta\varepsilon^{ij}}} \bullet \delta\vec{r} \qquad (3.2)$$

Where $\delta\vec{r}$ is a general real space vector; $\overline{\overline{\Delta\varepsilon^{ij}}}$ describes the differences in spontaneous strains between two variants and δu^{ij} represents the difference in spontaneous displacement between i and j variants. The coherent twin planes may be found by noting that lies in the twin plane, then the allowed nonzero component of δu^{ij} is normal to the twin plane. That is, in the reference frame of the high temperature phase, the coherent twin planes have identical deformation within the twin plane in both variants. Thus the possible coherent twin planes (hkl) can be found by noting that δu^{ij} is parallel to the normal to the plane (hkl) and that the displacement difference vector δu^{ij} is perpendicular to any vector $\delta\vec{r}$ in the twin plane, i. e., solving

$$\vec{g}_{hkl} \bullet \delta\vec{r} = 0 \text{ and } \delta u^{ij} \bullet \delta\vec{r} = 0 \qquad (3.3)$$

Directly leads to the coherent twin planes. As an example, consider the possible coherent twin planes between variants 1 and 2 for the ferroelectric rhombohedral phase. The difference tensor $\overline{\overline{\Delta\varepsilon^{12}}} = \overline{\overline{\varepsilon^{1}}} - \overline{\overline{\varepsilon^{2}}}$ for spontaneous strains is given as

$$\overline{\overline{\Delta\varepsilon_{kl}^{12}}} = \begin{pmatrix} 0 & Q_{44}P_S^2 & Q_{44}P_S^2 \\ Q_{44}P_S^2 & 0 & 0 \\ Q_{44}P_S^2 & 0 & 0 \end{pmatrix} \qquad (3.4)$$

And take $\delta\vec{r}$ parallel to the direction [uvw] the displacement difference vector δu^{ij} between variants 1 and 2 is

$$\delta u^{ij} = Q_{44} P_S^2 \begin{pmatrix} v+w \\ u \\ u \end{pmatrix} \qquad (3.5)$$

Setting the scalar product of δu^{ij} with the direction [uvw] equal to zero leads to

$$\delta u^{ij} \bullet \delta \vec{r} = 2Q_{44} P_S^2 u(v+w) = 0 \qquad (3.6)$$

This equation either has solutions for u =0, or $v+w$ =0. Therefore, if u =0, any direction $\delta \vec{r}$ =[0 vw] lies in the (100) plane, which is therefore the coherent twin plane. Similarly, for $\delta \vec{r}$ =[$uv\bar{v}$], $v+w$ =0, any direction [$uv\bar{v}$] lies in the (011) plane, which is therefore the second possible twin plane. Following the same method, all coherent domain planes for the ferroelectric thin films grown on (001) cubic perovskite substrates are summarized in table 3.1.[50] Three-dimensional schematics of 71° {101}-type and 109° {100}-type ferroelectric domain, two typical domain patterns in rhombohedral ferroelectric thin films, are shown in figure 3.2 (a) and (b), respectively.[50] Their corresponding cross-sectional views are presented in figure 3.2(c) and (d). These theoretical morphologies will be used to analyze experimental images.

From the energy consideration, the formation of domains in ferroelectric thin films leads to decrease the strain energy built in thin films.[51,52,55] The strain energy comes naturally from the different lattice parameter between films and substrate, as well as thermal effect. Thermal effect stems from the fact that the thin films are normally deposited as high temperature (~500 °C to 800 °C), then cooled to room temperature after deposition under specific oxygen environment. Therefore, the width in ferroelectric domain reflects the balance of anisotropic elastic energy, domain wall energy, and electric energy.[51,56] This problem is carefully studied by both thermodynamic[54-57] and mechanical methods.[51,52] The major results obtained by these two methods are identical.

But thermodynamic results need information of coefficients in free energy expanded as Landau-Devonshire series.[54,55] These coefficients were measured from bulk materials, which are probably different from thin films counterpart.[54] Therefore in coming discussion, we only introduce the mechanical method which was developed in Romanov's papers.[51,52] According to this method, the strain energy in {101} periodic domain r_1/r_4 lamellae (shown in Fig. 3.2(d)) consists of two parts: shear strain and biaxial strain energy. It is expressed as

$$E = lhG\omega_e^2 \qquad (3.7)$$

where l and h are domain width and thin films thickness, respectively. ω_e is the angle distortion in rhombohedral structure deviation from ideal perovskite structure . And {101} surface energy is

$$E^{Twin} = 2\sqrt{2}h\gamma^{\{101\}} \qquad (3.8)$$

where $\gamma^{\{101\}}$ represents the domain energy. The strain energy between r_1/r_4 domain and strain energy between thin films and substrates can be simulated by two types of coherent dislocations (Somigliana screw dislocation dipoles and quadrupoles).[51-52] After long derivation, the strain energy between coherent ferroelectric domains is

$$E^{SQ} = \frac{G\omega_s^2 l^2}{2\pi}\left[\frac{8h}{l}\tan^{-1}\frac{l}{2h} - \frac{4h}{l}\tan^{-1}\frac{l}{h} + \ln\left(\frac{4h^2+l^2}{h^2+l^2}\right) + \frac{2h^2}{l^2}\ln\left(\frac{16h^3\sqrt{h^2+l^2}}{\left(4h^2+l^2\right)^2}\right)\right] \qquad (3.9)$$

Combining the above energy term, the energy change after the formation of {101}-type multi-domain from mono-domain configuration can be expressed as:

$$
\begin{aligned}
\Delta E &= E^{Mul} - E^{Monodomain}\left(2l\right) \\
&= \frac{G\omega^2 l^2}{2\pi}\left\{\frac{8h}{l}\tan^{-1}\frac{l}{2h} - \frac{4h}{l}\tan^{-1}\frac{l}{h} + \ln\left(\frac{4h^2+l^2}{h^2+l^2}\right) + \frac{2h^2}{l^2}\ln\frac{16h^3\sqrt{h^2+l^2}}{\left(4h^2+l^2\right)^2}\right\} \quad (3.10) \\
&+ 2\sqrt{2}\gamma^{\{101\}} - Ghl\omega^2
\end{aligned}
$$

The calculated result of the energy change under different domain thicknesses is shown in figure 3.3. As shown in this figure, we can see that the formation of multidomains is energetically favorable. And there is an energy minimization under a specific domain width that is nominated as domain width at equilibrium condition. It is value to study the relationship between domain width at equilibrium condition and thin film thickness. By minimization of energy change in Eq. (3.10), domain width and thin film thickness are satisfied below self-consistent equation:

$$\frac{\partial}{\partial l}\left(\Delta E\right) = 0 \qquad (3.11)$$

In the case of domain width being much smaller than thin film thickness, there is a simple square root relationship between domain width and thin film thickness. It is expressed as:

$$l_{\min} = 2^{3/4}\left(\frac{\pi}{\ln 2}\right)\sqrt{\frac{\gamma^{\{101\}}h}{G\omega_s^2}} \qquad (3.12)$$

Experimental results will be fitted by this formula, and domain energy in $BiFeO_3$ can be extracted from a fitting parameter. The aforementioned method can be easily extended to {100}-type ferroelectric domain lamellae easily. The details of this case can be found in Romanov's paper.[51] One more important issue is that the surface energy of {100}-type domains, according to Landou-Devonshire theory, is the three times of that in {101}-type domains.[58] Therefore, it is reasonable to expect that the population of {101}-type domains is much higher than that of {100}-type ones

It should be emphasized that above discussion only considers mechanical condition at the ferroelectric boundaries. Other factors, such as the thermal history stemming from the different thermal expansion coefficients between films and substrates, also have dramatic effects to the ferroelectric domain structures. Until now, there are some papers discussing the stable domain configurations in ferroelectric thin films with tetragonal phase under different lattice mismatch and temperatures.[43-48] Extension of same discussion to rhombohedral ferroelectric thin films has been published in a review paper recently.[59]

3.2.3 The effect of ferroelectric domain on physical properties

Ferroelectric domain structures have dramatic effect on physical properties. The classic example is the commercialization of periodically poled ferroelectric single crystal chip.[60] The procedures in this work include designing electrodes, patterning electrodes using *state-of-the-art* photolithograph, poling ferroelectric domains confined by electrode pattern. The underlying physical principle is to manipulate ferroelectric domains. The non-linear optical beam can be coherently generated from two neighboring ferroelectric domains with opposite 180° spontaneous polarization. Zhu *et al*. demonstrated the realization of three beam output in a quasi-periodic-poled $LiTaO_3$ single chip.[61] The three beam generation comes from fundamental incident beam, second-harmonic generation as well as sum-frequency-generation between fundamental and second-harmonic beam. The efficiency of sum-frequency-generation can be as high as 23.0%. Zhu *et al*, extended similar idea to generation of red, green and blue in two-dimensional poled ferroelectric chips.[62] Domain structures affect the piezoelectric and dielectric properties of ferroelectric materials too. For example, Nagarajan *et al*. demonstrated a significantly enhanced piezoelectric response by switching non-180^{o} domain walls under external electric field.[63] Capacitors 1 μm^2 show a double of the remnant polarization at voltage as 15 V and piezoelectric coefficient of 250 pm/V. The piezoelectric coefficient is about three times of that in a single crystal with single domain (it is 87 pm/V in bulk sample). Xu *et al*. used electric-filed to manipulate the polar nano-regions in relaxor ferroelectric single crystals.[64] Dielectric measurements on poled PZN along the [111] direction by a field of 20 kV/cm show that diffuse ferroelectric phase is much more pronounced than that in non-poled PZN. This proves that the electric poling enhances the ferroelectric order in relaxor ferroelectric materials.

Up to now, to the best of our knowledge, there are two papers to discuss the manipulation of ferroelectric domains by means of vicinal substrates. Nagarajan *et al*. found that tetragonal PZT thin films grown on miscut (100) $SrTiO_3$ substrates have preferential domain (a-type).[65] The preferential domains are nucleated along the step edges on the substrate surface according to their opinion. And the critical thickness in formation of a-type domain is much lower than that in PZT grown on flat $SrTiO_3$ substrates. Finally, they proposed a model based on minimization of elastic energy to explain the preferential domain growth in miscut substrates. Chu *et al*. manipulated the ferroelectric domains by controlling the growth mode in $SrRuO_3$ electrode.[66] Step-grown $SrRuO_3$ makes the formation of periodic domains in $BiFeO_3$ thin films, while $BiFeO_3$ grown on $SrRuO_3$ electrode of random surface has none-periodic ferroelectric domains. Some ideas in above two papers have similarity with these in this chapter, but we systematically study this problem and correlate the physical properties with observed ferroelectric domain structures.[9]

3.3. Experimental

$BiFeO_3$ thin films with several thicknesses ranging from 200 nm to 1000 nm were deposited by high-rate off-axis sputtering on 0.8° and 4° miscut (001) $SrTiO_3$ substrates with 100 nm $SrRuO_3$ bottom electrodes. The details of growth conditions have been described at chapter 2. To study the domain structures systematically, 200 nm and 600 nm $BiFeO_3$ were grown on low-angle (<1°) miscut $SrTiO_3$ substrates; 200 nm, 450 nm, 600 nm and 1000 nm $BiFeO_3$ were grown on 4° miscut $SrTiO_3$ substrates.

The cross-sectional slices for TEM studies were obtained by cutting the $BiFeO_3/SrRuO_3/SrTiO_3$ sample parallel to the miscut direction so that the atomic steps on the miscut substrate run along the electron beam direction. TEM studies were carried out on a Philips CM12 operated at 120 KV with a high-angle (± 50°) double-tilt holder and on a JEOL 3011 ultra high resolution TEM operated at 300 KV with a point-to-point resolution of 0.17 nm. Analytical transmission electron work was conducted in a JEOL 2010F analytical TEM that are equipped with Oxford energy dispersion spectroscopy (EDS) detector and Gatan’s imaging filter tool. During the EDS and electron energy loss (EELS) characterization, a nominated 1-nm-size electron beam probe was used. The EDS spectra were processed by means of EDX Genesis software. And the Gatan DigitalMicrograph software was used to process EELS spectra.

3.4. Results

3.4.1 $BiFeO_3$ thin films grown on low-angle miscut $SrTiO_3$ substrates

Figure 3.4(a) is a typical micrograph for the 200 nm $BiFeO_3$ grown on low angle miscut (0.2°) $SrTiO_3$ substrate with 100 nm $SrRuO_3$ electrode. It can be seen the $BiFeO_3$ has uniform thickness through the films. And some particles are embedded in the films matrix. Selective area electron diffraction, EDS and EELS were conducted to study the particles' properties. Figure 3.4(b) is the SAED pattern taken from area covering matrix and one particle which is indicated by a circle in Fig. 3.4(a). One can see that except the major spots that can be determined as perovskite $BiFeO_3$ phase, there is a set of symmetric spots. These spots can be indexed well by assuming the particle as α-type Fe_2O_3 oxide. The orientation relationship between $BiFeO_3$ matrix and α-type Fe_2O_3 can be expressed as: $[42\bar{1}]$ $(\bar{1}1\bar{2})$ $BiFeO_3$ // $[1\bar{1}2]$ $(\bar{1}32)$ α-Fe_2O_3. EDS spectrum taken from particle area is shown in figure 3.5(a). We can see that there are only Fe and O elements in the spectrum. Quantitative calculation proves that the atomic ratio between Fe and O is 0.6, which is close to the nominated one in chemical formula α-Fe_2O_3. It should be mentioned that it is required to do calibration in quantitative EDS study. In our quantitative study, we chose the $BiFeO_3$ matrix as internal reference and assumed that $BiFeO_3$ matrix is stoichiometric. The same area was studied by EELS, which is shown in figure 3.5(b). One can see that there are Fe and O elements. Quantitative calculation for atomic ratio between Fe and O is close to EDS result, too.

Figure 3.6(a) shows a representative dark field cross-sectional TEM image for a 600 nm $BiFeO_3$ / 100 nm $SrRuO_3$ film grown on a 0.8° miscut (001) $SrTiO_3$ substrate. It can be seen that there are many fringes along the $\{101\}_P$ (in this chapter subscript P represents pseudo-cubic setting) and $\{100\}_P$ planes of the $BiFeO_3$ thin films. The SAED patterns from two different areas, indicated by circles in Fig. 3.6(a), are shown in figure 3.6 (b) and 3.6(c). The diffraction pattern in Fig. 3.6 (b), from region including the $\{100\}_P$-type fringes, shows the clear splitting on high order reflection spots along [010] direction, indicated by arrows. This reveals that the $\{100\}_P$ type of fringes are 109° domain walls, which is consistent with previous theoretical discussion (shown in Fig. 3.2) for possible domain structures in rhombohedral ferroelectric thin films grown on (001) cubic perovskite substrates (such as $SrTiO_3$).[50, 51] On the contrary, diffraction spots in Fig. 3.6(c) from region including the $\{101\}_P$-type fringes are clearly elongated along the $[101]_P$ direction, also indicated by arrows. The corresponding fringes are determined to be 71^o ferroelectric domain walls.[50, 51] In addition, Fig 3.6(a) shows that the population of $\{101\}_P$-type domain walls is higher than that of $\{100\}_P$-type domain walls. Similar phenomena has been observed in rhombohedral PZT bulk materials.[58]

High resolution TEM images in Figure 3.7(a) and (b) show the atomic structures of 71° and 109° domain walls in the same specimen, respectively. It is evident that the structural width (defined by the contrast change in image) of the 71° domain wall is much smaller than that of the 109° domain wall. This is possible due to the lower energy of 71° domain walls compared with that of 109° domain walls as discussed below. Phenomenological Landau-Ginzburg (L-G) free energy calculations show that the $\{100\}_P$ type domain surface energy is three times that of $\{101\}_P$ type twin domain in bulk ferroelectric materials,[58] and are therefore less likely to occur. This conclusion can also possibly be applied to ferroelectric thin films because the x-ray diffraction and electron diffraction result described above show that the $BiFeO_3$ thin films studied in this work have been fully relaxed via formation of domains and misfit dislocations.[21] The atomic structure of one misfit dislocation was studied by the HRTEM, which is shown in figure 3.8. To identify the type of misfit dislocation, reverse-fast-Fourier-transformation (RFFT) image is shown at inset of figure 3.8. The corresponding area used to construct the RFFT pattern is indicated by white dash square. It is obvious that the Burgers vector belongs to <011>-type. Except the misfit dislocations, we can see that there is free of impurity phase at $BiFeO/SrRuO_3$ interface and interface is atomically sharp.

3.4.2 $BiFeO_3$ thin films grown on 4° miscut $SrTiO_3$ substrates

In comparison to films grown on 0.8° (001) $SrTiO_3$ substrates, the domain structure of $BiFeO_3$ with the different thicknesses grown on 4° miscut $SrTiO_3$ were also studied. Figure 3.9(a) and (b) show the representative TEM image of the 200 nm $BiFeO_3$ and 600 nm $BiFeO_3$ thin films grown on 4° miscut $SrTiO_3$ substrates with 100 nm $SrRuO_3$ electrodes, respectively. Fringes parallel to $[101]_P$ direction can be seen in these $BiFeO_3$ thin films. In accordance with the previous discussion, these fringes are 71° domain walls. The atomic structure for the 71° is shown in figure 3.10. One can see that it is identical to micrograph shown in figure 3.7(a). In addition, as shown in figure 3.9(a), there are periodic misfit dislocations generated at $BiFeO_3/SrRuO_3$ interface. The atomic structure of a misfit dislocation is shown in figure 3.11. The Burgers vector is also determined as <011>$_P$-type. A more interesting point is that there are no 109° domain walls in this sample. Similar results were obtained on 600 nm $BiFeO_3$ / 100 nm $SrRuO_3$ heterostructure grown on 4° miscut $SrTiO_3$ substrate, which is shown in Figure 3.9(b). It is apparent that the {101}$_P$ type 71° domain walls in $BiFeO_3$ grown on 4° miscut $SrTiO_3$ (Fig. 3.9) are distributed much more uniformly in comparison with the films grown on 0.8° (001) $SrTiO_3$ substrates. The domain width and thin films thickness are indicated in figure 3.9(b). Plane-view TEM observations (not shown here) of the same films show that the 71° stripe domains are oriented perpendicular to the miscut direction, $[100]_P$, in films grown on 4° miscut $SrTiO_3$, but run along both the $[100]_P$ and $[010]_P$ directions in films grown on exact (001) $SrTiO_3$. This explains why no domain walls are seen in some regions of cross-sectional specimen. These results agree well with the in-plane piezoelectric-force microscopy (PFM) observations of the same films as studied in the work.[39]

To test the validation of the single domain growth in $BiFeO_3$ films on high angle miscut (miscut angle is 4°) $SrTiO_3$ substrates, two other $BiFeO_3$ thin films with thicknesses of 450 nm and 1 μm grown on 4° miscut $SrTiO_3$ substrates were studied. Figure 3.12 (a) and (b) are the typical bright-field micrographs for 450 nm and 1 μm $BiFeO_3$ films grown on 4° miscut $SrTiO_3$ substrates with 100 nm $SrRuO_3$ electrodes, respectively. We can see that there are only 71° lamellae ferroelectric domains in $BiFeO_3$ films. The relationship between 71° domain width and the thin films thickness for above 4 $BiFeO_3$ samples grown on 4° miscut $SrTiO_3$ substrates were shown in figure 3.13. The solid line is the fitted result by means of Eq. (3.12), which agrees well with the experimental values measured in TEM images. By fitting these data, the domain energy can be extracted as described at the following.

The ferroelectric hysteresis loops of 600 nm $BiFeO_3$ thin films grown on 0.8° and 4° miscut $SrTiO_3$ substrates are shown in dot-triangle and solid-square curves in figure 3.14. One can see that these hysteresis loops have well-defined saturated sharp. It means that the leakage current in these films is negligible. It should be emphasized that the saturated spontaneous polarization in $BiFeO_3$ films grown on 0.8° and 4° miscut are 52.3 and 57.9 $\mu C/cm^2$, respectively. The different saturated spontaneous polarization in these two samples is attributed to different domain structures observed by TEM, which will be discussed below.

3.5. Discussions

3.5.1. The possible mechanism for single-domain growth in $BiFeO_3$ on high-angle miscut $SrTiO_3$ substrates

Above TEM work imply that the atomic steps induced by the miscut of $SrTiO_3$ provide a preferred location for the nucleation and growth of 71° domains. It has been suggested that the nucleation of single domains on miscut substrates is due to either surface energy minimization or control of growth parameters to facilitate the step-flow growth from atomic steps, terraces & kinks on the surface of vicinal substrate.[67,68] The growth of domains in $BiFeO_3$ thin films involves the motion of domain walls which are oriented along the $\{101\}_P$ planes, in parallel with the [100] or [010] directions of $SrTiO_3$. The substrate surface steps oriented perpendicularly to the miscut direction [100] induced by miscut can play a role to pin the domain walls and limit the growth of domains in the direction perpendicular to the steps, thus resulting the one dimensional array of stripe domains observed. In other words, atomic steps probably can be worked as 71° domain-pinning centers. And, according to above discussion, it is energetically favorable to form 71° ferroelectric domain with respect to 109° ferroelectric domain. It is because that domain energy of 109° ferroelectric domain is three times that of 71° ferroelectric domain.[58]

3.5.2. The domain energy in $BiFeO_3$

As we discussed in the introduction, the ferroelectric domain width is the result of competition between mechanical strain and domain energy. If the thickness of thin films is much larger than domain width, the dependence of domain with l at equilibrium on the thin film thickness h can be written as:

$$l_{\min} = 2^{3/4}\left(\frac{\pi}{\ln 2}\right)\sqrt{\frac{\gamma^{\{101\}}h}{G\omega_s^2}} \tag{3.12}$$

where G represents Young's modulus, $\gamma^{\{101\}}$ the domain energy, and ω_s the rhombohedral distortion.[51] The same scaling law is also kept for domain structure in ferroelectric thin films with tetragonal structure.[47] As shown in figure 3.13, the fitting results agree well with the experimental values measured in TEM images. The fitting of experimental results with Eq. (3.12) gives the 71° domain wall energy of $9.2\pm0.49\times10^{-2}$ J/m^2. In this calculation, Young's modulus is estimated to be 100 GPa, a typical value for perovskite oxides.[11] The 109° domain energy also can be calculated as $27.9\pm0.93\times10^{-2}$ J/m^2 since

109° domain energy is three times that of 71° domain.[58] The calculated domain energy of $BiFeO_3$ thin films is of the same order as other oxides with perovskite structure (~10^{-2} J/m^2).[51]

3.5.3. The effect of domain structures on ferroelectric property in $BiFeO_3$ films

Different domain structures observed in $BiFeO_3$ thin films grown on 0.8° and 4° miscut (001) $SrTiO_3$ substrates result in different ferroelectric properties. As shown in figure 3.14, the saturated spontaneous polarization of 600 nm $BiFeO_3$ grown on 0.8° and 4° miscut (001) $SrTiO_3$ substrates are 52.3 and 57.9 $\mu C/cm^2$, respectively.[21] TEM studies show that the $BiFeO_3$ thin films grown on 0.8° (001) $SrTiO_3$ substrate are composed of 71° and 109° domains, while there is only 71° domain in $BiFeO_3$ grown on 4° miscut $SrTiO_3$. As a result, there exist a number of line defects at the junction between 71° and 109° domain walls in films grown on 0.8° miscut (001) $SrTiO_3$ substrates. The arrangement of atoms along these defects is highly disordered, thus domain walls can be pinned by these line defects. This may inhibit full polarization when the external electric field is applied to thin films. But quantitative contribution of the 109° domains embedded in 71° stripe domains matrix to measured saturated spontaneous polarization is still not clear, which will be studied by phase-field simulations.[59] Therefore the multi-domain structure in $BiFeO_3$ thin films grown on 0.8° miscut $SrTiO_3$ substrates probably leads to a lower saturated spontaneous polarization, compared with $BiFeO_3$ thin film grown on 4° miscut $SrTiO_3$ substrate.

3.6. Conclusions

200 nm $BiFeO_3$ thin films grown on low-angle (miscut angle 0.8°) miscut $SrTiO_3$ consist of perovskite $BiFeO_3$ and α-type Fe_2O_3 impurity phase. And there are 71° and 109° ferroelectric domain walls in $BiFeO_3$ thin films.

200 nm, 450 nm, 600 nm, and 1μm $BiFeO_3$ thin films grown on 4° miscut $SrTiO_3$ substrates are composed of 71° ferroelectric lamellae domains.

The misfit strain in $BiFeO_3$ thin films grown on miscut $SrTiO_3$ substrates is relaxed by the formation of ferroelectric domains and misfit dislocations. The Burgers vector of misfit dislocations belongs to $<011>_P$-type.

The domain width in $BiFeO_3$ thin films grown on 4° miscut (001) substrates increases as film thickness increases due to a reduction in domain wall energy. The domain width has a simple square root relationship with respect to thin films thickness. By fitting with theoretical result, the 71° and 109° ferroelectric domain energies in $BiFeO_3$ can be extracted.

The mixture of 71° and 109° ferrelectric domains in 600 nm $BiFeO_3$ films on 0.8° miscut $SrTiO_3$ has lower saturated spontaneous polarization than $BiFeO_3$ films grown on 4° miscut $SrTiO_3$ substrate. This is probably due to the crossover of domain walls of different types limiting the domain switching under externally applied field.

Table 3.1 Ferroelectric domain boundaries between different domain variants. The spontaneous polarization is along the [111], $[\bar{1}11]$, $[\bar{1}\bar{1}1]$, and $[1\bar{1}1]$ direction for variances 1, 2, 3, and 4, respectively.[51]

Variant	1	2	3	4
1		(100) (011)		(010) (101)
2			(010) $(\bar{1}01)$	
3				(100) $(0\bar{1}\bar{1})$

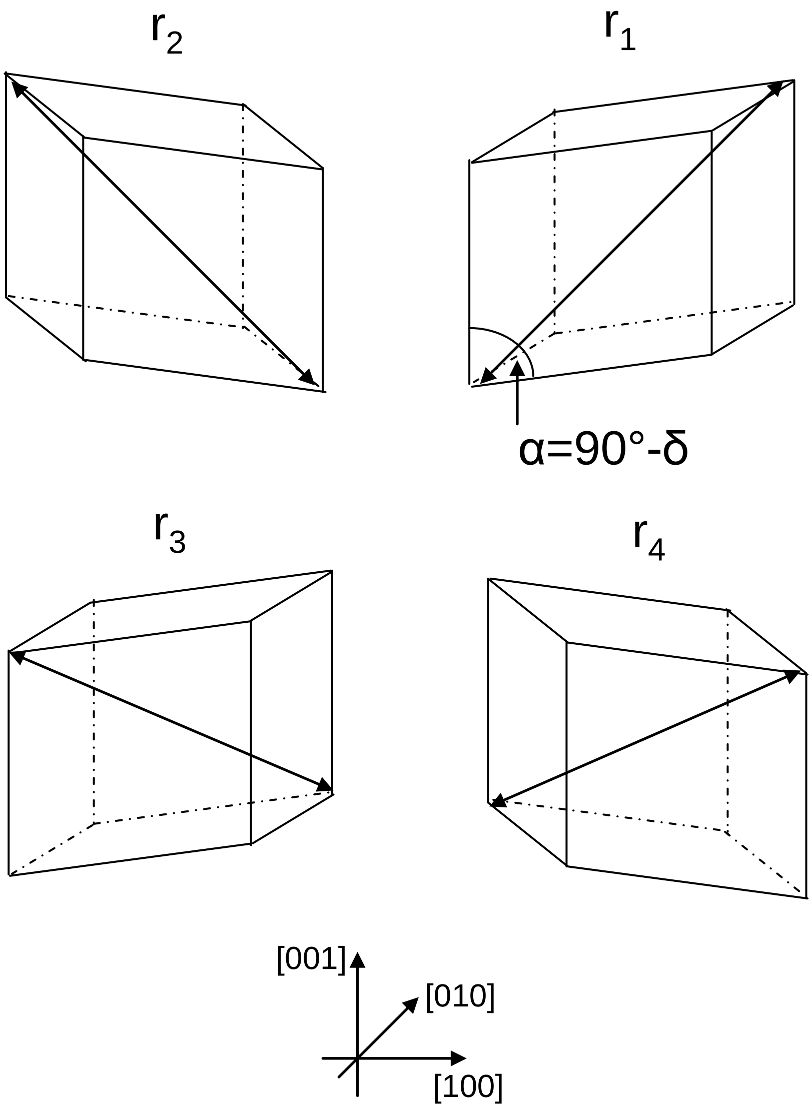

Fig. 3.1 The four possible directions of spontaneous polarization in rhombohedral ferroelectric materials (redrawn after Fig. 1 at reference 51). In pseudo-cubic setting, the spontaneous polarizations r_1^+, r_2^+, r_3^+ and r_4^+ can be written as [$P_x\hat{x}, P_y\hat{y}, P_z\hat{z}$], [$-P_x\hat{x}, P_y\hat{y}, P_z\hat{z}$],[$-P_x\hat{x}, -P_y\hat{y}, P_z\hat{z}$] and [$P_x\hat{x}, -P_y\hat{y}, P_z\hat{z}$] respectively.

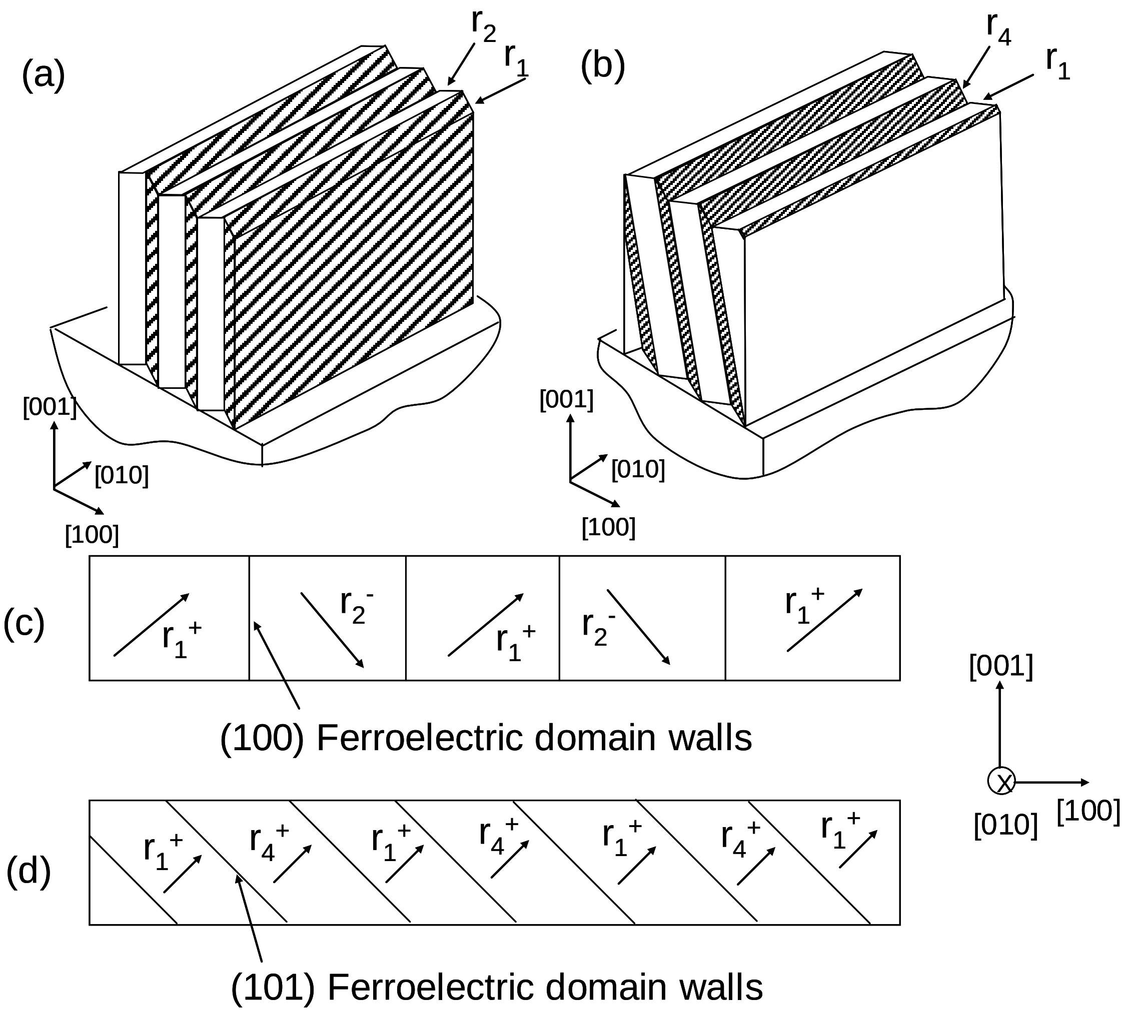

Fig. 3.2 (a) The three-dimensional morphology of 109° ferroelectric domain (r_1^+/r_2^-) lamellae. (b) The three-dimensional morphology of 71° ferroelectric domain (r_1^+/r_4^+) lamellae. (c) The cross-sectional view of 109° ferroelectric domain lamellae. (d) The cross-sectional view of 71° ferroelectric domain lamellae (redrawn after Fig. 3, 4 and 6 at reference 51).

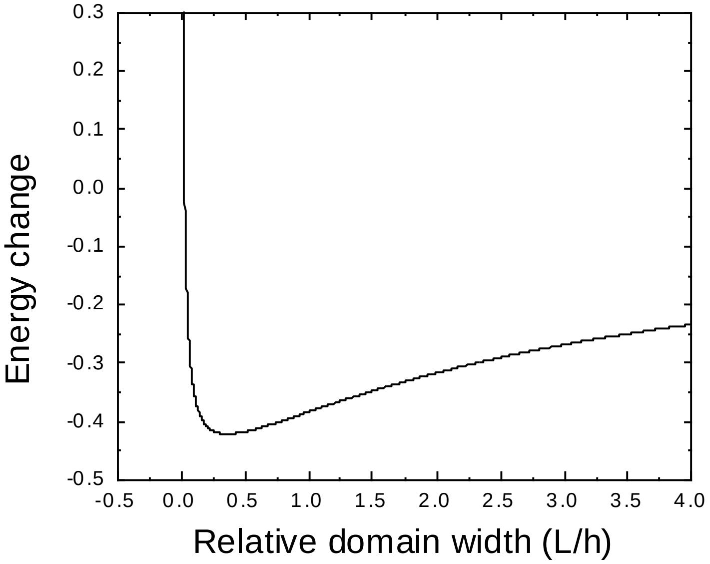

Fig. 3.3 The energy change after the formation of 71° ferroelectric domain lamellae (shown in Fig. 3.2(b)) from single domain configuration under different domain width. The domain energy is assumed as 15.0×10^{-2} J/cm^2.

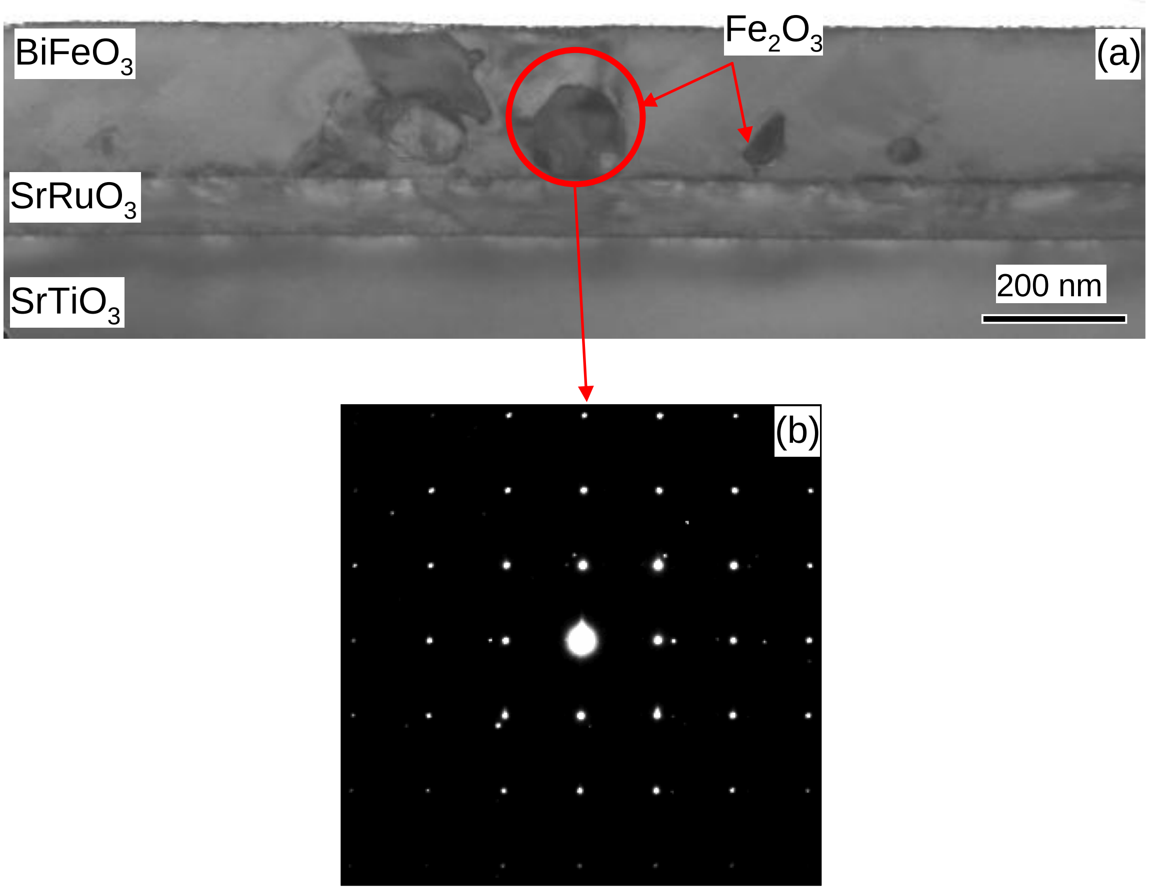

Fig. 3.4 (a) The bright-field image for 200 nm $BiFeO_3$ thin films grown on 0.4° miscut $SrTiO_3$ substrates with 100 nm $SrRuO_3$ electrode showing existence of perovskite $BiFeO_3$ matrix and particle-like secondary phases. (b) The selective area electron diffraction pattern taken from area covering $BiFeO_3$ matrix and α-Fe_2O_3 secondary phase.

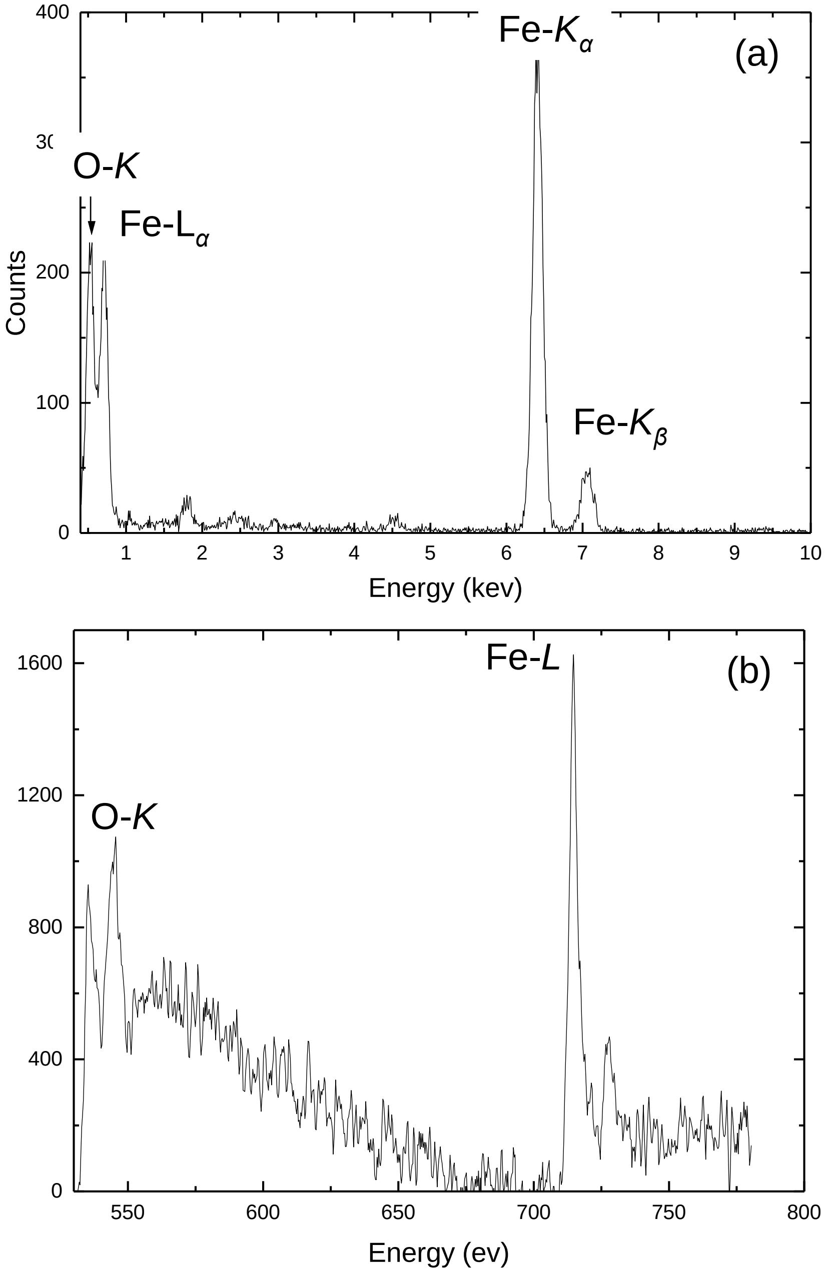

Fig. 3.5 (a) X-ray energy dispersive spectroscopy (EDS) spectrum of α-Fe_2O_3 secondary phase. (b) Electron energy loss spectroscopy (EELS) spectrum with background subtracted of α-Fe_2O_3 secondary phase.

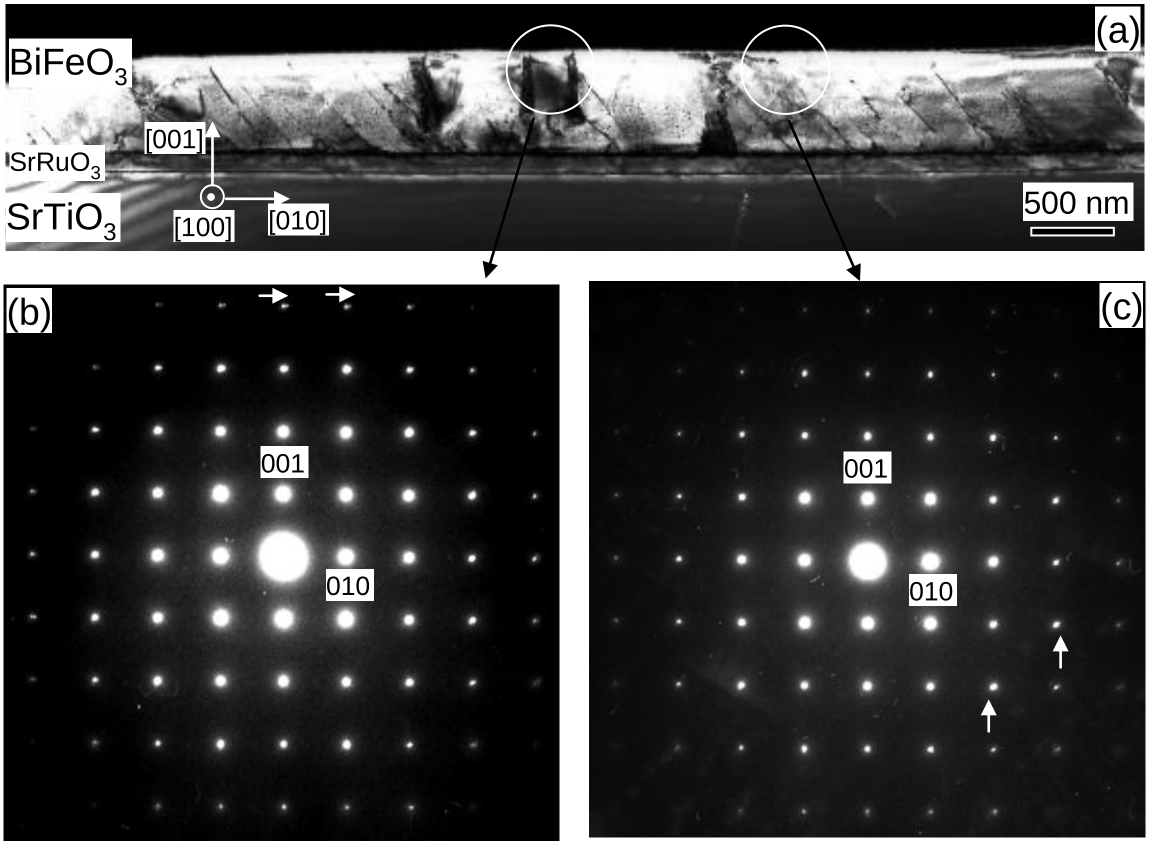

Fig. 3.6. (a) The dark field image for 600 nm $BiFeO_3$ thin films grown on 0.8° miscut $SrTiO_3$ substrates with 100 nm $SrRuO_3$ bottom electrode showing the 109° and 71° ferroelectric domains. (b) The SAED pattern taken from 109° ferroelectric domain area indicated by white circle. (c) The SAED pattern taken from 71° ferroelectric domain area indicated by white circle too. The splitting/elongation in high-order reflection spots are obvious, which are indicated by white arrows.

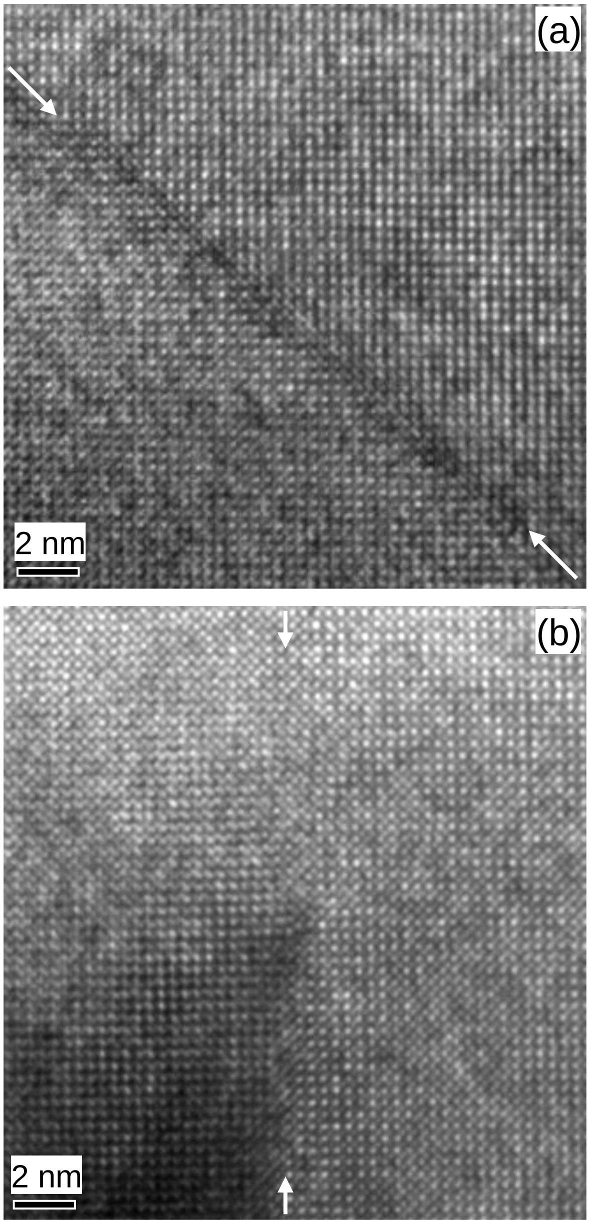

Fig. 3.7 (a) The high-resolution TEM micrograph of 71° ferroelectric domain. (b) The high-resolution TEM micrograph of 109° ferroelectric domain. The atomic distortion around the ferroelectric domain walls is obvious.

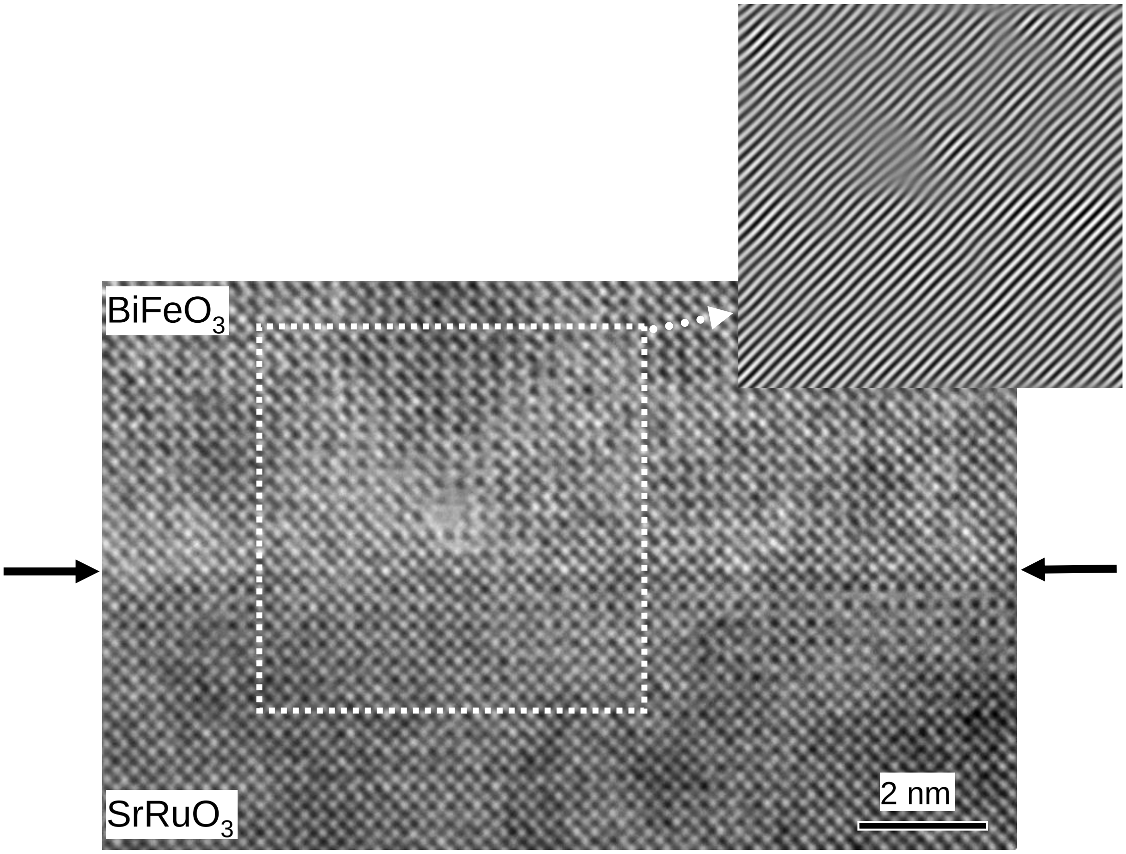

Fig. 3.8 The atomic structure of a misfit dislocation generated at interface between $BiFeO_3$ and $SrRuO_3$ in sample 600 nm $BiFeO_3$ grown on 0.8° miscut $SrTiO_3$ substrate with 100 nm $SrRuO_3$ bottom electrode. The inset is the reverse fast Fourier transformation image constructed from area indicated by a white dash square.

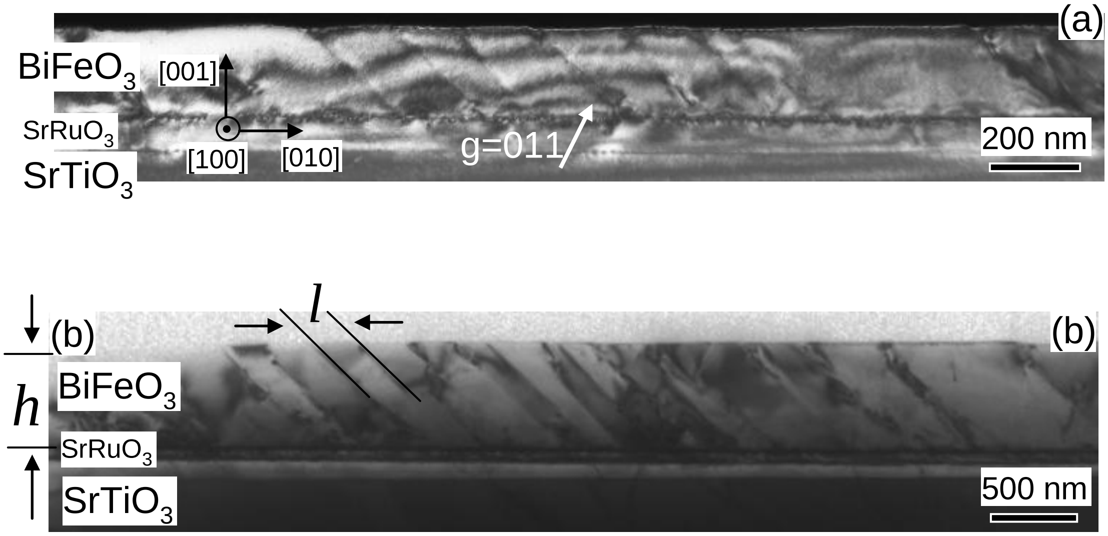

Fig. 3.9 (a) The dark field image of 200 nm $BiFeO_3$ thin films grown on 4° miscut $SrTiO_3$ substrate showing the 71° ferroelectric domains lamellae. (b) The bright-field image of 600 nm $BiFeO_3$ thin films grown on 4° miscut $SrTiO_3$ substrate with 100 nm $SrRuO_3$ bottom electrode showing 71° ferroelectric domains lamellae.

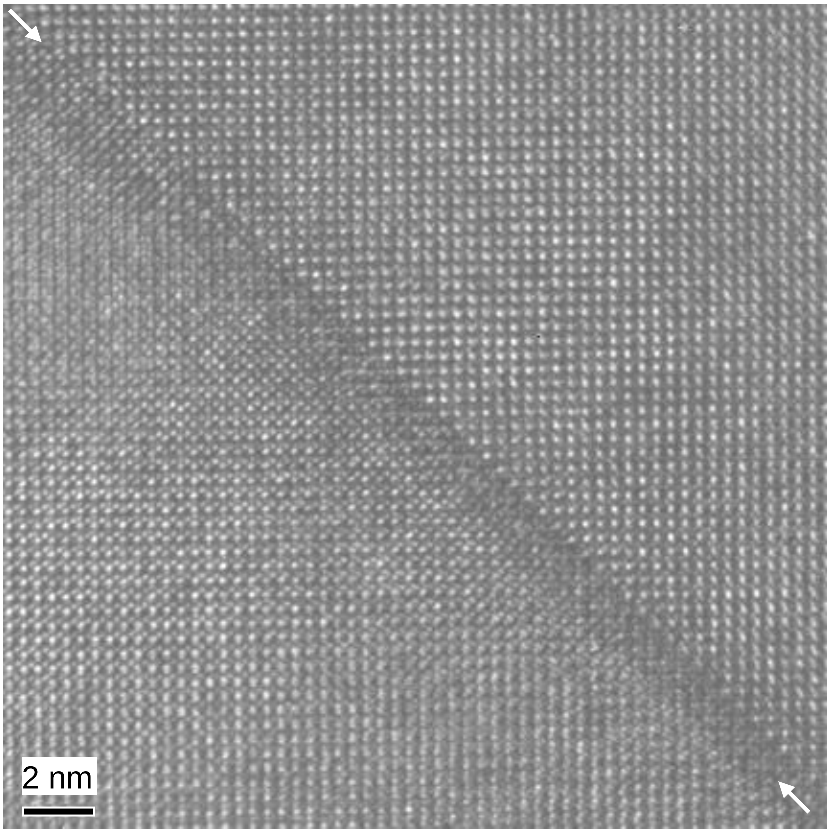

Fig. 3.10 The high-resolution TEM micrograph of 71° ferroelectric domain wall in $BiFeO_3$ thin films grown on 4° miscut $SrTiO_3$ substrate showing the atomic distortion around the ferroelectric domain wall.

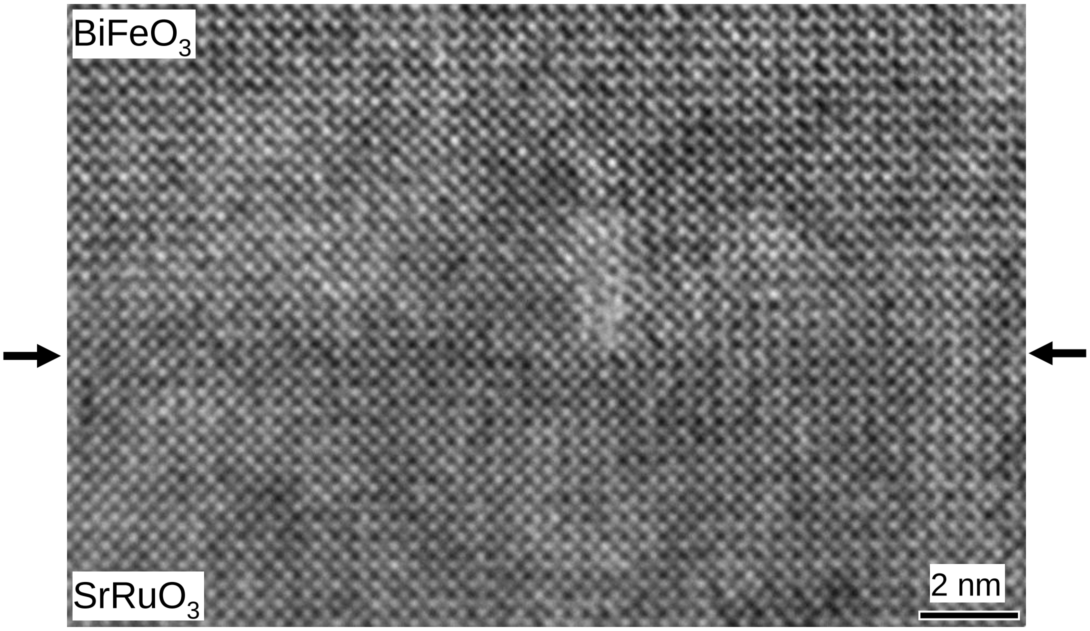

Fig. 3.11 The atomic structure of a misfit dislocation at $BiFeO_3$/$SrRuO_3$ interface in sample 200 nm $BiFeO_3$ grown on 4° miscut $SrTiO_3$ substrate with 100 nm $SrRuO_3$ electrode.

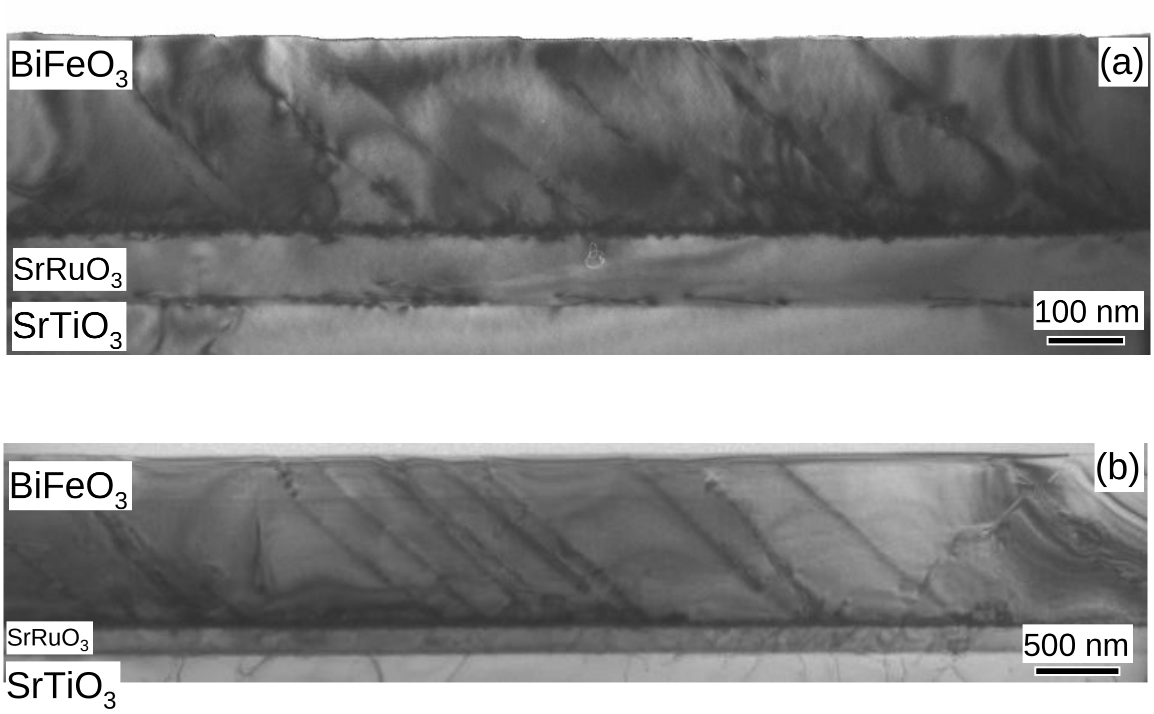

Fig. 3.12 (a) The bright-field image for 450 nm BiFeO$_3$ grown on 4° miscut SrTiO$_3$ substrate with 100 nm SrRuO$_3$ electrode showing 71° ferroelectric domain lamellae. (b) The bright-field image for 1000 nm BiFeO$_3$ thin film grown on 4° miscut SrTiO$_3$ substrate with 100 nm SrRuO$_3$ electrode showing 71° ferroelectric domain lamellae.

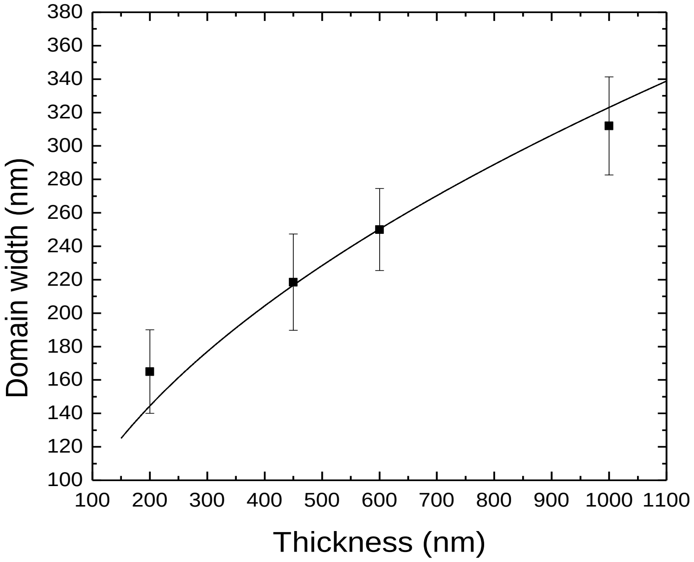

Fig. 3.13 The relationship between domain width and thin film thickness. The discrete spots are experimental results and solid curve is fitting results.

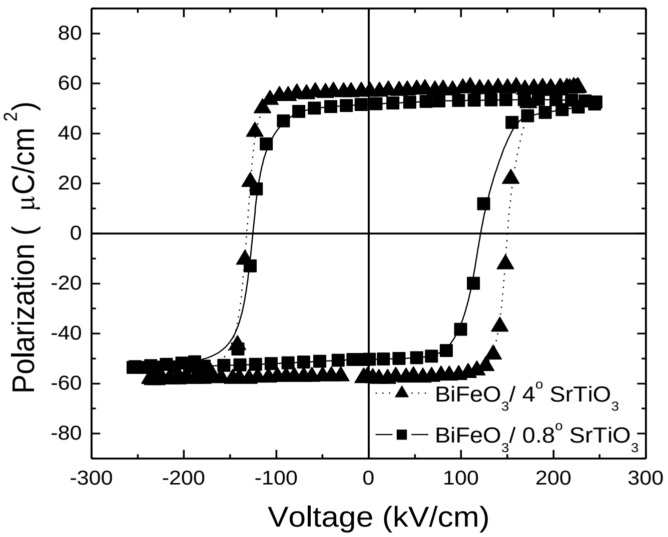

Fig. 3.14 The ferroelectric hysteresis loops of 600 nm $BiFeO_3$ thin films grown on 0.8° (solid-square curve) and 4° (dot-triangle curve) miscut $SrTiO_3$ substrates with 100 nm $SrRuO_3$ electrodes.[21]

3.7. References

[1] S. M. Skinner, “Magnetically ordered ferroelectric materials,” IEEE Transaction on parts, materials and packaging, **6**, 68 (1970).

[2] W. Prellier, M. P. Singh, and P. Murugavel, “The single-phase multiferroic oxides: from bulk to thin film,” J. Phys.: Condens. Matter., **17**, R803 (2005).

[3] M. Fiebig, “Revival of the magnetoelectric effect,” J. Phys. D: Appl. Phys., **38**, R123 (2005).

[4] R. Ramesh, and N. A. Spaldin, “Multiferroics: progress and prospects in thin films,” Nature Materials, **6**, 21 (2007).

[5] C. Ederer, and N. A. Spaldin, “Recent progress in first-principles studies of magnetoelectric multiferroics,” Current Opinion in Solid State and Materials Science, **9**, 128 (2005).

[6] W. Eerenstein, N. D. Mathur, and J. Scott, “Multiferroic and magnetoelectric materials,” Nature, **44**, 759 (2006).

[7] There is a focus issue for multiferroics at Journal of Materials Research in August, 2007.

[8] X. Tan, T. Du, and J. K. Shang, “Piezoelectric in-situ transmission electron microscopy technique for direct observations of fatigue damage accumulation in constrained metallic thin films,” Appl. Phys. Lett., **80**, 3946 (2002).

[9] Y. B. Chen, M. B. Katz, X. Q. Pan, R. R. Das, D. M. Kim, S. H. Baek, and C. B. Eom, “Ferroelectric domain structures of epitaxial (001) $BiFeO_3$ thin films,” Appl. Phys. Lett., **90**, 072907 (2007).

[10] C. Michel, J.M. Moreau, G. D. Achenbach, R. Gerson, and W. J. James, “The atomic structure of $BiFeO_3$,” Solid State Comm., **7**, 701 (1969).

[11] C. Blaauw, and F. V. D. Woude, “Magnetic and structural properties of $BiFeO_3$,” J. Phys. C: Solid State Phys., **6**, 1422 (1973).

[12] J. Wang, J. B. Neaton, H. Zheng, V. Nagarajan, S. B. Ogale, B. Liu, D. Viehland, V. Vaithyanathan, D. G. Schlom, U. V. Waghmare, N. A. Spaldin, K. M. Rabe, M. Wuttig, and R. Ramesh, "Epitaxial $BiFeO_3$, multiferroic thin films heterostructures," Science, **299**, 1719 (2003).

[13] W. Eerenstein, F. D. Morrison, J. Dho, M. G. Blamire, J. F. Scott, and N. D. Mathur, "Comment on "Epitaxial $BiFeO_3$ multiferroic thin film heterostructures," Science, **307**, 1203 (2005).

[14] J. Wang, A. Scholl, H. Zheng, S. B. Ogale, D. Viehland, D. G. Schlom, N. A. Spaldin, K. M. Rabe, M. Wuttig, L. Mohaddes, J. Neaton, U. Waghmare, T. Zhao, and R. Ramesh, "Response to comment on "Epitaxial $BiFeO_3$ multiferroic thin film heterostructures," Science, **307**, 1203 (2005).

[15] S. K. Singh, R. Ueno, H. Funakubo, H. Uchida, S. Koda, and H. Ishiwara, "Dependence of ferroelectric properties on thickness of $BiFeO_3$ thin films fabricated by chemical solution deposition," Jap. J. Appl. Phys., **44**, 8525 (2005).

[16] Z. L. Liu, H. R. Liu, G. H. Du, J. Zhang, and K. L. Yao, "Electric properties of $BiFeO_3$ films deposited on $LaNiO_3$ by sol-gel process," J. Appl. Phys., **100**, 044110 (2006).

[17] S. Habouti, C. Solterbeck, and M. Es-Souni, "Surface scanning probe microscopy investigation of solution deposited $BiFeO_3$ thin films," Appl. Phys. Lett., **88**, 262903 (2006).

[18] S. K. Singh, Y. K. Kim, H. Funakubo, and H. Ishiwara, "Epitaxial $BiFeO_3$ thin films fabricated by chemical solution deposition," Appl. Phys. Lett., **88**, 162904 (2006).

[19] S. K. Singh, R. Ueno, H. Funakubo, H. Uchida, S. Koda, and H. Ishiwara, "Dependence of ferroelectric properties on thickness of $BiFeO_3$ thin films fabricated by chemical solution deposition," Jap. J. Appl. Phys., **44**, 8525 (2005).

[20] S. K. Singh, H. Ishiwara, "Reduced leakage current in $BiFeO_3$ thin films on Si substrates formed by a chemical solution method," Jap. J. Appl. Phys., **44**, L734 (2005).

[21] R. R. Das, D. M. Kim, S. H. Baek, C. B. Eom, F. Zavaliche, S. Y. Yang, R. Ramesh, Y. B. Chen, X. Q. Pan, X. Ke, M. S. Rzchowski and S. K. Streiffer, " Synthesis and ferroelectric properties of epitaxial $BiFeO_3$ thin films grown by sputtering," Appl. Phys. Lett., **88**, 242904 (2006).

[22] J. F. Ihlefeld, A. Kumar, V. Gapalan, D. G. Schlom, Y. B. Chen, X. Q. Pan, T. Heeg, J. Schubert, X. Ke, P. Schiffer, J. Orenstein, L. W. Martin, Y. H. Chu, and R. Ramesh, "Adsorption-controlled molecular-beam epitaxial growth of $BiFeO_3$," Appl. Phys. Lett., **91**, 071922 (2007).

[23] J. Kabelac, S. Ghosh, P. S. Dobal, and R. Katiyar, "RF oxygen plasma assisted molecular beam epitaxy growth of $BiFeO_3$ thin films on $SrTiO_3$ (001)," J. Va. Sci. Technol. B, **25**, 1049 (2007).

[24] K. Y. Yun, D. ricinschi, T. Kanashima, M. Noda, and M. Okuyama, "Giant ferroelectric polarization beyond 150 μC/cm^2 in $BiFeO_3$ thin film," Jap. J. Appl. Phys., **43**, L647, (2004).

[25] D. Ricinschi, K. Y. Yun, and M. Okuyama, "A mechanism for the 150 μC/cm^2 polarization of $BiFeO_3$ films based on first-principles calculations and new structural data," J. Phys.: Condens Matters, **18**, L97 (2006).

[26] W. Tian, V. Vaithyanathan, D. G. Schlom, Q. Zhan, S. Y. Yang, Y. H. Chu, and R. Ramesh, "Epitaxial integration of (0001) $BiFeO_3$ with (0001)GaN," Appl. Phys. Lett., **90**, 172908 (2007).

[27] S. R. Shannigrahi, A. Huang, N. Chandrasekhar, D. Tripathy, and A. O. Adeyeye, "Sc modified multiferroic $BiFeO_3$ thin films prepared through a sol-gel process," Appl. Phys. Lett., **90**, 022901 (2007).

[28] Y. Wang, and C. W. Nan, "Enhanced ferroelectricity in Ti-doped multiferroic $BiFeO_3$ thin films," Appl. Phys. Lett., **89**, 052903 (2006).

[29] X. D. Qi, J. Dho, R. Tomov, M. G. Blamire, and J. L. MacManus-Driscoll, "Greatly reduced leakage current and conduction mechanism in aliovalent-ion-doped $BiFeO_3$," Appl. Phys. Lett., **86**, 062903 (2005).

[30] S. K. Singh, H. Ishiwara, and K. Maruyama, "Room temperature ferroelectric properties of Mn-substituted $BiFeO_3$ thin films deposited on Pt electrodes using chemical solution deposition," Appl. Phys. Lett., **88**, 262908 (2006).

[31] J. K. Kim, S. S. Kim, W. J. Kim, A. S. Bhalla, and R. Guo, "Enhanced ferroelectric properties of Cr-doped $BiFeO_3$ thin films grown by chemical solution deposition," Appl. Phys. Lett., **88**, 132901 (2006).

[32] M. Murakami, S. Fujino, S. H. Lim, L. G. Salamanca-Riba, M. Wuttig, I. Takeuchi, B. Varughese, H. Sugaya, T. Hasegawa, and S. E. Lofland, "Microstructure and phase control in Bi-Fe-O multiferroic nanocomposite thin films," Appl. Phys. Lett., **88**, 112505 (2006).

[33] F. Tyholdt, H. Fjellvag, A. E. Gunnas and A. Olsen, "Synthesis of epitaxial $BiFeO_3$ films by chemical solution deposition on Pt (100)," J. Appl. Phys., **102**, 074108 (2007).

[34] Y. H. Lin, Q. H. Jiang, Y. Wang, C. W. Nan, L. Chen, and J. Yu, "Enhancement of ferromagnetic properties in $BiFeO_3$ polycrystalline ceramic by La doping," Appl. Phys. Lett., **90**, 172507 (2007).

[35] S. K. Singh, R. Ueno, H. Funakubo, H. Uchida, S. Koda, and H. Ishiwara, "Dependence of ferroelectric properties on thickness of $BiFeO_3$ thin films fabricated by chemical solution deposition," Jap. J. Appl. Phys., **44**, 8525 (2005).

[36] C. Tabares-Munoz, J. P. Rivera, and H. Schmid, "Ferroelectric domains, Birefringence and absorption of single crystals of $BiFeO_3$," Ferroelectrics, **55**, 235 (1984).

[37] F. Kubel and H. Schmid, "Growth, twining and etch figures of ferroelectric/ferroelastic dendritic $BiFeO_3$ single domain crystals," J. Crystal growth, **129**, 515 (1993).

[38] F. Zavaliche, R. R. Das, D. M. Kim, C. B. Eom, S. Y. Yang, P. Shafer, and R. Ramesh, "Ferroelectric domain structure in epitaxial $BiFeO_3$ films," Appl. Phys. Lett., **87**, 182912 (2005).

[39] F. Zavaliche, P. Shafer, R. Ramesh, M. P. Cruz, R. R. Das, D. M. Kim, and C. B. Eom, "Polarization switching in epitaxial $BiFeO_3$ films," Appl. Phys. Lett., **87**, 252902 (2005).

[40] Y. H. Chu, T. Zhao, M. P. Cruz, Q. Zhan, P. L. Yang, L. W. Martin, M. Huijben, C. H. Yang, F. Zavallche, H. Zheng, and R. Ramesh, "Ferroelectric size effects in multiferroic $BiFeO_3$ thin films," Appl. Phys. Lett., **90**, 252906 (2007).

[41] P. Shafer, F. Zavaliche, Y. H. Chu, P. L. Yang, M. P. Cruz, and R. Ramesh, "Planar electrode piezoelectric force microscopy to study electric polarization switching in $BiFeO_3$," Appl. Phys. Lett., **90**, 202909 (2007).

[42] T. Zhao, A. Scholl, F. Zavaliche, K. Lee, M. Barry, A. Doran, M. P. Cruz, Y. H. Chu, C. Ederer, N. A. Spaldin, R. R. Das, D. M. Kim, S. H. Baek, C. B. Eom, and R. Ramesh, "Electrical control of antiferromagnetic domains in multiferroic $BiFeO_3$ films at room temperature," Nature materials, **5**, 823 (2006).

[43] S. B. Desu, Z. J. Chen, "The phase diagram of epitaxial $BaTiO_3$ films under bi-axial stress," Mat. Res. Soc. Symp. Proc., **433**, 345 (1996).

[44] A. Y. Emelyanov, N. A. Pertsev, and A. L. Kholkin, "Effect of external stress on ferroelectricity in epitaxial thin films," Phys. Rev. B., **66**, 214108 (2002).

[45] J. Wang, and T. Y. Zhang, "Effects of nonequally biaxial misfit strains on the phase diagram and dielectric properties of epitaxial ferroelectric thin films," Appl. Phys. Lett., **86**, 192905 (2005).

[46] N. A. Pertsev, A. G. Zembilgotov, and A. K. Tagantsev, "Effect of mechanical boundary conditions on phase diagrams of epitaxial ferroelectric thin films," Phys. Rev. Lett., **80**, 1988 (1998).

[47] J. S. Speck, A. C. Daykin, A. Seifert, A. E. Romanov, and W. Pompe, “Domain configurations due to multiple misfit relaxation mechanisms in epitaxial ferroelectric thin films. III. Interfacial defects and domain misorientations,” J. App. Phys., **78**, 1696 (1995).

[48] V. Srikant, E. J. Tarsa, D. R. Clarke, and J. S. Speck, “Crystallographic orientation of epitaxial $BaTiO_3$ films: The role of thermal-expansion mismatch with the substrate,” J. Appl. Phys., **77**, 1517 (1995).

[49] J. S. Speck, and W. Pompe, “Domain configurations due to multiple misfit relaxation mechanisms in epitaxial ferroelectric thin films. I. Theory,” J. Appl. Phys., **76**, 466 (1994).

[50] S. K. Streiffer, C. B. Parker, A. E. Romanov, M. J. Lefevre, L. Zhao, J. S. Speck, W. Pompe, C. M. Foster, and G. R. Bai, “Domain patterns in epitaxial rhombohedral ferroelectric films. I. Geometry and experiments,” J. Appl. Phys., **83**, 2742 (1998).

[51] A. E. Romanov, M. J. Lefevre, J. S. Speck, W. Pompe, S. K. Streiffer and C. M. Foster, “Domain pattern formation in epitaxial rhombohedral ferroelectric films. II. Interfacial defects and energetic,” J. Appl. Phys., **83**, 2754 (1998).

[52] N. Farag, M. Bobeth, W. Pompe, A. E. Romanov and J. S. Speck, “Modeling of twinning in epitaxial {001}-oriented $La_{0.67}Sr_{0.33}MnO_3$ thin films,” J. Appl. Phys., **97**, 113516 (2005).

[53] J. Fousek, and V. Janovec, “The orientation of domain walls in twinned ferroelectric crystals,” J. Appl. Phys., **40**, 135 (1969).

[54] Y. G. Wang, W. L. Zhong, and P. L. Zhang, “Surface and size effects on ferroelectric films with domain structures,” Phys. Rev. B, **51**, 5311 (1995).

[55] C. Kittel, “Theory of the structure of ferromagnetic domains in films and small particles,” Phys. Rev., **70**, 965 (1946).

[56] A. L. Roitburd, “Equilibrium structure of epitaxial layers,” Phys. Stat. Sol. (a). **37**, 329 (1976).

[57] L. Landau, and E. M. Lifshiz, “*Electrodynamics of continuous media*,” (Academic Press, New York, second edition).

[58] C. A. Randall, D. J. Barber, and R. W. Whatmore, “Ferroelectric domain configurations in a modified-PZT ceramic,” J. Mater. Sci., **22**, 925 (1987).

[59] D. G. Schlom, L. Q. Chen, C. B. Eom, K. M. Rabe, S. K. Streiffer, and J. M. Triscone, “Strain tuning of ferroelectric thin films,” Annu. Rev. Mater. Res., **37**, 589 (2007).

[60] R. L. Byer, "Quasi-phase matched nonlinear interactions and devices," J. Nonlinear Opt., **6**, 549 (1997).

[61] S. N. Zhu, Y. Y. Zhu, and N. B. Ming, "Quasi-phase-matched third-harmonic generation in a quasi-periodic optical superlattice," Science, **278**, 843 (1997).

[62] J. L. he, J. Liao, H. Liu, J. Du, F. Xu, H. T. Wang, S. N. Zhu, Y. Y. Zhu, and N. B. Ming, "Simultaneous cw red, yellow, and green light generation, "traffic signal lights," by frequency doubling and sum-frequency mixing in a aperiodically poled $LiTaO_3$," Appl. Phys. Lett., **83**, 228 (2003).

[63] V. Nagarajan, A. roytburd, A. Stanishevsky, S. Prasertchoung, T. Zhao, L. Chen, J. Melngailis, O. Auciello, and R. Ramesh, "Dynamics of ferroelastic domains in ferroelectric thin films," Nature materials, **2**, 43, (2002).

[64] G. Y. Xu, Z. Zhong, Y. Bing, Z. G. Ye, and G. Shirane, "Electric-field-induced redistribution of polar nano-regions in a relaxor ferroelectric," Nature materials, **5**, 134 (2006).

[65] V. Nagarajan, C. S. Ganpule, H. Li, L. Salamanca-Riba, A. L. Roytburd, E. D. Williams, and R. Ramesh, "Control of domain structure of epitaxial $PbZr_{0.2}Ti_{0.8}O_3$ thin films grown on vicinal (001) $SrTiO_3$ substrates," Appl. Phys. Lett., **79**, 2805 (2001).

[66] Y. H. Chu, Q. Zhan, L. W. Martin, M. P. Cruz, P. L. yang, G. W. Pabst, F. Zavaliche, S. Y. Yang, J. X. Zhang, L. Q. Chen, D. G. Schlom, I. N. Lin, T. B. Wu and R. Ramesh, "Nanoscale domain control in multiferroic $BiFeO_3$ thin films," Adv. Mater., **18**, 2307 (2006).

[67] R. Ricci, M. F. Bevilacqua, F. M. Granozio, and U. S. D. Uccio, "Mechanism of single-domain selection in epitaxial $CaRuO_3$ thin films," Phys. Rev. B., **65**, 155428 (2002).

[68] W. Hong, H. N. Lee, M. Yoon, H. M. Christen, D. H. Lowndes, Z. G. Suo, and Z. Y. Zhang, "Persistent step-flow growth of strained films on vicinal substrates," Phys. Rev. Lett., **95**, 095501 (2005).

CHAPTER 4

STRAIN RELAXATION OF $BaTiO_3$ THIN FILMS GROWN ON SMALL LATTICE-MISMATCHED SUBSTRATES

4.1 Introduction

Mechanical strain can have a dramatic effect on the many physical properties of materials, which is much more significant in epitaxial thin films. This is because, in this scenario, the lattice mismatch and thermal expansion coefficient difference between thin films and substrates naturally provide the mechanical strain in coherent thin films. Three typical examples of physical properties enhanced by mechanic strain are given as following. Locquet *et al*. reported a doubled critical temperature in thin film of the high temperature superconductor $La_{1.9}Sr_{0.1}CuO_4$ by means of epitaxial strain.[1] Coherent $La_{1.9}Sr_{0.1}CuO_4$ film grown on $SrLaAlO_4$ substrate (lattice mismatch is 0.63 % in this case) has Curie temperature of 49 K with respect to 25 K in its bulk counterpart.[1] Haeni *et al*. observed the ferroelectric transition temperature in strained $SrTiO_3$ thin films at room temperature.[2] The critical step in this work is to use new developed $DyScO_3$ substrate, which has only 0.5 % lattice mismatch and relative small thermal expansion difference with $SrTiO_3$. Zhao *et al*. studied the enhanced optical nonlinearity in strained $BaTiO_3$ thin films.[3] They grew $BaTiO_3$ /$SrTiO_3$ and Ce-doped $BaTiO_3$/$SrTiO_3$ superlattice by molecular beam epitaxial. The effective second-harmonic generation coefficient d_{33} of coherent $BaTiO_3$ thin films has one order of magnitude larger than that in bulk counterpart. From above-mentioned examples, it is evident that strain in functional oxide thin films does enhance some physical properties with respect to strain-free counterparts.

Recently, we grew highly coherent and strain-partially relaxed $BaTiO_3/SrRuO_3$ bilayer on $GdScO_3$ and $DyScO_3$ substrates by pulsed laser deposition.[4] This chapter describes our studies of the strain relaxation in $BaTiO_3$ thin films grown on three small lattice-mismatched substrates ($GdScO_3$, $DyScO_3$ and $SrTiO_3$) with strained/strain-partially relaxed $SrRuO_3$ bottom electrodes by transmission electron microscopy. The strain relaxation mechanism is discussed by means of thermodynamic method.

4.2. Background and literature review

It is out of scope of this chapter to summarize the strain effect on physical properties of ferroelectric oxide thin films. We only summarize previous experimental and theoretical study of strain effect on $BaTiO_3$ thin films (including monolayer & multilayer morphologies) in this section. In principle, strain relaxation of $BaTiO_3$ thin films is directly correlated to strain effects. Strain relaxation and strain effect on $BaTiO_3$ thin films therefore should be summarized together. But some work, especially theoretical work, is mainly focused on strain effect on $BaTiO_3$ thin films. In these work, the researchers assume simply that thin films are strained under substrates' constraint. For the sake of clarity, we separately summarized strain relaxation and strain effects on $BaTiO_3$ thin films. In addition, we will use critical thickness calculation to discuss strain relaxation in $BaTiO_3/SrRuO_3$ bilayer in this chapter. Two critical thickness calculation models (Matthews-Blakeslee and People-Bean models) were summarized as well.

4.2.1 Strain effects on ferroelectric properties in $BaTiO_3$ thin films

A. Theoretical calculation

$BaTiO_3$ is well known as a classic example of displacement ferroelectric materials.[5] The origin of spontaneous polarization in displace ferroelectric materials is attributed to the atomic shift of the cation Ti^{4+} of 0.006 nm along c-axis with respect to center position in a standard cubic perovskite structure. At the same time, the O^{2-} anion has the opposite displacement along the same axis. Thus, a net microscopic polarization is formed. Normally, tensile and compressive strains have different effect on coherent $BaTiO_3$ thin films. In detail, biaxial tensile strain depresses the spontaneous polarization and ferroelectric-paraelectric phase transition temperature, while enhancement of polarization and Curie temperature can be realized under biaxial compressive strain.[6-15] The results via first-principle calculation, thermodynamic Landau-Devonshire and phase-field theory are summarized as following. For example, Neaton *et al*. studied the effect of compressive strain on ferroelectric properties in $BaTiO_3$ thin films by means of first principles calculation.[6,7] In their calculation, a strain state is formed in the epitaxial $BaTiO_3/SrTiO_3$ superlattice. The electric polarization enhancement in ferroelectric superlattice is discussed on different thickness ratio between $BaTiO_3$ and $SrTiO_3$. It is because that the different thickness ratio between $BaTiO_3$ and $SrTiO_3$ represents the degree of compressive strain to $BaTiO_3$. The calculation proves that the large tetragonality in $BaTiO_3$ is enhanced by nearly 70% for the compressive misfit strain of (-2.28%). Nakhmanson *et al*. also studied similar problem by first principles calculations.[8] In their calculations, the polar properties in epitaxial short-period ternary $CaTiO_3$/$SrTiO_3$/$BaTiO_3$ superlattice is investigated. Polarization enhancement with respect to bulk $BaTiO_3$ is also found in this system. In addition, the degree of inversion-symmetry breaking in three-component superlattice can be controlled by varying the thickness of the component layers.

Besides the first principle calculations, there are some theoretical discussions of the same problem based on thermodynamics.[11-16] Considering the coupling between electric polarization and lattice strain in a film/substrate system, the Gibbs free energy can be expanded by Landau-Devonshire series as:[11,12]

$$\begin{aligned}
G = {} & a_1\left(P_1^2 + P_2^2 + P_3^2\right) + a_{11}\left(P_1^4 + P_2^4 + P_3^4\right) + a_{12}\left(P_1^2P_2^2 + P_2^2P_3^2 + P_1^2P_3^2\right) \\
& + a_{111}\left(P_1^6 + P_2^6 + P_3^6\right) + a_{112}\left[P_1^4\left(P_2^2 + P_3^2\right) + P_2^4\left(P_1^2 + P_3^2\right) + P_3^4\left(P_1^2 + P_2^2\right)\right] \\
& + a_{123}P_1^2P_2^2P_3^2 - \frac{1}{2}s_{11}\left(\sigma_1^2 + \sigma_2^2 + \sigma_3^2\right) - s_{12}\left(\sigma_1\sigma_2 + \sigma_2\sigma_3 + \sigma_3\sigma_1\right) \\
& - \frac{1}{2}s_{44}\left(\sigma_4^2 + \sigma_5^2 + \sigma_6^2\right) - Q_{11}\left(\sigma_1P_1^2 + \sigma_2P_2^2 + \sigma_3P_3^2\right) \\
& - Q_{12}\left[\sigma_1\left(P_2^2 + P_3^2\right) + \sigma_2\left(P_1^2 + P_3^2\right) + \sigma_3\left(P_1^2 + P_2^2\right)\right] - Q_{44}\left(\sigma_4P_2P_3 + \sigma_5P_1P_3 + \sigma_6P_1P_2\right)
\end{aligned} \tag{4.1}$$

Where G is the free energy, P_1, P_2, P_3 are spontaneous polarization along x, y and z direction, respectively. σ_i is the stress element. s_{ij} is electrostrictive coefficient. a_1 is expressed as $a_o\left(T - T_c\right)$ (T and T_c are temperature and Curie temperature of ferroelectric-to-paraelectric phase transition in ferroelectric materials, respectively), where the temperature effect is considered. Accounting for mechanical and electric boundary conditions, the relationship between strain and spontaneous polarization, as well as strain-dependent Curie temperature can be obtained by minimizing Gibbs free energy. In detail, the mechanical boundary conditions are:[11,12]

$$\frac{\partial G}{\partial \sigma_1} = \frac{\partial G}{\partial \sigma_2} = -u_m \quad \frac{\partial G}{\partial \sigma_6} = 0 \tag{4.2a}$$

$$\sigma_3 = \sigma_4 = \sigma_5 = 0 \tag{4.2b}$$

where u_m is a strain element induced by lattice mismatch between film and substrate. And the minimization of Gibbs free energy can be obtained as:

$$\frac{\partial G}{\partial P_i} = 0 \ (i = 1,2,3) \tag{4.3}$$

Combined equations (4.2) and (4.3), the "misfit strain-temperature" phase diagram of (001) $BaTiO_3$ thin films can be obtained, which is shown in Fig. 4.1.[16] In this diagram, the possible domain patterns are indicated. As shown in Fig. 4.1, the compressive strain will keep spontaneous polarization along c-axis. However, under tensile stress, the novel ferroelectric state (a/b phase) can be realized. In other word, the spontaneous polarization in coherent $BaTiO_3$ under tensile stress has component along a-b plane. This novel ferroelectric state stems from mechanical strain, which is different from multi-domain structures in strain relaxed $BaTiO_3$.[16]

As for effects of compressive strain on the Curie temperature in coherent (001) $BaTiO_3$ (c-type single domain) thin films, the Gibbs free energy in equation (4.1) can be simplified to:[4,17]

$$G = \left(a_1 - \frac{2Q_{12}\varepsilon_s}{s_{11}+s_{12}} \right) P_3^2 + \left(a_{11} + \frac{Q_{12}^2}{s_{11}+s_{12}} \right) P_3^4 + a_{111}P_3^6 + a_{1111}P_3^8 + \frac{\varepsilon_s^2}{s_{11}+s_{12}} \tag{4.4}$$

The in-plane compressive strain effect has been considered in terms related to ε_s. To obtain Eq. (4.4), the small spontaneous polarization around the Curie temperature has been considered. Therefore, the dependence of Curie temperature on in-plane compressive strain can be expressed as:[4]

$$T_c = \theta + 4\varepsilon_o C \frac{Q_{12}}{s_{11} + s_{12}} \varepsilon_s \qquad (4.5)$$

Where θ and C are the Curie temperature and Curie-Weiss constant, respectively. s_{11} and s_{12} are elastic compliances. Q_{12} is the electrostrictive coefficient. The parameters in this equation have been experimentally measured. However, the values are varied in different papers.[17] The upper and lower limits of Curie temperatures under different compressive strains, by considering the variances in expansion coefficients, are shown in Fig. 4.2.

B. Experimental study

Although there are many theoretical works of strain effect on ferroelectric thin films, comparisons between these theoretical and experimental results have been available only recently. Schlom *et al*. grew $BaTiO_3/SrTiO_3$ superlattices with high crystalline quality by molecular beam epitaxy (MBE).[18] To realize layer-by-layer growth, they used an atomic absorption spectroscopy to *in-situ* monitor the flux of all elements during the MBE growth, and then shutter-controlled and adsorption-controlled growth was developed to grow ferroelectric superlattices. The details for experimental setup and growth condition can be find in reference.[18] Tian *et al*. used the quantitative high-resolution TEM to study $BaTiO_3/SrTiO_3$ superlattices grown by MBE.[19] Tetragonal ratio (c/a) of $BaTiO_3$ layer in superlattices was measures as 1.05, in contrast to 1.013 in bulk counterpart. The enhancement of ferroelectric properties is supported by phase-field and first principles calculations. However, direct electrical measurements of these samples were hampered by large current leakage that probably stems from oxygen vacancies.

Shimuta *et al*. used pulsed laser deposition to grow asymmetric $BaTiO_3$/$SrTiO_3$ strained superlattices.[20] The largest remnant polarization of 46 μC/cm^2 was measured in a superlattice which has stacking periodicity of 15 unit cells $BaTiO_3$ / 3 unit cells $SrTiO_3$. The increase in the remnant polarization is attributed to the $BaTiO_3$-rich structure and strain effects. Yanase *et al*. studied the thickness dependence of ferroelectricity in epitaxial $BaTiO_3$ thin films.[21] Their study proves that ferroelectric hysteresis loop can be measured even in 12 nm $BaTiO_3$ thin films. In addition, the Curie temperature can be increased to 200 °C (it is 120 °C in bulk counterpart[5]), which is explained by misfit strain. Lee *et al*. reported a strong polarization enhancement in asymmetric three-component ferroelectric superlattices.[22] a three-component superlattice ($BaTiO_3$ / $SrTiO_3$ / $CaTiO_3$) was grown layer-by-layer by pulsed laser deposition. Highly coherent interfaces among superlattice were corroborated by Scanning transmission electron microscopy (STEM) and x-ray diffraction (XRD) observations. The enhancement of ferroelectric properties is attributed to the mechanical strain in three-component superlattices.

4.2.2. Strain relaxation study in $BaTiO_3$ thin films

Strain relaxations in monolayer $BaTiO_3$ thin films are summarized in this section. Sun *et al*. studied the evolution of dislocation arrays in $BaTiO_3$ thin films grown on (001) $SrTiO_3$ substrates by MBE. TEM characterization corroborates that the critical thickness in this system is between 2 and 4 nm. The majority of misfit dislocations belongs to <100> type.[23] Suzuki *et al*. systematically studied this problem by TEM, XRD and atomic force microscopy (AFM).[24] Both <100>-type threading and <110>-type misfit dislocations were observed in these $BaTiO_3$ thin films. In addition, the dissociation of <110>-type dislocations was also observed in thick (>=100 nm) $BaTO_3$ thin films. The dissociation generates the stacking fault with displacement vector of 1/2a<101>. They believed that the strain relaxation is attributed to the generation and evolution of dislocation half-loop in $BaTiO_3$ thin films. Visinoiu *et al*. studied the initial growth stage of epitaxial $BaTiO_3$ films on vicinal (001) $SrTiO_3$ substrates.[25] X-ray diffraction and cross sectional high-resolution transmission electron microscopy revealed well-defined epitaxial films and a sharp interface between $BaTiO_3$ and substrates. The layer-then-island growth model is employed to explain the observed morphology. Chen *et al*. studied the strain relaxation of $BaTiO_3$ thin films that were grown on $LaAlO_3$ substrates by metal-organic chemical vapor deposition (MOCVD).[26] $BaTiO_3$ thin films display (100) orientated growth in this case. Lattice mismatch strain is mainly relaxed by formation of misfit dislocations. Lei *et al*. reported a series of papers to study the strain relaxation of $BaTiO_3$ thin films grown on MgO, MgO-buffered R-cut sapphire and (001) $MgAl_2O_4$ substrates.[27-29] $BaTiO_3$ thin films were deposited by laser ablation at different temperatures under oxygen pressure of 2×10^{-3} mbar. Different strain relaxation behavior was observed in $BaTiO_3$ thin films grown on different substrates. The strain relaxation in $BaTiO_3$ grown on MgO substrate is mainly due to formation of {111} stacking faults and nanotwins in $BaTiO_3$ thin films. TEM studies prove that the stacking faults and nanotwins are bounded by partial dislocations. The partial dislocations are classified as Shockley type (a/3) <112> and Frankel type (a/3) <111> in this system. The movement of these plane defects and interaction among them are also discussed. In the case of $BaTiO_3$ thin films grown on (001) $MgAl_2O_4$ substrates, $BaTiO_3$ films grown at 850 °C show the columnar structure.[29] But when the growth temperature is increased to 900 °C, epitaxial $BaTiO_3$ thin films can be obtained. In epitaxial $BaTiO_3$ films, stacking faults and twins are the predominant strain relaxation defects in this system. The formation of these planar defects is attributed to the atomic steps on the substrate surfaces.

4.2.3 Theoretic critical thickness in thin films

A. Matthew model

Strain relaxation in thin films is a critical problem not only in application but also in fundamental science.[30] The study of strain relaxation in semiconductor thin films can be traced back to J. H. Van der Merwe and F. C. Frank's classic works.[31,32] In their work, they proposed an important parameter-critical thickness. The critical thickness is a criterion of determining whether misfit strain will relax or not. When the thickness of a thin film is smaller than the critical thickness, the mechanical strain between thin film and substrate is sustained. However, the strain in thin film is relaxed by the dislocations formation when thin film thickness is larger than critical thickness. The remaining problem is to how to predict the critical thickness in theory. Their work was extended substantially in Matthews's papers.[33-35] In these papers, the classic Matthews method is proposed. The critical thickness is calculated in the condition where the force exerted by the misfit strain is equal to tension in the dislocation lines.[33] Therefore, the critical thickness, h_c, is satisfied in this equation

$$h_c = \frac{b}{2\pi f} \frac{\left(1 - \nu \cos^2 \alpha\right)}{\left(1 + \nu\right) \cos \lambda} \left(\ln \frac{h_c}{b} + 1 \right) \tag{4.6}$$

Where f is the lattice mismatch between film and substrate, b is the magnitude of Burgers vector, v is the Poisson ratio. α is the angle between the Burgers vector and the dislocation-line direction. λ is the angle between the Burgers vector and the direction in the interface perpendicular to the dislocation line.

B. People-Bean model

Besides Matthew's mechanical model, there is a People-Bean's energy model. This model was proposed to explain the large deviation between experimental and theoretical results in Ge_xSi_{1-x} thin films grown by MBE. The experiments prove that the thickness of coherent Ge_xSi_{1-x}, grown on Si substrates, is as much as an order of magnitude larger than that predicted by Mathew's method, especially in the case of lattice mismatch less than 0.5 %.[36,37] In the People-Bean mode, the critical thickness is defined as the thickness at which the strain energy is equal to dislocation energy. The critical thickness h_c can be calculated as:[36]

$$2G\frac{(1+v)}{(1-v)}h_c f^2 = \frac{Gb^2}{4\pi d}\ln\left(\frac{h_c}{b}\right) \qquad (4.7)$$

where G is the Young's modulus. f is the lattice mismatch between films and substrate; b and d are the magnitude of Burgers vector and effective interfacial width of an isolated dislocation, respectively. A comparison between theoretical results calculated by the Matthew and People-Bean models is shown in Fig. 1 at the reference 36, there is a dramatic difference between these two methods in the case of small lattice mismatch (<1.0 %). Huang extended the People-Bean model to discuss the strain relaxation in heterostructure grown on compliant substrate.[38]

It should be mentioned that attainment of a critical thickness predicted by both Matthew-Blakeslee and People-Bean models is not a sufficient condition for strain relaxation, kinetic factors must be considered to describe strain relaxation phenomena in thin films.[39-41] In order for relaxation to occur in practice, it is necessary for threading dislocations exist in the strained layer and temperature permits rapid gliding of these threading dislocations at growth temperature.[39-41] Therefore, thermodynamic, mechanical and kinetic factors will be discussed holistically for thick coherent growth of $BaTiO_3$/$SrRuO_3$ bilayer on $GdScO_3$ ($DyScO_3$) substrates.

4.3. Experimental

Five $BaTiO_3$/$SrRuO_3$ bilayer with different thicknesses were prepared by pulsed-laser deposition: $BaTiO_3$ (200nm) / $SrRuO_3$ (50nm) / (110) $GdScO_3$; $BaTiO_3$ (50nm) / $SrRuO_3$ (200nm) / (110) $DyScO_3$; $BaTiO_3$ (50nm) / $SrRuO_3$ (100nm) / (110) $DyScO_3$; $BaTiO_3$ (100 nm) / $SrRuO_3$ (100nm) / (110) $DyScO_3$; and $BaTiO_3$ (100 nm) / $SrRuO_3$ (50 nm) / (001) $SrTiO_3$. Details of the growth condition have been described at chapter 2.[4] Planar-view and cross-sectional TEM samples were prepared by mechanical grinding, polishing and dimpling, followed by argon ion milling (PIPS^{TM} Model 691, Gatan, Inc.) at 4.0 kV to electron transparency. It is valuable to mention that one of the samples, $BaTiO_3$ (50nm) / $SrRuO_3$ (100nm)/ (110) $DyScO_3$), was annealed at 1000 °C for 10 hours in ambient atmosphere. The aim of this experiment was to confirm that $BaTiO_3$ films are truly constrained by rare-earth scandate substrates. The planar-view samples were ion-milled from the substrate sides. Both a high-resolution electron microscope (JOEL 3011 operated at 300 kV with point-to-point resolution of 0.17 nm) and an analytical electron microscope (JOEL 2010F operated at 200 kV) were used in this work.

4.4. Results

4.4.1 Strained $BaTiO_3$ grown on $GdScO_3$ and $DyScO_3$ substrates

Figure 4.3 shows a typical low-magnification cross-sectional bright-field image of a $BaTiO_3$ (200 nm) / $SrRuO_3$ (50 nm) bilayer grown on (110) $GdScO_3$. It shows that both $BaTiO_3/SrRuO_3$ and $SrRuO_3/GdScO_3$ interfaces are free of dislocations. The dark band at the $BaTiO_3/SrRuO_3$ interface is due to diffraction contrast at the interface. The atomic structures at the $BaTiO_3/SrRuO_3$ and $SrRuO_3/GdScO_3$ interfaces, with electron beam aligned along the [100] zone axis of $BaTiO_3$, are shown in Fig. 4.4(a) and (b), respectively. It can be seen that the both interfaces are fully coherent and atomically sharp.

Similar results were obtained from $BaTiO_3$ (50nm) / $SrRuO_3$ (200 nm), $BaTiO_3$ (50nm) / $SrRuO_3$ (100nm) bilayer grown on (110) $DyScO_3$. Fig. 4.5 shows a cross-sectional TEM image in which both $BaTiO_3/SrRuO_3$ and $SrRuO_3/DyScO_3$ interfaces are free of dislocations. HRTEM images for two interfaces are shown in Fig. 4.6(a) and (b). One can see that both the $BaTiO_3/SrRuO_3$ and the $SrRuO_3/DyScO_3$ interfaces are the coherent and atomically sharp, which are similar to Fig. 4.4(a) and (b). Fig. 4.7 (a) is the bright-field image of $BaTiO_3$ (50nm) / $SrRuO_3$ (100nm) grown on (110) $DyScO_3$

substrate. It is evident again that the $BaTiO_3/SrRuO_3$ and $SrRuO_3/DyScO_3$ interfaces are coherent and dislocation free. As we discussed in the experimental section, the other piece cut from same sample characterized in Fig. 4.7(a) was annealed at 1000 °C for 10 hours. And then similar TEM work was conducted for an annealed piece. The typical bright-field image of the annealed sample is shown in figure 4.7(b). It is obvious that coherent $BaTiO_3/SrRuO_3$ and $SrRuO_3/DyScO_3$ interfaces remain after long annealing time (10 hours) at high temperature (1000 °C). Therefore, we can conclude that these $BaTiO_3/SrRuO_3$ bilayers are coherently grown on $GdScO_3$ and $DyScO_3$ substrates.

4.4.2 Partially relaxed $BaTiO_3$ grown on $DyScO_3$ substrate

However, when the thickness of the $BaTiO_3$ layer increases, the interface between $BaTiO_3$ and $SrRuO_3$ becomes partially relaxed and misfit dislocations form at the $BaTiO_3/SrRuO_3$ interface. Fig. 4.8(a) is a cross-sectional image of a $BaTiO_3$ (100 nm) / $SrRuO_3$ (100 nm) bilayer grown on (110) $DyScO_3$. Dislocation cores at the $BaTiO_3/SrRuO_3$ interface are observed, while the $SrRuO_3/DyScO_3$ interface is free of dislocations. The distribution of dislocations along the $BaTiO_3/SrRuO_3$ interface is inhomogeneous. The average dislocation spacing of about 58 nm is much larger than the theoretical equilibrium dislocation spacing of 25 nm,[23] which indicates that $BaTiO_3$ thin film is partially relaxed. Fig. 4.8(b) is a planar-view TEM image of the same film. The orthogonal dislocation network consists of two perpendicular edge dislocation lines with Burgers vectors $a[100]_{BaTiO_3}$ and $a[010]_{BaTiO_3}$, respectively. X-ray energy dispersion spectroscopy (EDS) analysis, shown in figure 4.9, confirmed that the area studied in Fig.

4.8(b) includes $BaTiO_3$, $SrRuO_3$, and $DyScO_3$. Fig. 4.8(a) confirms that the dislocation networks shown in Fig. 4.8(b) are located at the $BaTiO_3/SrRuO_3$ interface. Figure 4.10 is the HRTEM image of a misfit dislocation generated at interface between $BaTiO_3$ and $SrRuO_3$. The Burgers circuit proves that Burgers vector of the misfit dislocations belongs to $a < 100 >_{\mathrm{BaTiO_3}}$-type.

4.4.3 Partially relaxed $BaTiO_3/SrRuO_3$ bilayer grown on $SrTiO_3$ substrate

When the substrate is changed to $SrTiO_3$, the strain relaxation behavior of $BaTiO_3$ and $SrRuO_3$ bilayer is different from above scenarios. Figure 4.11 (a) and (b) are low-magnification cross-sectional and planar-view micrographs of $BaTiO_3$ (100 nm) / $SrRuO_3$ (50 nm) bilayer grown on (001) $SrTiO_3$ substrate, respectively. As shown in Fig. 4.11 (a), it is obvious that there are misfit dislocations generated at both $BaTiO_3/SrRuO_3$ and $SrRuO_3/SrTiO_3$ interfaces. Statistical measurements prove that the dislocation spacings at $BaTiO_3/SrRuO_3$ and $SrRuO_3/SrTiO_3$ interfaces are 99 nm and 71 nm, respectively. Compared with dislocation spacing at equilibrium condition, one can see that lattice mismatch between $BaTiO_3/SrRuO_3$ bilayer and $SrTiO_3$ substrate has been partially relaxed. The dislocation network is formed in the same sample, as shown in Fig. 4.11 (b). The area imaged in Fig. 4.11 (b) includes $BaTiO_3$, $SrRuO_3$ and $SrTiO_3$, which was confirmed by chemical analysis (not shown here) using x-ray energy dispersion spectroscopy attached to the TEM. Therefore the dislocation network in this micrograph is the overlap of dislocation lines at both $BaTiO_3/SrRuO_3$ and $SrRuO_3/SrTiO_3$ interfaces.

The orthogonal dislocation network is also composed of two perpendicular edge dislocation lines with Burgers vectors of $a[100]$ and $a[010]$, respectively.

4.5. Discussions

4.5.1. Strain relaxation of $BaTiO_3/SrRuO_3$ bilayer grown on $GdScO_3$, $DyScO_3$ and $SrTiO_3$ substrate

The above TEM results verify that the critical thickness of $BaTiO_3$ thin films grown on $GdScO_3$ substrates with coherent $SrRuO_3$ layers is over 200 nm; while critical thickness of $BaTiO_3$ thin films grown on $DyScO_3$ substrates with coherent $SrRuO_3$ layers is between 50 and 100 nm. Additionally the 100 nm $BaTiO_3$ / 50 nm $SrRuO_3$ bilayer grown on a $SrTiO_3$ substrate has been partially relaxed at $BaTiO_3/SrRuO_3$ and $SrRuO_3/SrTiO_3$ interfaces. These results can be understood via holistically considering mechanical effect, kinetic effect, and thermodynamic calculation.

In general, to ensure coherent growth in bilayer systems, the important structural parameters are the thickness of each layer and the lattice mismatch between each layer and substrate.[33-35] Primarily, the mechanical properties are considered to be related to the coherent growth of $BaTiO_3/SrRuO_3$ bilayer on $GdScO_3$ ($DyScO_3$) substrates.[39-42] We used an empirical parameter: the thickness-normalized lattice mismatch, $f = \frac{t_1 f_1 + t_2 f_2}{t_1 + t_2}$ (f and t represent lattice mismatch and thickness, respectively). Although it ignores physical parameters like shear modulus, etc., it is a more accurate measurement of energetic strain instability than considering only lattice mismatch in bilayer system.[42]

The theoretical average in-plane lattice mismatches between the $BaTiO_3$ and $SrRuO_3$ films and the three substrates, $GdScO_3$, $DyScO_3$ and $SrTiO_3$, are calculated in table 4.1. One can see that in the $BaTiO_3/SrRuO_3$ bilayer grown on $GdScO_3$ substrate, $BaTiO_3$ is under compressive stress and $SrRuO_3$ is under tensile stress. In other word, the mismatch strain in this specific bilayer system is compensated by the opposite sign of the strain in each layer. More specifically, the $BaTiO_3/GdScO_3$ lattice mismatch is 0.55 % ($BaTiO_3$ in compression), while the $SrRuO_3/GdScO_3$ lattice mismatch is 1.07 % ($SrRuO_3$ in tension). The thickness normalized lattice mismatch for this system is 0.23 %, which is probably small enough to allow lattice coherency with only limited strain energy build-up. We believe this to be the reason that $BaTiO_3$ (200 nm) / $SrRuO_3$ (50nm) bilayer grown on $GdScO_3$ substrates are still coherent. Stacking thin alternating layers with opposite strain states with respect to substrate has previously been used to growth thick, coherent semiconductor superlattices. As reported by Brenchley *et al.*, coherent $In_{0.59}Ga_{0.41}/In_{0.42}Ga_{0.58}$ superlattices with thickness up to 2.4 μm can be grown on InP substrates.[43] In this instance, the superlattice consists of layered pairs of alternating 0.4 % tensile and 0.8 % compressive strain. Similar results have been reported by Tamargo *et al.*[44] In the case of $BaTiO_3/SrRuO_3$ bilayer grown on $DyScO_3$ substrates, the strain state due to the lattice mismatch is similar to that of the same bilayer grown on $GdScO_3$. Specifically, the compressive strain of $BaTiO_3/DyScO_3$ is 1.20 % and tensile strain of $SrRuO_3/DyScO_3$ is 0.4 %. In the $BaTiO_3$ (50 nm) / $SrRuO_3$ (200 nm) / $DyScO_3$ sample, the thickness normalized lattice mismatch is 0.08 %, again this value is generally small enough to allow for coherent interfaces. However, the thickness normalized lattice mismatch in the $BaTiO_3$ (100 nm) / $SrRuO_3$ (100 nm) / $DyScO_3$ sample is 0.4 %, which is likely too high for fully coherent films, thus causing partial relaxation at the $BaTiO_3$/$SrRuO_3$ interface. When $BaTiO_3$ / $SrRuO_3$ bilayer was grown on a $SrTiO_3$ substrate, the mechanical condition is different from that in the same bilayer grown on $GdScO_3$ ($DyScO_3$) substrate. As shown in table 4.1, one can see that both $BaTiO_3$ and $SrRuO_3$ layers grown on $SrTiO_3$ substrate are under compressive stress. The thickness normalized lattice mismatch in this sample is 1.65 %, which is much larger than that (0.4%) in strain-partially relaxed 100 nm $BaTiO_3$ / 100 nm $SrRuO_3$ grown on $GdScO_3$ substrate. Therefore the strain energy in 100 nm $BaTiO_3$ / 50 nm $SrRuO_3$ bilayer grown on a $SrTiO_3$ substrate has been partially relaxed by the introduction of misfit dislocations at both $BaTiO_3$/$SrRuO_3$ and $SrRuO_3$/$SrTiO_3$ interfaces.

Semi-quantitative calculations based on thermodynamic theory were conducted to corroborate the above discussion. As discussed in the introduction, within the frame work of a thermodynamic equilibrium theory, there are two widely accepted models used to determine the critical thickness: the Matthews-Blakeslee (mechanical equilibrium) model[33-35] and the People-Bean (energy equilibrium) model.[36] The former requires the total energy being a minimum at the critical thickness, while the latter assumes that the elastic energy is equal to the dislocation energy at the critical thickness. Generally, the Matthews-Blakeslee model, which has its physical basis stemming from a force balance, is frequently used to describe strain relaxation in thin film systems. On the other hand, the People-Bean model is more accurate in certain thin film systems which have extremely low initial dislocation densities, low dislocation mobility at growth temperature and small lattice mismatches (<1.0%) between thin film and substrate.[36,39] The critical thickness, h_c, can be expressed in the Matthews-Blakeslee model (Eq. 4.6) and in the People-Bean model (Eq. 4.7). The critical thickness predicted by the People-Bean model is much larger than that predicated by the Matthew-Blakeslee model. Predictions by the People-Bean model are in much closer agreement with our experimental results, which is described at following. To simplify the mechanical problem in bilayer structure, the Young's modulus and Poisson ratio difference in each layer are ignored. The People-Bean model applied to bilayer structure can be expressed as:

$$2G\frac{(1+\nu)}{(1-\nu)}\left(h_1 f_1^2 + h_2 f_2^2\right) = \frac{Gb^2}{4\pi d}\ln\left(\frac{h_1+h_2}{b}\right) \qquad (4.8)$$

Where h and f are the critical thickness and lattice mismatch, with the subscripts 1 and 2 representing the bottom and top layer, respectively. The phase diagrams of coherent/strain-relaxed $BaTiO_3$ and $SrRuO_3$ bilayer grown on $GdScO_3$, $DyScO_3$ and $SrTiO_3$ substrates are shown in Fig. 4.12 (a), (b) and (c), respectively. The lattice mismatches between each layer and substrates, as shown in table 4.1, were used in the calculation. It can be seen from Fig. 4.12 (a) that the critical thickness of $BaTiO_3$ is 225 nm when $SrRuO_3$ layer is 50 nm. Therefore the coherent 200 nm $BaTiO_3$ / 50 nm $SrRuO_3$ /$GdScO_3$ sample [Fig. 4.3] is in agreement with theoretical calculation. As shown in Fig. 4.12 (b), the critical thicknesses of $BaTiO_3$, with the thickness of $SrRuO_3$ being 200 and 100 nm, are 68 and 73 nm, respectively. In other word, it is expected that 50 nm $BaTiO_3$ / 200 nm $SrRuO_3$ and 50 nm $BaTiO_3$ / 100 nm $SrRuO_3$ maintains coherency, while 100 nm $BaTiO_3$ / 100 nm $SrRuO_3$ will be relaxed. The agreement between theory and experimental results [Fig. 4.5, 4.7 and 4.8] is again notable. Finally, we can see from Fig. 4.12 (c) that the critical thickness of $BaTiO_3$ is 18.5 nm when the thickness of $SrRuO_3$ is 50 nm, much thinner than $BaTiO_3$ layer in the 100 nm $BaTiO_3$ / 50 nm $SrRuO_3$ / $SrTiO_3$

sample. Therefore, this calculation supports TEM observation [Fig. 4.11] that both the $BaTiO_3$ and $SrRuO_3$ layers are partially relaxed.

In addition, thick and coherent $BaTiO_3/SrRuO_3$ grown on $GdScO_3$ and $DyScO_3$ substrates could be due to the high crystalline quality (free of threading dislocations, cracks, etc) of substrates and bilayer. As was discussed earlier, the kinetic process for the strain relaxation in thin films is attributed to the generation and propagation of dislocations.[40,41] As shown in Fig. 4.3 and 4.5, the absence of numerous threading dislocations in $BaTiO_3/SrRuO_3$ bilayer systems probably contributes to the coherent growth in the $BaTiO_3$ (200nm) / $SrRuO_3$ (50nm) / $GdScO_3$ and $BaTiO_3$ (50nm) / $SrRuO_3$ (200nm) / $DyScO_3$ samples. More detailed experiments at initial growth stages of these bilayer systems must be conducted to study kinetic effects on strain relaxation.[40,41]

4.5.2. Discussion of strain relaxation in bilayer by pseudomorphic layer model

Huang proposed pseudomorphic layer model to discuss strain relaxation in bilayer structures.[46] It is assumed in this method that before strain relaxation begins, the bilayer will assume a pseudomorphic state to minimize built in strain energy. The in-plane pseudomorphic lattice constant, a_0, is determined via strain energy minimization in bilayer. The strain relaxation in the bilayer is determined by the lattice mismatch between the substrate and pseudomorphic state. In other word, the bilayer structure can be simplified to a monolayer configuration by this method. The formation of a pseudomorphic state in bilayer structures has been observed in some experiments.[46-47] In detail, the strain energy in the pseudomorphic state is expressed as[46]

$$E = \frac{2\mu_1(1+v_1)}{(1-v_1)}\left(\frac{a_0-a_1}{a_0}\right)^2 h_1 + \frac{2\mu_2(1+v_2)}{(1-v_2)}\left(\frac{a_0-a_2}{a_0}\right)^2 h_2 \quad (4.9)$$

where E is the strain energy in bilayer, v is the Poisson ratio, μ is the shear modulus, and a is the in-plane lattice constant, with the subscripts 1 and 2 representing the buffer and top layers. The effective in-plane lattice constant of bilayer can then be determined via energy minimization ($\partial E/\partial a_0 = 0$), which yields a common lattice constant of[46]

$$a_0 = \frac{B_1h_1/a_1 + B_2h_2/a_2}{B_1h_1/a_1^2 + B_2h_2/a_2^2} \quad (4.10)$$

where $B = \frac{2\mu(1+v)}{(1-v)}$. According to equation (4.10), we can see that the in-plane pseudomorphic lattice constant includes the effects of anisotropic elastic property and thickness difference in each layer. The critical thicknesses, predicted by the People-Bean model, in $BaTiO_3/SrRuO_3$ bilayer with different thicknesses grown on $SrTiO_3$, $DyScO_3$ and $GdScO_3$ substrates can be calculated, which are shown in Fig. 4.13 (a), (b) and (c), respectively. In the above calculation, the shear moduli of $BaTiO_3$ and $SrRuO_3$ are 39.4 GPa[48] and 60.1 GPa[49], respectively; and the Poisson ratio of $BaTiO_3$ and $SrRuO_3$ are 0.65[50] and 0.3[51], respectively. For comparison with experimental results, the theoretical critical thicknesses, predicted by pseudomorphic layer model, of five experimental systems are shown in table 4.2. Compared theoretical critical thicknesses and those (total thickness of $BaTiO_3/SrRuO_3$ bilayer) in our experimental samples, samples 1, 2 and 3 should be coherent, while samples 4 and 5 will be relaxed. These results are in agreement with our TEM observations [Fig. 4.3, Fig. 4.5, Fig. 4.7, Fig. 4.8, and Fig. 4.11]. It should be noted, however, that above discussion cannot give any insight into how this strain relaxation is realized.

4.5.3. Effect of strain on spontaneous polarization and Curie temperature in strained $BaTiO_3$ thin films

The strained $BaTiO_3$ thin films studied by TEM show enhanced ferroelectric properties. Figure 4.14 is the ferroelectric hysteresis loops measured for coherent $BaTiO_3$ thin films grown on $DyScO_3$ (red curve) and $GdScO_3$ (blue curve) substrates.[4] We can see that the saturated spontaneous polarization in strain $BaTiO_3$ thin films grown on $DyScO_3$ and $GdScO_3$ are about 80 and 50 μC/cm^2, respectively. As a reference, the spontaneous polarization in bulk $BaTiO_3$ (strain-free) sample is around 25 μC/cm^2.[5] This means that strained $BaTiO_3$ thin films can have double or triple spontaneous electric polarization with respect to strain-free counterpart. This enhancement is dependent on the applied compressive strain. To the best of our knowledge, this is the largest spontaneous polarization reported in compressive-type strained $BaTiO_3$ thin films. The Curie temperature for ferroelectric-to-paraelectric transition was measured by an *in-situ* x-ray diffraction heating experiment.[4] The Curie temperature in strained $BaTiO_3$ grown on $DyScO_3$ and $GdScO_3$ substrates are 400 and 540 °C, respectively.[4] As shown in Fig. 4.2, the agreement between experimental and theoretical results is good when the deviation in free-energy expansion coefficients between $BaTiO_3$ thin films and their bulk counterparts is considered.

4.6. Conclusions

The different strain relaxation in $BaTiO_3/SrRuO_3$ with different thicknesses in each layer was observed by TEM. The different strain relaxation behavior was explained by thermodynamic critical thickness theory and kinetic consideration. Coherent $BaTiO_3/SrRuO_3$ can remain after high temperature annealing (1000 °C for 10 hours). The Burger vector for dislocations generated at $BaTiO_3/SrRuO_3$ interface belongs to <100>-type.

Experimental and theoretical results show that the strain relaxation of $BaTiO_3/SrRuO_3$ bilayer is mainly determined by the lattice mismatch between the substrate and each layer, as well as the thickness of each layer.

The compressive strain triples the spontaneous polarization in the strained $BaTiO_3$ thin film grown on $DyScO_3$ substrate, compared with that in its bulk counterpart.

Curie temperature is increased from 120 °C (strain-free $BaTiO_3$) to 540 °C in strained $BaTiO_3$ thin films grown on $DyScO_3$ substrates, which is in agreement with prediction by thermodynamic calculation.

Table 4.1 The average lattice mismatch between $BaTiO_3$ ($SrRuO_3$) and $GdScO_3$ ($DyScO_3$, $SrTiO_3$).[4] Where the lattice mismatch is defined as $f=(a_{sub}-a_{film})/a_{film}$, a_{sub} and a_{film} are the average in-plane spacing of substrate and thin films, respectively.

Film / Substrate	**Average mismatch (%)**
$SrRuO_3$ / $DyScO_3$	0.41
$BaTiO_3$ / $DyScO_3$	-1.20
$SrRuO_3$ / $GdScO_3$	1.10
$BaTiO_3$ / $GdScO_3$	-0.56
$BaTiO_3$ / $SrTiO_3$	-2.19
$SrRuO_3$ / $SrTiO_3$	-0.51

Table 4.2 The theoretical critical thicknesses predicted by pseudomorphic layer model in five experimental systems.

Samples	**Thickness of $BaTiO_3$ (nm)**	**Thickness of $SrRuO_3$ (nm)**	**Substrate**	**Critical thickness (nm)**
1	200	50	$GdScO_3$	550.0
2	50	200	$DyScO_3$	3100.0
3	50	100	$DyScO_3$	650.0
4	100	100	$DyScO_3$	170.0
5	100	50	$SrTiO_3$	13.0

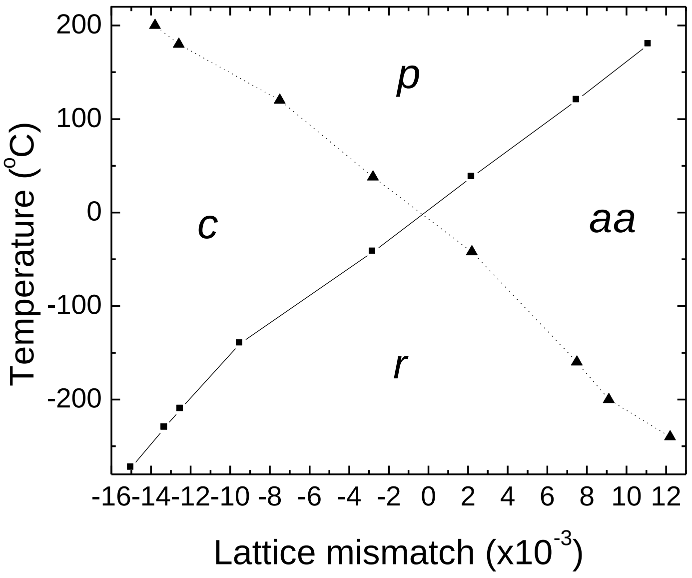

Fig.4.1 The phase diagram of possible domain configuration in $BaTiO_3$ thin films under different temperature and in-plane lattice mismatch (redrawn after Fig. 6 at the reference 16). P, paraelectric phase; c, out-of-plane tetragonal phase; aa, orthorhombic phase with polarization as $p_x=p_y$ and $p_z=0$; r a ferroelectric phase with $p_x=p_y\neq p_z\neq 0$.

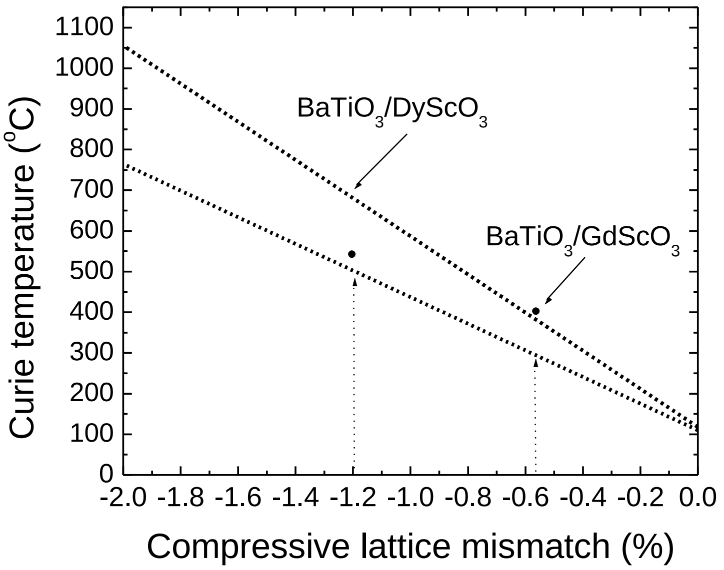

Fig. 4.2 The dependence of Curie temperature in (001) single domain $BaTiO_3$ thin films under different compressive strain. Two discrete spots are experimental results measured by *in-situ* XRD heating experiment.[4]

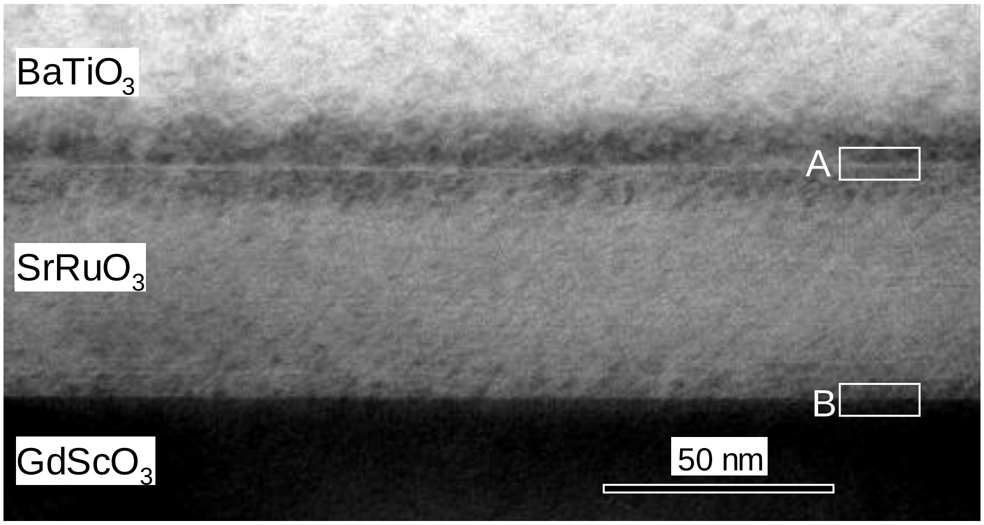

Fig. 4.3 Low-magnification bright-field micrograph for 200 nm $BaTiO_3$ grown on (110) $GdScO_3$ with 50 nm $SrRuO_3$ electrode. Interfacial areas studied by HRTEM are indicated by two white rectangles.

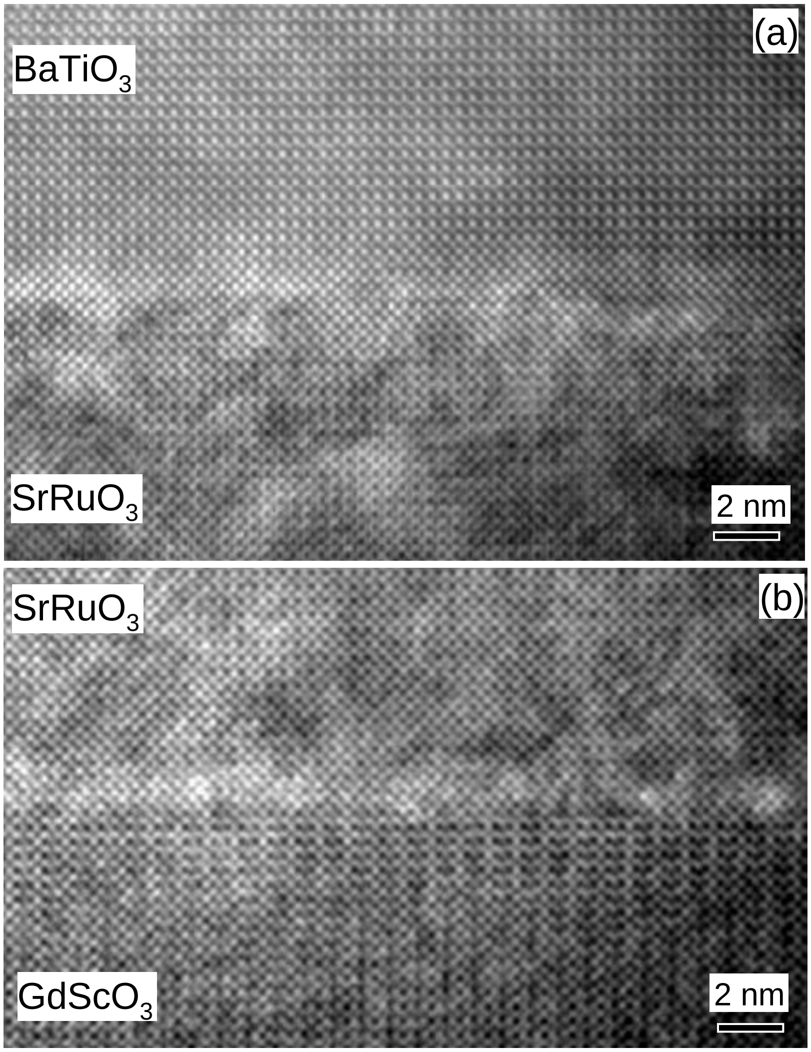

Fig. 4.4 HRTEM images for two interfaces in sample 200 nm $BaTiO_3$/ 50 nm $SrRuO_3$ grown on (110) $GdScO_3$ substrate (a) interface between $BaTiO_3$ and $SrRuO_3$; (b) interface between $SrRuO_3$ and $GdScO_3$.

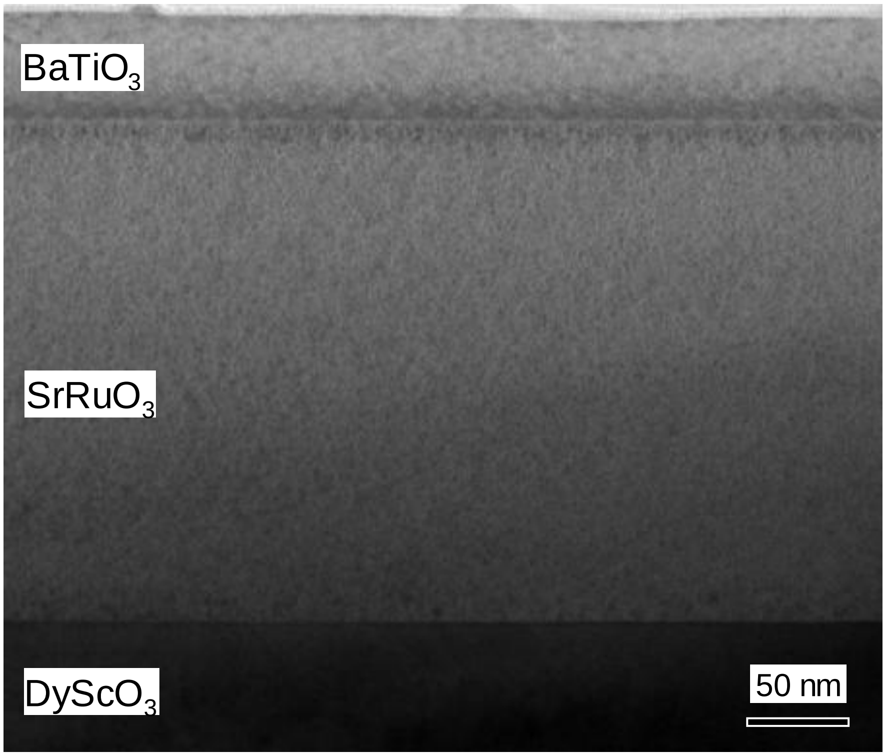

Fig. 4.5 Low-magnification bright-field micrograph for 50 nm $BaTiO_3$ /200 nm $SrRuO_3$ grown on (110) $DyScO_3$ substrate.

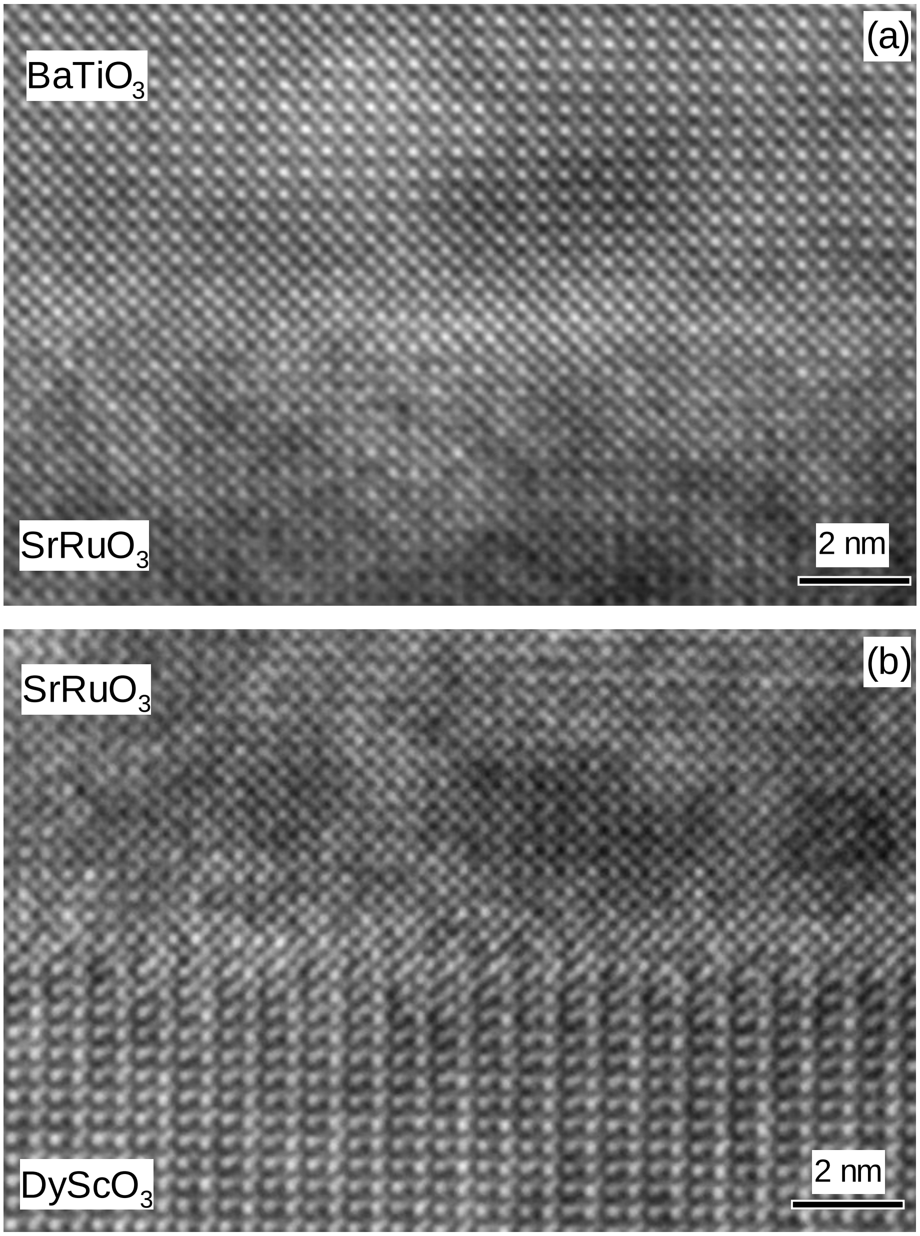

Fig. 4.6 HRTEM images for interfaces (a) between $BaTiO_3$ and $SrRuO_3$ (b) between $SrRuO_3$ and $DyScO_3$ in sample 50 nm $BaTiO_3$ / 200 nm $SrRuO_3$ grown on (110) $DyScO_3$ substrate.

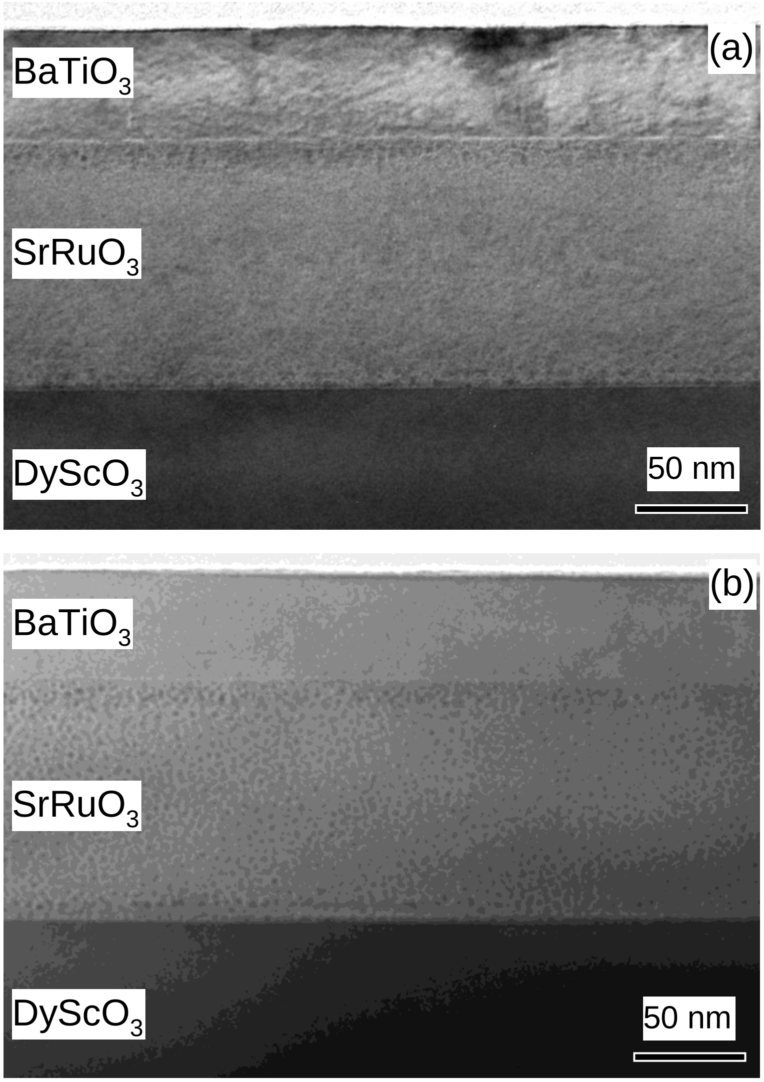

Fig. 4.7 (a) The bright-field image for 50 nm $BaTiO_3$ / 100 nm $SrRuO_3$ grown on (110) $DyScO_3$ substrate. Two sharp interfaces are obvious in this micrograph. (b) The bright field image for sample studied in (a) after annealing (1000 °C for 10 hours). One can see that coherent $BaTiO_3$ and $SrRuO_3$ remain after high-temperature annealing.

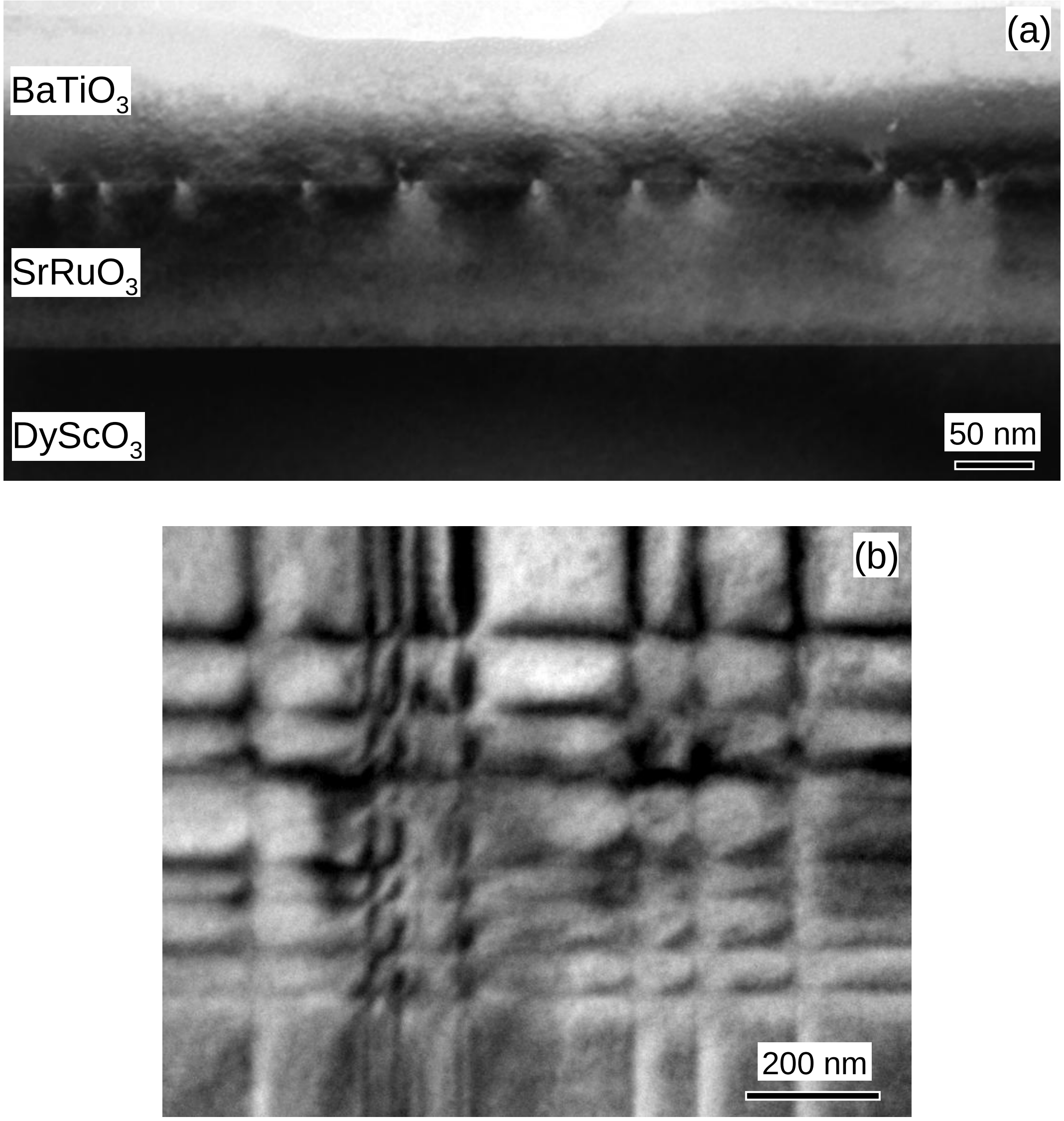

Fig. 4.8 (a) Low-magnification bright-field micrograph of 100 nm BaTiO$_3$ / 100 nm SrRuO$_3$ grown on (110) DyScO$_3$ substrates showing the misfit dislocation cores generated at BaTiO$_3$/SrRuO$_3$ interface. (b) planar-view TEM micrograph of 100 nm BaTiO$_3$ / 100 nm SrRuO$_3$ grown on (110) DyScO$_3$ substrates showing the orthogonal dislocation network.

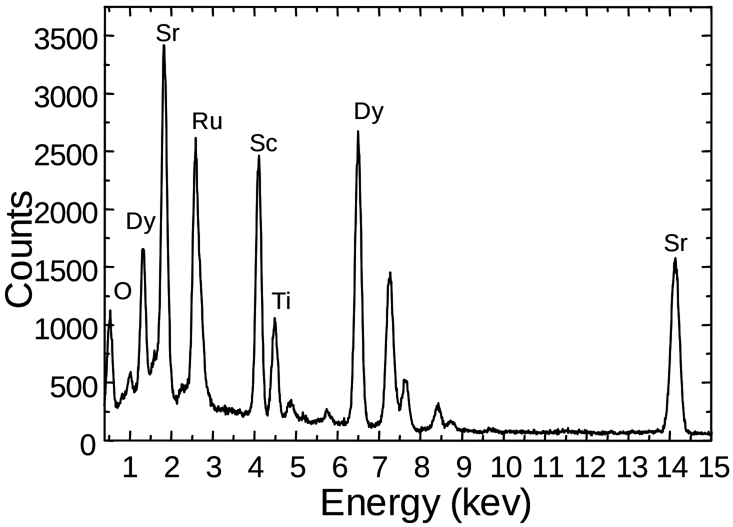

Fig. 4.9 X-ray energy dispersive spectroscopy (EDS) spectrum taken from area shown in Fig. 4.8(b). One can see that there are Dy, Sc, Ba, Ti, and O elements in this area.

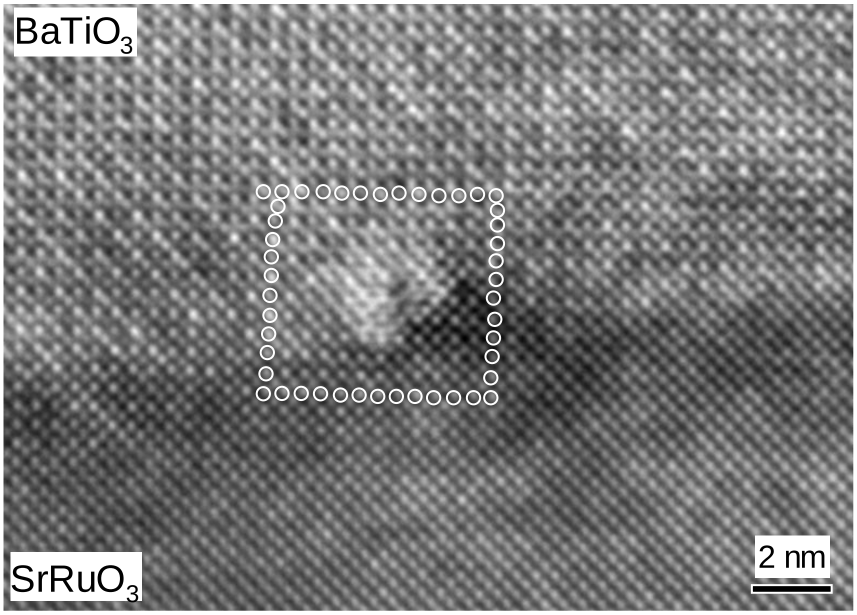

Fig. 4.10 HRTEM image of a misfit dislocation at $BaTiO_3/SrRuO_3$ interface in sample $BaTiO_3$ (100nm) / $SrRuO_3$ (100nm) grown on (110) $DyScO_3$ substrate. Burgers circuit was drawn around the dislocation to determine Burgers vector.

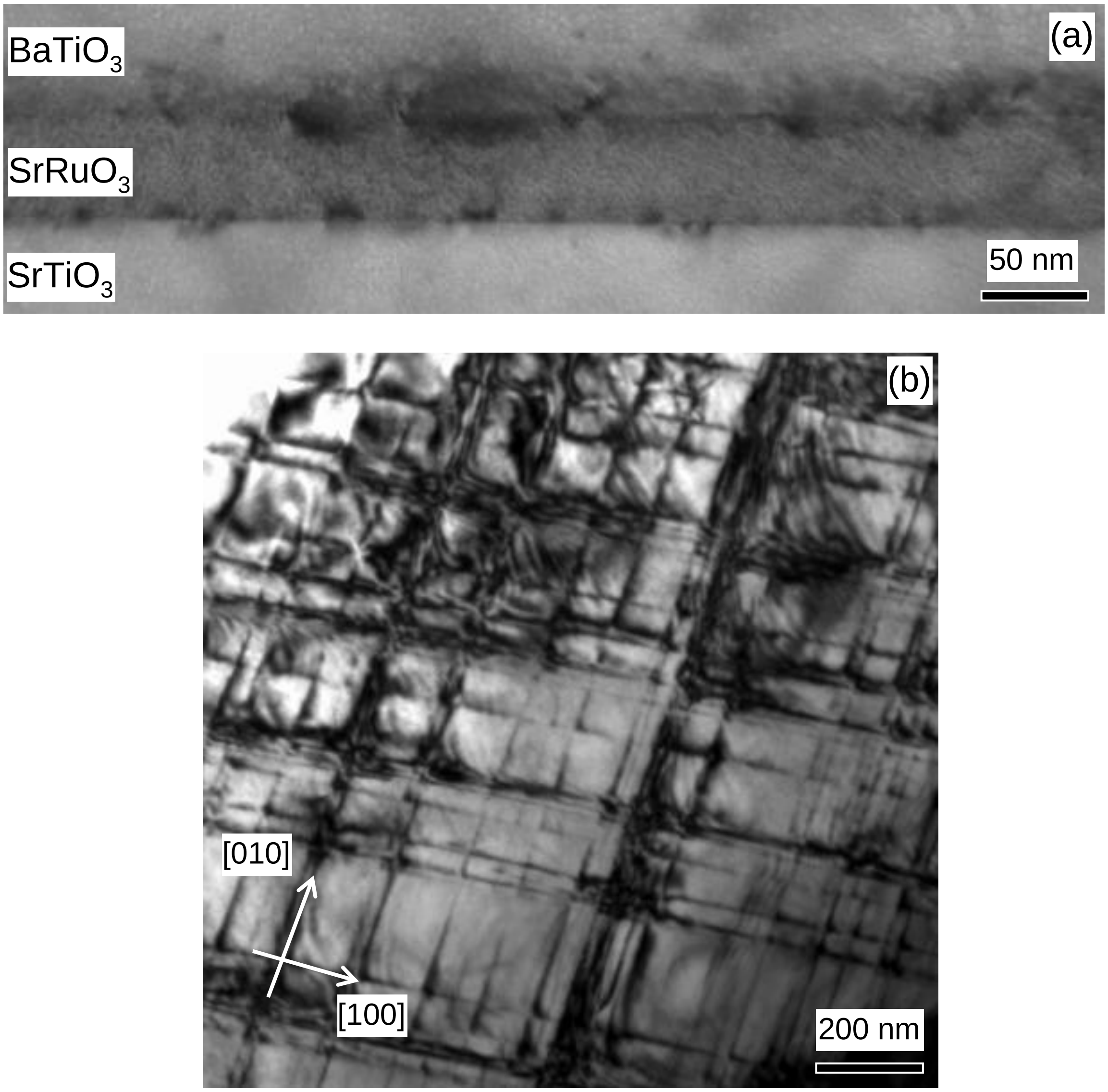

Fig. 4.11 (a) Low-magnification bright-field micrograph of 100 nm $BaTiO_3$ / 50 nm $SrRuO_3$ grown on (001) $SrTiO_3$ substrate showing the misfit dislocation cores generated at $BaTiO_3$/$SrRuO_3$ and $SrRuO_3$/$SrTiO_3$ interfaces. (b) planar-view TEM micrograph of 100 nm $BaTiO_3$ / 50 nm $SrRuO_3$ grown on (001) $SrTiO_3$ substrate showing the orthogonal dislocation network.

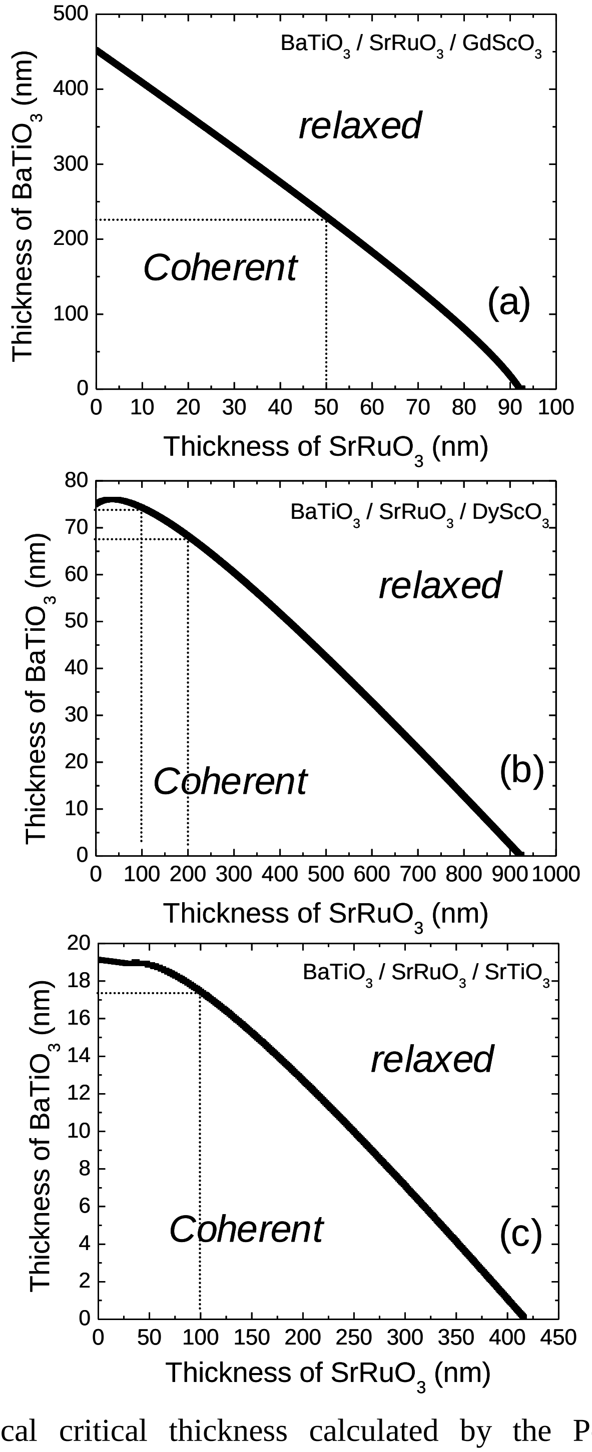

Fig. 4.12 Theoretical critical thickness calculated by the People-Bean model for BaTiO$_3$/SrRuO$_3$ bilayer grown on GdScO$_3$ (a), DyScO$_3$ (b) and SrTiO$_3$ (c) substrates. Dash lines indicate specific systems highlighted in this report for experimental comparison.

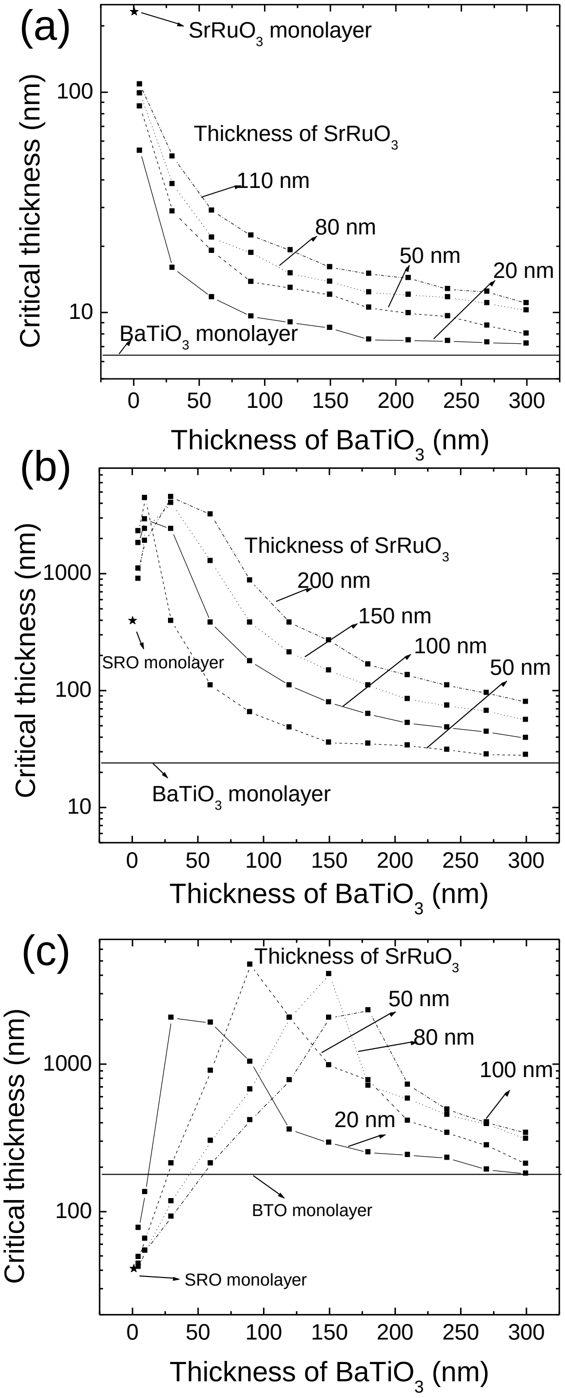

Fig. 4.13 Critical thicknesses, predicted by pseudomorphic model, of $BaTiO_3$/$SrRuO_3$ bilayer grown on $SrTiO_3$ (a), $DyScO_3$ (b) and $GdScO_3$ (c) substrates under different $BaTiO_3$ and $SrRuO_3$ thicknesses. Monolayer $SrRuO_3$ and $BaTiO_3$ cases are labeled by a pentagon and a horizontal line, respectively.

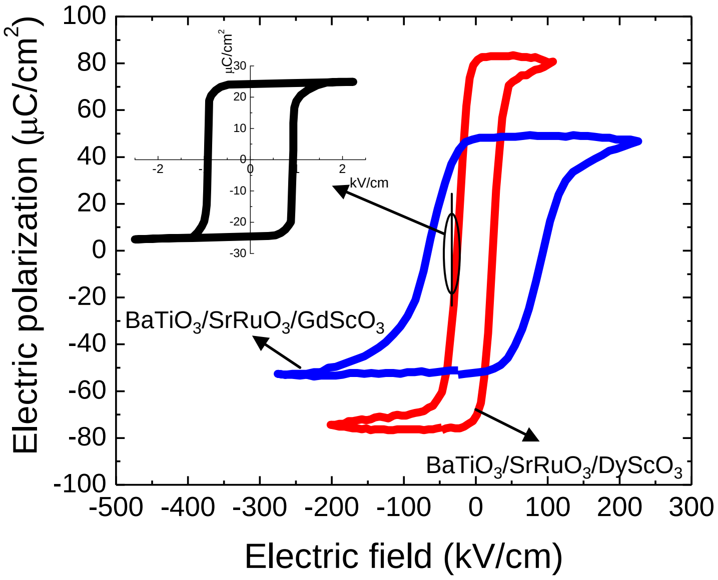

Fig. 4.14 The ferroelectric hysteresis loops of coherent $BaTiO_3$ grown on $DyScO_3$ (red curve) and $GdScO_3$ (blue curve) substrates.[4] The inset is the ferroelectric hysteresis loop of strain-free $BaTiO_3$.

4.7. References:

[1] J. P. Locquet, J. Perret, J. Fompeyrine, E. Machler, J. W. Seo, and G. V. Tendeloo, "Doubling the critical temperature of $La_{1.9}Sr_{0.1}CuO_4$ using epitaxial strain," Nature, **394**, 453 (1998).

[2] J. H. Haeni, P. Irvin, W. Chang, R. Uecker, P. Reiche, Y. L. Li, S. Choudhury, W. Tian, M. E. Hawley, B. Cralgo, A. K. Tagantsev, X. Q. Pan, S. K. Streiffer, L. Q. Chen, S. W. Kirchoefer, J. Levy, and D. G. Schlom, "Room-temperature ferroelectricity in strained $SrTiO_3$," Nature, **430**, 758 (2004).

[3] T. Zhao, H. B. Lu, F. Chen, G. Z. yang, and Z. H. Chen, "Stress-induced enhancement of second-order nonlinear optical susceptibilities of Barium titanate films," J. Appl. Phys., **87**, 7448 (2000).

[4] K. J. Choi, M. biegalski, Y. L. Li, A. Sharan, J. Schubert, R. Uecker, P. Reiche, Y. B. Chen, X. Q. Pan, V. Gopalan, L. Q. Chen, D. G. Schlom, and C. B. Eom, "Enhancement of ferroelectricity in strained $BaTiO_3$ thin films," Science, **306**, 1005 (2004).

[5] W. D. Gallister, Jr., *Materials Science and Engineering An Introduction,* (John Wiley & Sons Inc. 2003, 6th edition) P645.

[6] J. B. Neaton, C. L. Hsueh, and K. M. Rabe, "Enhanced polarization in strained $BaTiO_3$ from first principles," Mat. Res. Soc. Symp. Proc., **718**, D10.26.1 (2002).

[7] J. B. Neaton, and K. M. Rabe, "Theory of polarization enhancement in epitaxial $BaTiO_3$/$SrTiO_3$ superlattices," Appl. Phys. Lett., **82**, 1586 (2003).

[8] S. M. Nakhmanson, K. M. Rabe, and D. Vanderbilt, "Polarization enhancement in two- and three-component ferroelectric superlattices," Appl. Phys. Lett., **87**, 102906 (2005).

[9] J. C. Lee, L. J. Kim, J. Kim, D. Jung, and U. V. Waghmare, "Dielectric properties of $BaTiO_3$/$SrTiO_3$ ferroelectric thin film artificial lattice," J. Appl. Phys., **100**, 051613 (2006).

[10] Y. Emelyanov, N. A. Pertsev, and A. L. Kholkin, "Effect of external stress on ferroelectricity in epitaxial thin films," Phys. Rev. B, **66**, 214108 (2002).

[11] S. B. Desu, and Z. J. Chen, "The phase diagram of epitaxial $BaTiO_3$ films under bi-axial stress," Mat. Res. Soc. Symp. Proc., **433**, 345 (1996).

[12] S. B. Desu, V. P. Dudkevich, P. V. Dudkevich, I. N. Zakharchenko, and G. L. Kushlyan, “Thermodynamics of epitaxial ferroelectric films,” Mat. Res. Soc. Symp. Proc., **401**, 195 (1996).

[13] N. A. Pertsev, A. G. Zembilgotov, and A. K. Tagantsev, “Effect of mechanical boundary condition on phase diagrams of epitaxial ferroelectric thin films,” Phys. Rev. Lett., **80**, 1988 (1998).

[14] J. Wang, and T. Y. Zhang, “Effects of nonequally biaxial misfit strains on the phase diagram and dielectric properties of epitaxial ferroelectric thin films,” Appl. Phys. Lett., **86**, 192905 (2005).

[15] V. G. Koukhar, N. A. Pertsev, and R. Waser, “Thermodynamic theory of epitaxial ferroelectric thin films with dense domain structures,” Phys. Rev. B, **64**, 214103 (2001).

[16] D. G. Schlom, L.-Q. Chen, C. B. Eom, K. M. Rabe, S. K. Streiffer, and J. M. Triscone, “Strain tuning of ferroelectric thin films,” Annu. Rev. Mater. Res., **37**, 589 (2007).

[17] The material parameters for BaTiO3 are: Q_{11}=(0.1 to 0.113) m^4/c^2, Q_{12}=-0.05 to -0.034 m^4/C^2, C=1.37-1.73×10^5 ^oC, $S_{11}+S_{12}$=5.2-6.4×10^{-12} m^2/N, and sita=110-118 ^oC. These data can be found in supplement of reference 4.

[18] G. Schlom, J. H. Haeni, J. Lettieri, C. D. Theis, W. Tian, J. C. Jiang, and X. Q. Pan, “Oxide nano-engineering using MBE,” Mater. Sci. Engi., B, **87**, 282 (2001).

[19] W. Tian, J. C. Jiang, X. Q. Pan, J. H. Haeni, Y. L. Li, L. Q. Chen, D. G. Schlom, J. B. Neaton, K. M. Rabe and Q. X. Jia, “Structural evidence for enhanced polarization in a commensurate short-period $BaTiO_3/SrTiO_3$ superlattice,” Appl. Phys. Lett., **89**, 092905 (2006).

[20] T. Shimuta, O. Nakagawara, T. Makino, S. Aral, H. Tabata, and T. Kawai, “Enhancement of remnant polarization in epitaxial $BaTiO_3/SrTiO_3$ superlattices with “asymmetric” structure,” J. Appl. Phys., **91**, 2290 (2002).

[21] N. Yanase, K. Abe, N. Fukushima, and T. Kawakubo, “Thickness dependence of ferroelectricity in heteroepitaxial $BaTiO_3$ thin film capacitors,” Jpn, J. Appl. Phys., **38**, 5305 (1999).

[22] H. N. Lee, H. M. Christen, M. F. Chlsholm, C. M. rouleau, and D. H. Lowndes, “Strong polarization enhancement in asymmetric three-component ferroelectric superlattices,” Nature, **433**, 395 (2005).

[23] P. Sun, W. Tian, X. Q. Pan, J. H. Hanei, and D. G. Schlom, “Evolution of dislocation arrays in epitaxial $BaTiO_3$ thin films grown on (100) $SrTiO_3$,” Appl. Phys. Lett., **84**, 3298 (2004); P. Sun, X. Q. Pan, J. H. Haeni, and D. G. Schlom, “Structural evolution

of dislocation half-loops in epitaxial $BaTiO_3$ thin films during high-temperature annealing," Appl. Phys. Lett., **85**, 1967 (2004).

[24] T. Suzuki, Y. Nishi and M. Fujimoto, "Analysis of misfit relaxation in heteroepitaxial $BaTiO_3$ thin films," Philosophical Magazine A, **79**, 2461 (1999).

[25] Visinolu, M. Alexe, H. N. Lee, D. N. Zakharov, A. Pignolet, D. Hesse, and U. Gosele, "Initial growth stages of epitaxial $BaTiO_3$ films on vicinal $SrTiO_3$ (001) substrate surface," J. Appl. Phys., **91**, 10157 (2002).

[26] J. Chen, L. A. Wills, B. W. Wessels, D. L. Schulz, and T. J. Marks, "Structure of organometallic chemical vapor deposited $BaTiO_3$ thin films on $LaAlO_3$," J. Electronic Materials, **22**, 701 (1993).

[27] H. Lei, C. L. Jia, M. Siegert, J. Schubert, Ch. Buchal and K. Urban, "Microstructure and orientation relations of $BaTiO_3$/MgO/YSZ multilayer deposited on Si (001) substrates by laser ablation," J. Crystal Growth, **204**, 137 (1999).

[28] H. Lei, G. Van. Tendeloo, M. Siegert, and J. Schubert, "Microstructural investigation of $BaTiO_3$ thin films deposited on (001) MgO," J. Mater. Res., **17**, 1923 (2002).

[29] H. Lei, "The growth of $BaTiO_3$ films on (001) $MgAl_2O_4$ substrates by pulsed laser deposition technique," Thin solid films, **515**, 1701 (2006).

[30] J. Dunstan, "Review Strain and strain relaxation in semiconductors," Journal of Materials Science: Materials in electronics, **8**, 337 (1997).

[31] J. H. van der Merwe, "Crystal interfaces. Part I. semi-infinite crystals," J. Appl. Phys., **34**, 117 (1963).

[32] Frank, J. H. van der Merwe, "One-dimensional dislocations. II. Misfitting monolayers and oriented overgrowth," Pro. Roy. Soc. London, Series A, **198**, 216 (1949).

[33] J. W. Matthews, and A. E. Blakeslee, "Defects in epitaxial multilayers: I. misfit dislocations," J. Cryst. Growth, **27**, 118 (1974).

[34] J. W. Matthews, and A. E. Blakeslee, "Defects in epitaxial multilayers: II. Dislocation pile-ups, threading dislocations, slip lines and cracks," J. Cryst. Growth, **29**, 273 (1975).

[35] J. W. Matthews, and A. E. Blakeslee, "Defects in epitaxial multilayers: III. Preparation of almost perfect multilayers," J. Cryst. Growth, **32**, 265 (1976).

[36] R. People, and J. C. Bean, "Calculation of critical layer thickness versus lattice mismatch for Ge_xSi_{1-x}/Si strained-layer heteorstructures," Appl. Phys. Lett., **47**, 322 (1985); R. People and J. C. Bean, "Erratum: calculation of critical layer thickness

versus lattice mismatch for Ge_xSi_{1-x}/Si strained-layer heterostructures," Appl. Phys. Lett., **49**, 229 (1985).

[37] S. E. Park, Byungsung O, C. R. Lee, "Strain relaxation in $In_xGa_{1-x}N$ epitaxial films grown coherently on GaN," J. Cryst. Growth, **249**, 455 (2003).

[38] F. Y. Huang, "Theory of strain relaxation for epitaxial layers grown on substrate of finite dimension," Phys. Rev. Lett., **85**, 784 (2000).

[39] L. B. Freund, "The driving force for glide of a threading dislocation in a strained epitaxial layer on a substrate," J. Mech. Phys. Solids, **38**, 657 (1990).

[40] L. B. Freund, "Dislocation mechanisms of relaxation in strained epitaxial films," MRS Bulletin, **July**, 52 (1992).

[41] M. D. Thouless, "Modeling the development and relaxation of stresses in films," Annu. Rev. Mater. Sci., **25**, 69 (1995).

[42] R. Hull, J. C. Bean, F. Cerdeira, A. T. Fiory, and J. M. Gibson, "Stability of semiconductor strained-layer superlattices," Appl. Phys. Lett., **48**, 56 (1986).

[43] M. E. Brenchley, M. Hopkinson, and A. Kelly, "Coherency strain as an athermal strengthening mechanism," Phys. Rev. Lett., **78**, 3912 (1997).

[44] M. C. Tamargo, R. Hull, L. H. Greene, J. R. Hayes, and A. Y. Cho, "Growth of a novel InAs-GaAs strained layer superlattice on InP," Appl. Phys. Lett., **46**, 569 (1985).

[45] D. J. Dunstan, S. Young, and R. H. Dixon, J. Appl. Phys., "Geometrical theory of critical thickness and relaxation in strained-layer growth," J. Appl. Phys., **70**, 3038 (1991).

[46] F. Y. Huang, "Effect of strain transfer on critical thickness for epitaxial layers grown on compliant substrate," App. Phys. Lett., **76**, 3046 (2000).

[47] C. Kim, I. K. Robinson, J. Myoung, K. Shim, and K. Kim, "Buffer layer strain transfer in AlN/GaN near critical thickness," J. Appl. Phys., **85**, 4040 (1999).

[48] B. L. Cheng, M. Gabbay, W. Duffy, and J. G. Fantozzi, "Mechanical loss and Young's modulus associated with phase transitions in barium titanate based ceramics," J. Mater. Sci., **31**, 4951 (1996).

[49] S. Venkatesan, B. J. Kooi, J. T. M. De Hosson, A. H. G. Vlooswijk, and B. Noheda, "Substrate influence on the shape of domains in epitaxial $PbTiO_3$ thin films," J. Appl. Phys., **102**, 104105 (2007).

[50] C. Ederer, and N. A. Spaldin, “Effect of epitaxial strain on the spontaneous polarization of thin film ferroelectrics,” Phys. Rev. Lett., **95**, 257601 (2005).

[51] C. B. Eom, *et al*. “Single-crystal epitaxial thin films of the isotropic metallic oxides $Sr_{1-x}Ca_xRuO_3$,” Science, **258**, 1766 (1992).

CHAPTER 5

MICROSTRUCTURE OF $PrScO_3$ THIN FILMS GROWN ON MISCUT SUBSTRATES

5.1. Introduction

In recent years, materials scientists have paid much attention to binary and ternary oxides containing rare-earth elements (e.g., Gd, Dy, Lu). Among them, ternary rare earth scandates, for instance $GdScO_3$, $DyScO_3$ and $LuScO_3$, have attracted considerable attention.[1-15] Research on these materials is stimulated by two potential applications in industry. Primarily, binary and ternary rare-earth oxides are good high dielectric constant (high-k) materials for replacing the SiO_2 insulator layer in conventional complementary metal-oxide semiconductor (CMOS) large-scale integrated circuits. This is because thickness of SiO_2 insulator layer in current CMOS chip is close to ten nanometers given the continued scaling down for electronic devices. Thus, serious leakage current and related energy dissipation in Si chips cause the electric devices to fail.[1] To continue scaling down these devices and avoid leakage current, a new material with a high dielectric constant is required. The underlying principle for high-k dielectric materials is the increasing of the effective thickness of the gate insulator, while retaining equivalent capacitance values in thick SiO_2 gate layer.[1] Binary and ternary rare-earth oxides are studied for this application.[1-11] Secondly, rare-earth scandates ($GdScO_3$, $DyScO_3$) can be used as substrates to grow multifunctional perovskite oxides (such as ferroelectric $BaTiO_3$, cuperate high-temperature superconductors $Sr_xLa_{1-x}CuO_2$) thin films.[12-15] This application is due to the small lattice mismatch and relatively small thermal expansion coefficient difference between the films and substrates.[16] Highly strained $BaTiO_3$ thin films have been grown on $GdScO_3$ and $DyScO_3$ substrates. Strained $BaTiO_3$ thin films show dramatically enhanced ferroelectric properties.[17] According to crystallographic study, these two substrates provide compressive strain to $BaTiO_3$ thin films since in-plane lattice constant of $GdScO_3$/$DyScO_3$ is smaller than that of $BaTiO_3$.[17]

$PrScO_3$ has the similar advantages as high-k candidate with other rare-earth scandates.[10] Besides being a high-k candidate, single crystalline $PrScO_3$ also can be used as a substrate to grow ferroelectric perovskite thin films. It should be mentioned that $PrScO_3$ has larger lattice constant than $BaTiO_3$, opposite to $GdScO_3$ and $DyScO_3$. $PrScO_3$ therefore provides tensile strain to coherent $BaTiO_3$ which is grown above.[18] However, single crystal $PrScO_3$ can not be grown by conventional Czochralski method due to high melting temperature (~2100 °C) and non-congruence at the melting temperature.[19] Strain-relaxed $PrScO_3$ template is an alternative to bulk counterpart. Recently, we grew strain-relaxed, single-domain $PrScO_3$ templates on high-angle miscut $SrTiO_3$ substrates by pulsed laser deposition.[19] The crystalline quality of these templates is close to that in single crystal $SrTiO_3$ substrates.[19] In this chapter, we characterized the crystallographic domains, defects and interface structure in $PrScO_3$ thin films grown on low ($<1^o$) and high-angle ($\geq 1^o$) miscut substrates.

5.2. Background and literature review

In this section, we summarize past studies of ternary rare-earth scandates as high-k materials and growth of multifunctional perovskite oxides with high crystalline quality using rare-earth scandates as substrates. The effect of using vicinal substrates on the microstructure of thin films is reviewed as well.

5.2.1. Study for rare-earth oxides used as high-k dielectric materials

So far, most major efforts have been applied to studying the $GdScO_3$,[1,6,7] $DyScO_3$[1,2,3,4] and $LaScO_3$[8,9,10] thin films grown on Si substrates. For example, Lim *et al*. studied the dielectric functions and optical bandgaps in single crystal $GdScO_3$ and $SmScO_3$ by far ultraviolet spectroscopic ellipsometry and visible-near UV optical transmission measurements.[1] Optical dielectric functions and optical band gap energies for these materials are obtained and discussed by first principles band structure calculations. Zhao *et al*. deposited $GdScO_3$, $DyScO_3$ and $LaScO_3$ on (100) Si by pulsed laser deposition.[2] They found that $DyScO_3$ and $GdScO_3$ preserve their amorphous structures up to 1000 ^{o}C. Dielectric constants were measured as ~22 and low leakage current comparable to HfO_2 of the same equivalent oxide thickness is obtained. Thomas *et al*. deposited the $DyScO_3$ on Si substrate via metal-organic chemical vapor deposition.[3] Films were amorphous with root mean square roughness less than 2 Å and were stable up to 1050 °C. Electric characterization yielded C-V curves with negligible hysteresis (<10 mV), high dielectric constant (~22) and low leakage current. Afanasev *et al*. studied the electron energy band alignment between Si and $LaScO_3$, $GdScO_3$ and $DyScO_3$ by internal photoemission and photoconductivity measurements.[4] The band gap is nearly same in these materials (~5.6-5.7 eV), the conduction and valance band offsets at Si/oxide interface are 2.0±0.1 and 2.5±0.1 eV, respectively. In their later report,[5] they studied the effects of 1 nm SiO_x interlayer on the band alignment between Si and complex rare earth oxides ($LaAlO_3$, $LaScO_3$, and Sc_2O_3). All these materials are found to have the same band offsets even though there is a thin layer SiO_x layer. This suggests that the bulk electron states and properties of the semiconductor and insulator layer play a much more important role in determining the band lineup at the interface than any dipoles related to particular bonding configurations encountered in the transition region between Si and these oxides. Wagner *et al*. synthesized $GdScO_3$ thin films on Si substrate by electron beam evaporation.[6] Rutherford backscattering indicates that the $GdScO_3$ is stoichiometric. Transmission electron microscopy (TEM) study shows that smooth and amorphous films can be stable up 1000 ^oC. Electric characterization revealed that the dielectric constant is 23 and leakage current is as low as 770 $\mu A/cm^2$ for a capacitance equivalent thickness of 1.5 nm. Kim *et al*. grew $GdScO_3$ films by atomic layer deposition.[7] The films were pure and amorphous both as-deposited and after a 5 min annealed at 950 ^oC. TEM study proves that film has smooth interface with respect to Si substrate. Electric measurements give a dielectric constant of 22. $GdScO_3$ films with a 1 nm equivalent oxide thickness have low leakage currents of 2 mA/cm^2 at 1 V gate bias. Edge *et al*. studied the thermal stability of amorphous $LaScO_3$ films by high-resolution TEM (HRTEM), XRD and transmission infrared absorption spectroscopy.[8] XRD studies showed that the films remained amorphous after annealing in N_2 at 700 ^oC. By 800 ^oC, the $LaScO_3$ had started to crystallize and form a ~5 nm thick Sc-deficient interlayer between film and the Si substrate. Heeg *et al*. prepared $LaScO_3$ film by pulsed laser deposition on $SrTiO_3$ and MgO substrates.[9] Electric measurement revealed that dielectric constant is around 20 to 27, leakage current of 0. 85 to 6 μA/cm^2 at 250 kV/cm, a breakdown field of 0.6 to 1.2 mV/cm, and optical bandgaps of the films range from 5.5 to 6 eV. Christen *et al*. studied the crystallization behavior of rare-earth scandates (Y, La, Pr, Nd, Sm, Gd, Tb, Dy, Ho, Er, Tm, Yb, and Lu).[10] The crystallization temperature depends monotonically on the rare-earth element atomic number and Goldschmidt tolerance factor, with crystallization temperature as low as 650 ^oC for $LaScO_3$ and $PrScO_3$. The dielectric constant for crystalline films is 30, which is higher than that in their amorphous counterparts. The band gaps are both 5.5 eV, measured by ellipsometry. It is interesting to mention that meta-stable orthorhombic $LuScO_3$ can be synthesized by epitaxial growth. Heeg *et al*. synthesized meta-stable $LuScO_3$ with an orthorhombic structure by molecular-beam epitaxy and pulsed laser deposition on $NdGaO_3$ and $DyScO_3$ substrates.[11] Rocking-curve XRD measurements show that the full width at half maximum of (001) pole is as narrow as 0.05^o. A critical film thickness of approximately 200 nm is needed for the epitaxial stabilized perovskite polymorph of $LuScO_3$ on $NdGaO_3$ (110) substrates.

In summary, rare-earth scandates are potential candidates to replace SiO_x as insulator layer in novel CMOS structure. This is because rare-earth scandates show the relative high dielectric constant ranging from 22 to 32, large band gap (5.5~5.7 eV) and large band offsets for electrons and holes (2.2-2.5 eV), as well as relatively thermal stability at the high-k films/Si interfaces. It should be emphasized that epitaxial rare-earth scandates have larger dielectric constants than their amorphous counterparts.[10] We focus on epitaxial $PrScO_3$ thin films in this work.

5.2.2. Study for multifunctional perovskite oxides grown on rare-earth scandate substrates

As discussed in reference 20, the lattice constants of the commercially available perovskite substrates, such as $YAlO_3$, $LaSrAlO_4$, $LaAlO_3$, $NdGaO_3$, $LaGaO_3$ and $SrTiO_3$, tend to be smaller than many of the ferroelectric materials of current interest. This is because these commercially available substrates were developed to grow high-temperature superconductor thin films, which have lattice constants ranging from 3.8 to 3.9 Å. Recently, single crystals of $GdScO_3$ (lattice constant ~3.97 Å) and $DyScO_3$ (~3.94 Å) were grown successfully by Czochralski method, which provide novel substrates to grow ferroelectric perovskite oxides.[20] These substrates have close lattice parameters and small thermal expansion differences with $BaTiO_3$ (a typical ferroelectric material) according to *in-situ* XRD measurements.[16] Schubert *et al*. grew highly-crystalline 1 µm $BaTiO_3$ films on (110) $GdScO_3$ substrates by pulsed laser deposition.[12] HRTEM revealed an atomically sharp interface between film and substrate. The optical losses were in $BaTiO_3/GdScO_3$ waveguide less than 2dB/cm at a wavelength of 632.8 nm. Karimoto *et al*. grew high-quality n-type superconducting thin films ($Sr_{1-x}La_xCuO_2$) with a T_c of over 40 K on lattice-matched $DyScO_3$ by molecular beam epitaxy.[13] The optimally doped film seems to be free of strain, thus leading to a low resistivity of 75 μΩ cm at room temperature and 15 μΩ cm just above T_c. Haeni *et al*. reported the ferroelectric properties in strained $SrTiO_3$ films at room temperature grown on $DyScO_3$ substrate by molecular-beam epitaxy.[14] The high E_r at room temperature in these films (nearly 7,000 at 10 GHz) and its sharp dependence on electric field are promising for device applications. In their subsequent work, Biegalski *et al*. studied the ferroelectric properties of a 50 nm strained $SrTiO_3$ film grown on $DyScO_3$ substrates.[15] X-ray rocking curve proves that full width at half maximum in ω-scan for (001)-pole is as narrow as 0.002. These films show a frequency-dependent permittivity maximum near 250 K, which is well fit by Vogel-Fulcher equation. The in-plane remnant polarization was measured to be 10 $\mu C/cm^2$ at 77 K. The high T_{max} is attributed to the biaxial tensile strain state, while the superimposed relaxor behavior is likely due to defects.

In summary, coherent perovskite thin films can be grown on rare-earth scandate substrates. In this work, we grew and characterized the strain-relaxed $PrScO_3$ thin films that can be used as templates to substitute single crystalline $PrScO_3$ substrates.[19,21]

5.2.3. Domain/phase controlling in thin films via miscut substrates

As we discussed in the introduction of Chapter 3, domain structures in thin films can be controlled by means of miscut substrates. There are a series of parallel atomic steps on the surface of miscut substrate, the steps probably provide the initial growth sites for step-flow growth mode, especially in the case of high rate diffusion coefficient along step edges.[22] Gan *et al*. studied the effect of both miscut angle (α) and miscut direction (β) of vicinal substrate on the domain structure and epitaxial growth of $SrRuO_3$ films.[23] $SrRuO_3$ films were grown on miscut $SrTiO_3$ substrates with α up to 4.1° and β up to 37° away from the in-plane [010] direction. Single domain $SrRuO_3$ films can be obtained with large miscut angle (>1.9°) and miscut a direction close to [010] direction. Compared with $SrRuO_3$ films grown on exact $SrTiO_3$ substrates, higher crystalline quality and better in-plane alignment were observed in $SrRuO_3$ films on miscut $SrTiO_3$ substrates. It is probably due to the growth mechanism changes from two-dimensional nucleation to step flow growth. Jiang *et al*. studied the microstructure of $SrRuO_3$ films grown on exact and miscut $SrTiO_3$ substrates by TEM.[24] All six possible domains were observed on $SrRuO_3$ films grown on exact $SrTiO_3$ substrate, while only one type of domain in $SrRuO_3$ films grown on miscut $SrTiO_3$ substrates. The orientation relationship between the film and substrate was determined by electron diffraction. Bu *et al*. employed a vicinal $SrTiO_3$ substrate to stabilize the perovskite phase in $Pb(Mg_{1/3}Nb_{2/3})O_3$-$PbTiO_3$ (PMN-PT) thin film.[25] XRD and TEM studies show that the PMN-PT grown on high angle miscut (>4°) $SrTiO_3$ substrate is nearly pure perovskite phase, while there is high volume fraction of pyrochlore phase in PMN-PT films on exact $SrTiO_3$ substrate. PMN-PT films grown on 8° miscut substrates show a ferroelectric hysteresis loop with a remnant polarization of 20 $\mu C/cm^2$ at room temperature. Dekkers *et al*. studied the correlation between vicinal properties of $SrTiO_3$ substrates and the twinning in YBCO thin films by x-ray reciprocal space mapping.[26] On substrates having an [110] in-plane orientation of step edges, a completely preferred twin pair is observed if miscut angle is increased to 0.6°. While on substrates having their step edges oriented along one of the crystallographic axis, the films exhibit a de-twinning as the vicinal angle increases. With miscut angle increased to 1.1°, single-domain YBCO film can be obtained.

In summary, vicinal substrates can be used to stabilize metastable perovskite phases, manipulate the crystallographic (ferroelectric, ferromagnetic) domains, and suppress the generation of defects in multifunctional perovskite oxide thin films. The anisotropic physical properties can be exploited in oxide thin films with single domain structure grown on vicinal substrates.[23]

5.3. Experimental

The $PrScO_3$ thin films were grown by pulsed laser deposition, as described in Chapter 2. Here, we only emphasize that $PrScO_3$ thin films were synthesized by either direct or two-step growth.[19] In direct growth, 130 nm $PrScO_3$ thin films were grown on substrates at 900 °C. In two-step growth, 30 nm $PrScO_3$ thin films were grown at 900 °C and annealed *ex-situ* at 1200 °C. Then, an additional 100 nm $PrScO_3$ thin film was deposited above annealed buffer layer. Cross-sectional slices for TEM studies were obtained by cutting the $PrScO_3/SrTiO_3$ sample parallel to the miscut direction on substrates in order to study the miscut effects on nucleation and defect structures. TEM samples were then prepared by mechanical grinding, polishing and dimpling, followed by Ar ion milling to electron transparency. TEM studies were carried out on a conventional TEM (Philips CM12 operated at 120 kV) and a high resolution TEM (JEOL 3011 operated at 300 kV) with a point to point resolution of 0.17 nm. Electron diffraction simulation was conducted via commercial software (Crystalkit). And the TEM micrographs were processed by DigitalMicrograph and Photoshop software.

5.4. Results

5.4.1 $PrScO_3$ thin films grown on low-angle (<1°) miscut $SrTiO_3$ substrates

Figure 5.1 are cross-sectional TEM micrographs of the (a) 130 nm $PrSrO_3$ and (b) 100 nm $PrScO_3$ with 30 nm annealed $PrScO_3$ buffer layer, both grown on low-angle (0.4°) miscut $SrTiO_3$ substrates. One can see that the $PrScO_3$ thin films synthesized both by the direct and two-step methods show columnar structures. The average column width, however, is very different between these two samples. The column width of two-step $PrScO_3$ thin films is about 100 nm, much larger than the 30 nm width in $PrScO_3$ thin films grown by direct growth. This indicates that the annealed $PrScO_3$ buffer layer improved the crystalline quality of subsequently grown $PrScO_3$ films dramatically. This assertion is corroborated by the full width at half maximum of the (220) pole, measured by x-ray diffraction.[19] The crystallographic structures of these $PrScO_3$ thin films were characterized by selective area electron diffraction (SAED), shown in figure 5.2(b). To index this pattern, diffraction experiments were simulated using the CrystalKit software. Figure 5.2(c) is the composite patterns including [001] and $[\bar{1}10]$ zone axis electron diffraction patterns of orthorhombic $PrScO_3$, respectively. Two $[\bar{1}10]$ electron diffraction patterns are rotated 90° against each other in the paper plane. It is apparent that the resulting composite pattern matches well with the experimental diffraction pattern shown in the figure 5.2(b). This proves that there are three types of domains in $PrScO_3$ thin films. This analysis shows that all three type domains exist in the $PrScO_3$ thin films grown on 0.2° miscut (001) $SrTiO_3$. The orientation relationship between three different domains and $SrTiO_3$ substrate can be expressed as:

$$[\bar{1}10](110)\ PrScO_3\ //\ [100](001)\ SrTiO_3\ (\alpha\text{-type})$$

$$[001](110)\ \mathrm{PrScO_3} \,//\, [100](001)\ \mathrm{SrTiO_3}\ (\beta\text{-type}) \qquad (5.1)$$

$$[\bar{1}10](001)\ \mathrm{PrScO_3} \,//\, [100](001)\ \mathrm{SrTiO_3}\ (\gamma\text{-type})$$

A similar multi-domain structure reported in isostructual $SrRuO_3$ thin films is due to a structural transition upon cooling.[27] However, there exists no analogous structural transition in $PrScO_3$ within the temperature range of room temperature to 1100°C.[19] Therefore, we believe that the multi-domain structure is formed at the deposition temperature.

To examine the atomic structure of the $PrScO_3$ domains, high resolution TEM (HRTEM) was conducted. Figure 5.2(d) and (e) show cross-sectional HRTEM images of two domain boundaries from areas indicated by black rectangles in figure 5.2(a). As shown in these two images, the domain in the middle is β-type while the domain on the left is γ-type and on the right α-type. This is also confirmed by the fast Fourier transformation (FFT) analysis (not shown here) taken from corresponding areas. In addition, it can be seen that the domain boundaries are atomically sharp.

In addition to the crystallographic domains described above, there are misfit dislocations distributed periodically along the film/substrate interface. Figure 5.3(a) is a high-magnification TEM micrograph showing several dislocation cores at the $PrScO_3/SrTiO_3$ interface. The atomic structure of a misfit dislocation core, incident electron beam aligned along the [100] $SrTiO_3$ direction, is shown in figure 5.3(b). The Burgers vector was determined to be a <010> by drawing a Burgers circuit around the dislocation core. The spacing between neighbor dislocations is about 17.3 nm, while the theoretical equilibrium dislocations spacing can be calculated as 14 nm.[28] This means that misfit dislocations relax the 82 % misfit strain between films and substrate. Considering the multi-domain structure observed in $PrScO_3$ films grown on low angle miscut $SrTiO_3$ substrates, the strain arising from the lattice mismatch between the thin film and substrate is relaxed by the formation of misfit dislocations and the multi-domain structures.

5.4.2 $PrScO_3$ thin films grown on high-angle (≥1°) miscut $SrTiO_3$ substrates

For comparison with $PrScO_3$ thin films grown on low-angle (<1°) miscut $SrTiO_3$ substrates, we also studied the microstructure of $PrScO_3$ thin films grown on 4° miscut $SrTiO_3$ substrates by both direct and two-step growth, which are shown in figures 5.4(a) and (b), respectively. One can see again that $PrScO_3$ thin films exhibit the columnar structure in both samples. And the annealed $PrScO_3$ buffer layer improves the crystalline quality of the subsequently grown $PrScO_3$ thin films. The column width in $PrScO_3$ grown by two-step growth is around 130 nm, which is larger than that in $PrScO_3$ grown by direct growth (~30nm). The SAED was conducted to study the domain structure of $PrScO_3$ thin films grown on 4° miscut $SrTiO_3$ substrates, which is shown in the figure 5.4(c). Compared with computer electron diffraction pattern simulations described previously, Fig. 5.4(c) shows that the $PrScO_3$ thin films grown on 4° miscut $SrTiO_3$ comprise only one orientation relationship with the substrate: $PrScO_3$ (110) [001] // $SrTiO_3$ (001) [100], the β-type domain in accordance with the above classification. This indicates that the $PrScO_3$ thin films grown on 4° miscut $SrTiO_3$ consist of a single domain. Though there is only one type of domain, many defect fringes in $PrScO_3$ can be seen in figure 5.4(a). These fringes are identified as either antiphase boundaries bounded by partial dislocations or small angle (<1^o) rotation domain boundaries. An HRTEM micrograph of a typical antiphase boundary for this film is shown in figure 5.4(d). The atomic displacement between the left and right domains is $\frac{1}{2}[001]_P$ in the pseudocubic setting. And figure 5.5 is a HRTEM image for an antiphase boundary bounded by a partial dislocation generated at $PrScO_3/SrTiO_3$ interface. It can be seen that this fringe is {011}-type antiphase boundary. A similar defect has been reported on thin films with perovskite structures.[29] An associated partial dislocation with a Burgers vector 1/2<011>-$SrTiO_3$ is seen at the substrate/film interface, determined by the Burgers circuit shown in Fig. 5.5.

Identical to $PrScO_3$ thin films grown on low angle (<1°) miscut $SrTiO_3$, periodic misfit dislocations were generated in the $PrScO_3$ thin films grown on high angle (≥1°) miscut $SrTiO_3$ substrates. Figure 5.6 is a high magnification TEM micrograph of several typical interfacial misfit dislocations of Burgers vector <100>. The average dislocation spacing is about 17.0 nm, again close to the equilibrium spacing of 14.5 nm. Therefore, the lattice mismatch between the film and substrate is also mainly relaxed by the formation of misfit dislocations at the interface. The inset is the HRTEM image for a dislocation core at $PrScO_3/SrTiO_3$ interface. The Burgers vector also can be determined as <010>-type.

Figure 5.7 is the bright field image for 100 nm $PrScO_3$ thin film grown on 1° miscut $SrTiO_3$ substrate by two-step growth. It can be seen that film shows the columnar structure too. SAED pattern (not shown here) proves that there is only one type of domain. Careful study for the fringes shown in Fig. 5.7 proves that the majority defects in this sample are small angle rotation domain boundaries. These studies prove that the miscut angle in vicinal $SrTiO_3$ substrates can be as low as 1° to induce growth of single domain $PrScO_3$ thin films.

To quantify the crystalline quality in $PrScO_3$ thin films grown on miscut $SrTiO_3$ substrates with different miscut angles, high-resolution x-ray diffraction measurement was conducted.[19] Figure 5.8 is the comparison of full-width at half maximum (FWHM) on (220) pole in $PrScO_3$ grown on 0.2, 1.0, 2.0 and 4.0^o miscut $SrTiO_3$ substrates.[19] It can be seen that FWHM in $PrScO_3$ on 0.2 miscut $SrTiO_3$ substrate is 0.17, which is the highest among these films; while FWHM increases from 0.045 to 0.09 when the miscut angle in $SrTiO_3$ substrates changes from 1 to 4°. A qualitative discussion of the decreasing of FWHM in $PrScO_3$ thin films grown on $SrTiO_3$ substrates miscut at various angles is given.

5.4.3 $PrScO_3$ thin film grown on high-angle (2°) miscut LSAT substrates

It is of interest to study whether other miscut perovskite substrates may also be used to control the crystallographic domain structure of $PrScO_3$ thin films. For this work, LSAT substrates were utilized for comparison. Figure 5.9(a) is a dark-field micrograph for $PrScO_3$ film on LSAT substrate by two-step growth. (100) weak reflection was used to take this picture. One can see that there is only one type of crystallographic domain, which is similar to scenario happened in $PrScO_3$ films grown on high angle ($\geq 1^o$) miscut $SrTiO_3$ substrates. This result proves that controlling crystallographic domains can be realized by means of miscut perovskite substrates. Figure 5.8(b) and (c) are SAED patterns taken from substrate and from the substrate and thin film, respectively. Figure 5.9(b) was taken from substrate, which can be indexed as [100] zone axis of LSAT. And figure 5.9(c) is the SAED pattern including $PrScO_3$ film and LSAT substrate. The orientation relationship between $PrScO_3$ film and LSAT substrate can be described as:

$$[001]\ (110)\ PrScO_3\ //\ [100]\ (001)\ LSAT \quad (5.2)$$

In accordance with above setting, the crystallographic domain in $PrScO_3$ belongs to β-type, too. Using reflection spots from LSAT as internal calibration, the lattice parameters in $PrScO_3$ can be calculated as a=0.581 nm and b=0.550 nm. Comparing with lattice parameters in $PrScO_3$ bulk material,[19] we can conclude that the $PrScO_3$ films are nearly fully relaxed. In the $PrScO_3$/LSAT interface area, periodic misfit dislocations were also observed. Figure 5.8(d) is a high-magnification micrograph for misfit dislocations. The spacing between two neighboring misfit dislocations is measured as 10.4 nm, which is close to the one (10.2 nm) in equilibrium condition. This result is in agreement with SAED result.

5.5. Discussions

5.5.1 The improvement of crystal quality in $PrScO_3$ thin films grown by two-step growth

The improvement of crystalline quality in $PrScO_3$ synthesized by the two-step growth method can be understood by considering the following scenario. In two-step growth, the first 30 nm $PrScO_3$ thin film was grown at 900 °C and annealed at 1200 °C. It is expected that the lattice mismatch between 30 nm $PrScO_3$ and substrates is relaxed via the formation of misfit dislocations, in agreement with our observations and pervious studies.[28,30] The substrate now has effectively changed from the original $SrTiO_3$ or LSAT to pseudo-substrates of $PrScO_3$ exhibiting the bulk lattice constant. Now, on subsequent

$PrScO_3$ growth, layer-by-layer or step-flow growth can now occur due to the virtual lack of any lattice mismatch between the film and the pseudo-substrate. In the case of high-angle miscut substrates, the periodic atomic steps of the substrate also appear on the surface of pseudo-substrates, observable by atomic force microscopy.[23] It is reasonable to assume that growth on these stepped pseudo-substrates is dominated by step-flow growth, in theory yielding very high crystalline quality films. However, it is possible that neighboring terraces are rotated against each other by 90° in low angle (<1°) miscut substrates or by small angles in high angle (≥1°) miscut substrates. These terraces quite probably affect the domain structures in the subsequent $PrScO_3$ film. We expect it is for this reason that we observed the columnar structures in our $PrScO_3$ films with small-angle rotation domain boundaries, antiphase boundaries and dislocations at the interface between neighboring domains. On the contrary, direct growth $PrScO_3$ thin films should follow three-dimensional growth because of its large lattice mismatch with $SrTiO_3$ (~3.1%) and with LSAT (~3.8%).[19] It is for this reason that there are more extended defects, and hence smaller grain sizes, in direct growth versus two-step growth. As to preferential β-type domain growth on high-angle (>1°) miscut substrates, this effect is possibly due to the relatively smaller strain energy along the pseudo-infinite direction of atomic steps in the β-type domain than α- or γ-type domains, as discussed in part 5.5.3.

5.5.2 The possible crystallographic domains in $PrScO_3$ thin films grown on perovskite cubic $SrTiO_3$ substrates

$SrTiO_3$ has a cubic perovskite structure with the space group of *P*m3m (no. 221) and lattice constant of 0.3905 nm. $PrScO_3$ has a $GdFeO_3$-type orthorhombic structure.

The space group has been determined to be *P*bnm (No. 62) with lattice constants a=0.5609 nm, b=0.5777 nm and c=0.8031 nm.[24] And crystal structure of $PrScO_3$ can be viewed as pseudo-tetragonal structure. In this setting, lattice constant of a_{PT} (subscription PT represents to pseudo-tetragonal structure) is equal to b_{PT} but different from c_{PT} ($a_{PT}=b_{PT}=d_{110}\neq c_{PT}= c/2$). Therefore, $PrScO_3$ thin films can be grown with either the (001) or (110) plane parallel to the $SrTiO_3$ (001) plane (Miller indices of $PrScO_3$ in this chapter are based on orthorhombic unit cell). Theoretically, $PrScO_3$ thin films grown epitaxially on terraces of (001) miscut $SrTiO_3$ substrates may have domains in one of six possible orientations relative to the substrate as shown in figure 5.10:[24]

$$\begin{aligned}
&\alpha\text{-domains: } PrScO_3\ (110)[\bar{1}10] \,//\, SrTiO_3\ (001)[100];\\
&\beta\text{-domains: } PrScO_3\ (110)\ [001] \,//\, SrTiO_3\ (001)\ [100]; \qquad (5.3)\\
&\gamma\text{-domains: } PrScO_3\ (001)\ [\bar{1}10] \,//\, SrTiO_3\ (001)\ [100];
\end{aligned}$$

and their variants by a 180° in-plane rotation, which can not be distinguished from the above three domains in conventional TEM images.[24] Figure 5.10 shows a schematic diagram of the three possible domain configurations in $PrScO_3/SrTiO_3$ system.

5.5.3 The preferential growth of β-type domain in $PrScO_3$ thin films on high-angle (≥1°) miscut $SrTiO_3$ substrates

To understand the effect of high angle (≥1°) miscut $SrTiO_3$ substrate on the domain structure of the $PrScO_3$ thin films, we consider the lattice misfit with different epitaxial orientations between $PrScO_3$ and $SrTiO_3$. As a result of a vicinal cutting, there are parallel terraces on the surface of 4° miscut $SrTiO_3$ substrate (Fig. 5.10). Each terrace has infinite size perpendicular to miscut direction ([100] $SrTiO_3$ direction in Fig. 5.10), but finite size parallel to miscut direction ([010] $SrTiO_3$ direction in Fig. 5.10) depending on miscut angle. Therefore, the strain state along infinite direction of terrace could be a crucial factor in the orientation of the domain during the nucleation and growth of $PrScO_3$. Comparing the strain states in the three different domain configurations (Fig. 5.10), it can be seen that the lattice mismatch in the β-type domain (2.8 %) is lower than that in α- and γ-type domains (3.0 %) along the infinite direction of terraces. This possibly leads to the preferred β-type domain in the $PrScO_3$ thin films.

5.5.4. The effect of microstructure of $PrScO_3$ films on the crystalline quality

According to aforementioned full width at half maximum (FWHM) measurement [shown in Fig. 5.8], one can see that the FWHM of (220) pole has maximum value (0.17°) in $PrScO_3$ on 0.2^o miscut $SrTiO_3$ substrate, while it is 0.065° and 0.089° in $PrScO_3$ grown on 1° and 4° miscut substrates, respectively. TEM result indicates that there are 6 different variances in $PrScO_3$ thin films grown on low-angle (<1°) miscut $SrTiO_3$ substrates. The reflection from (220) (Bragg angle is 22.291°) and (004) (Bragg angle is 22.55°) pole can not be distinguished by x-ray diffraction. The FWHM of (220) pole therefore in $PrScO_3$ grown on 0.2° miscut $SrTiO_3$ substrate has highest value. However, there is only one type of variance when $PrScO_3$ films grown on high-angle ($\geq 1^o$) miscut $SrTiO_3$ substrates, which leads to small FWHM values in $PrScO_3$ films grown on high angle miscut $SrTiO_3$ substrates. In detail, FWHM values in $PrScO_3$ films grown on 1° and 2° miscut $SrTiO_3$ substrates are 0.065° and 0.066°, respectively. They are smaller than that (0.088°) in $PrScO_3$ grown on 4° miscut $SrTiO_3$ substrate. Our TEM results show that there are small-angle rotation domain boundaries, stacking faults bounded by partial dislocations in $PrScO_3$ film grown on 4° miscut $SrTiO_3$ substrate. It probably results in the larger FWHM value in $PrScO_3$ grown on 4° miscut $SrTiO_3$ substrates with respect to $PrScO_3$ grown on 1° miscut $SrTiO_3$ substrates. In later case, the majority defects in $PrScO_3$ film grown on 1° miscut $SrTiO_3$ substrate are small-angle rotation domain boundaries. Obviously, what the quantitative correlation between small angle and antiphase boundary and FWHM value needs further study.

5.6. Conclusions

Strain-relaxed, single-domain $PrScO_3$ templates can be grown on high-angle (>1°) miscut substrates ($SrTiO_3$ and LSAT) by pulsed laser deposition.

$PrScO_3$ template grown on low angle (<1°) miscut $SrTiO_3$ substrate is composed of six-type crystallographic domains. The orientation relationship between $PrScO_3$ template and $SrTiO_3$ substrate has been determined.

Ex-situ Annealed 30 nm $PrScO_3$ buffer layer improves crystalline quality of successively-grown thick $PrScO_3$ layer dramatically. However, the annealed template cannot be used to control crystallographic domain structures in $PrScO_3$ thin film.

When $PrScO_3$ template was grown on high angle (≥1°) $SrTiO_3$ substrate, there is only one type of variance in $PrScO_3$ film. The orientation relationship between film and substrate is: [001] (110) $PrScO_3$ // [100] (001) $SrTiO_3$. $PrScO_3$ films with high crystalline quality can be grown on 1° miscut $SrTiO_3$ substrate (FWHM of (220) pole is about 0.07). Lattice mismatch between films and substrates is mainly relaxed by the formation of misfit dislocations at $PrScO_3$/$SrTiO_3$ interface. The Burgers vector was determined as <100>a.

Single domain $PrScO_3$ films can be grown on high-angle (2°) miscut LSAT substrates, too. The orientation relationship between films and substrates is: [001] (110) $PrScO_3$ // [100] (001) LSAT. $PrScO_3$ thin film is also relaxed by misfit dislocations generated at $PrScO_3$/LSAT interface. The Burgers vector belongs to <100>a type as well.

The growth of single domain $PrScO_3$ on high angle ($\geq$1°) miscut $SrTiO_3$ substrate is probably caused by strain-energy minimization in terraces on the $SrTiO_3$ surface.

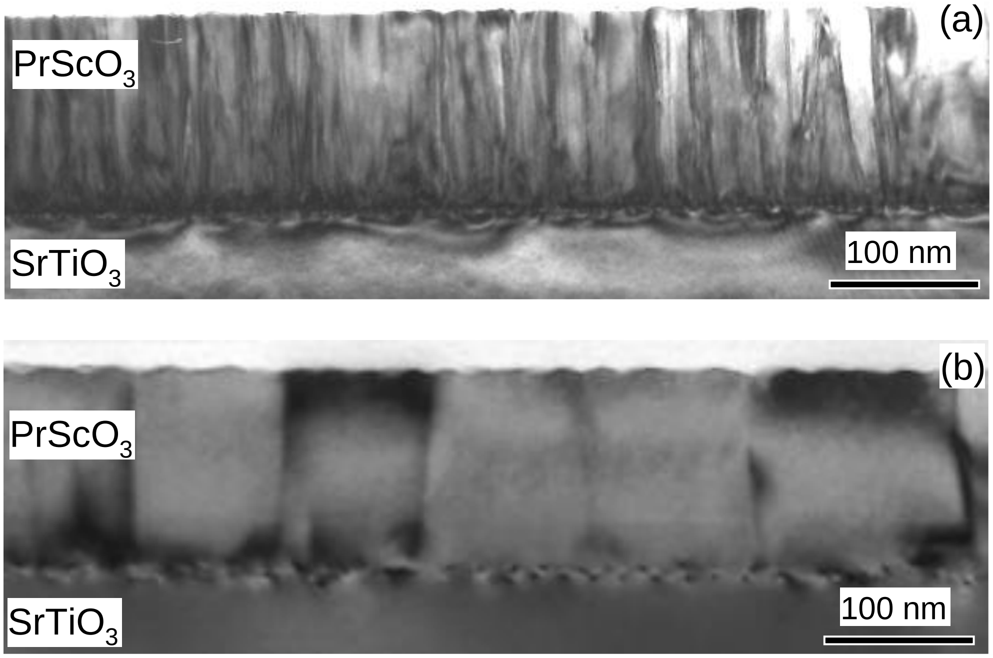

Fig. 5.1 (a) The bright field image of 130 nm PrScO$_3$ thin films grown on 0.2° miscut SrTiO$_3$ substrate by direct-growth. (b) The bright field image for 100 nm PrScO$_3$ thin films grown on 0.4° miscut SrTiO$_3$ substrate by two-step growth.

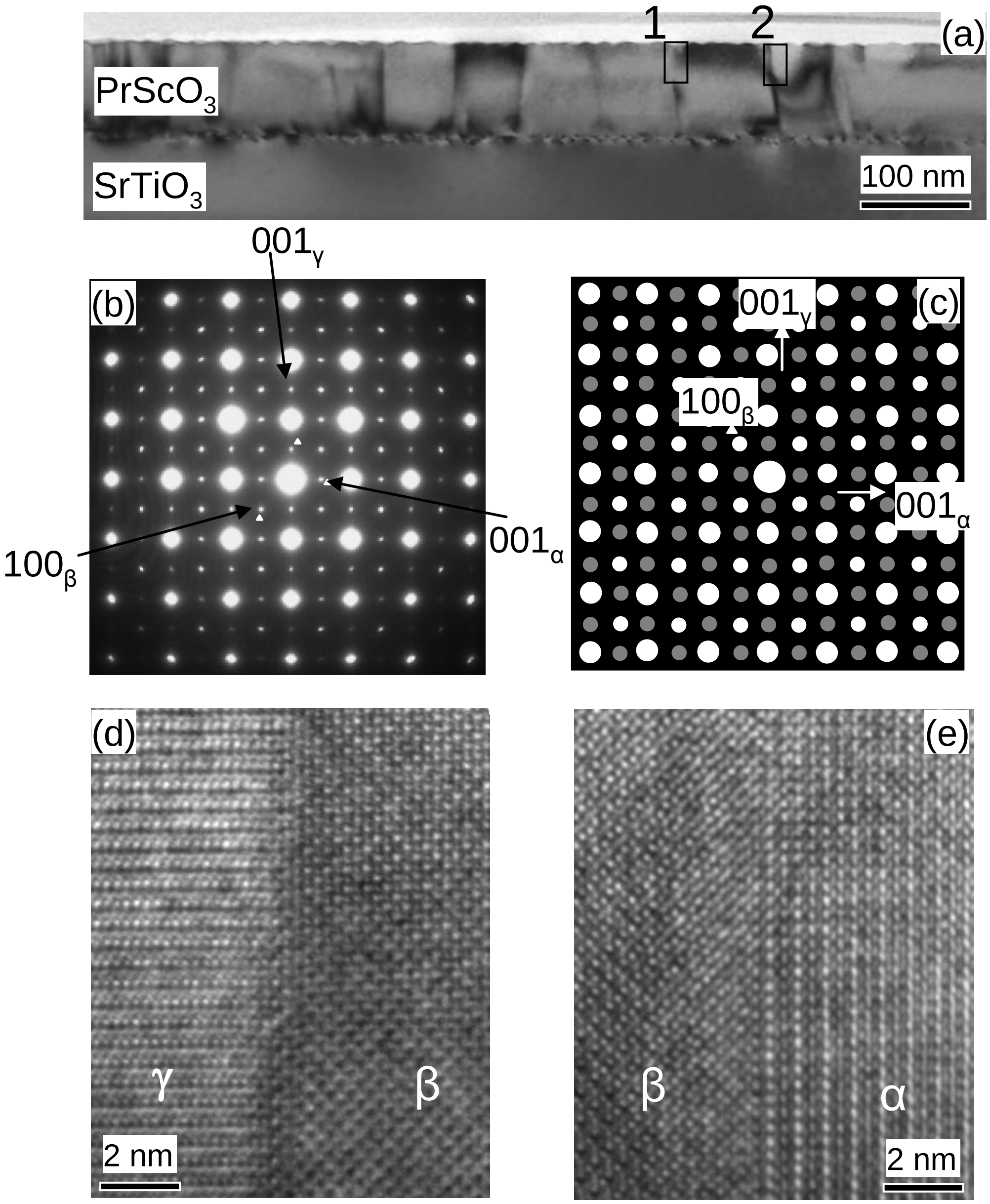

Fig. 5.2 (a) The bright-field image for 100 nm $PrScO_3$ grown on 0.4° miscut $SrTiO_3$ substrate synthesized by two-step growth. (b) The SAED pattern taken from $PrScO_3$ thin film. The weak spots coming from three different crystallographic domains were labeled. (c) The simulated SAED pattern is composed of two [$\bar{1}10$] and [001] zone axis of $PrScO_3$. Two [$\bar{1}10$] zone axis are rotated 90° against each other in paper plane. (d) The HRTEM image for grain boundary indicated by 1 in Fig. 5.2(a). (e) The HRTEM image for grain boundary indicated by 2 in Fig. 5.2 (a).

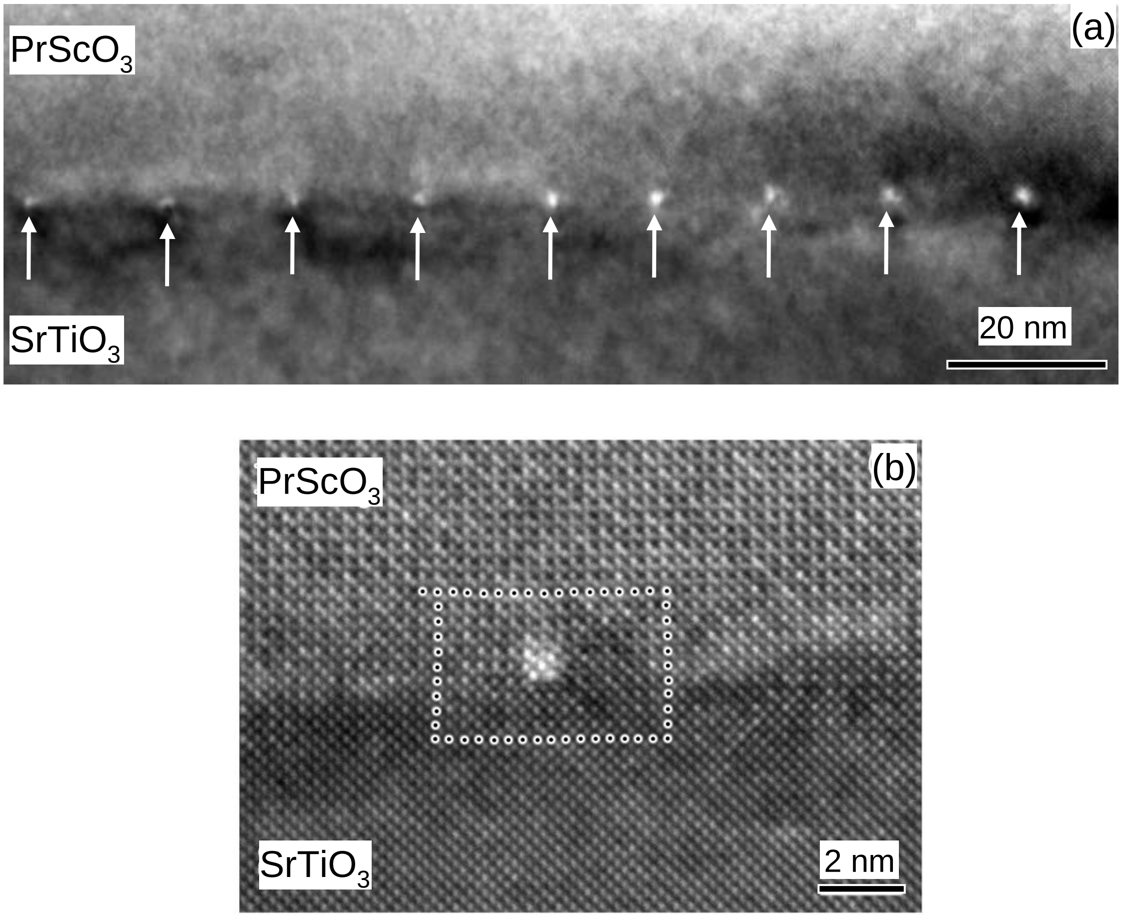

Fig. 5.3 (a) The high-magnification image for periodic misfit dislocations generate at the $PrScO_3/SrTiO_3$ interface in sample 130 nm $PrScO_3$ grown on 0.4° miscut $SrTiO_3$ substrate by two-step growth. (b) The atomic structure of a misfit dislocation at the $PrScO_3/SrTiO_3$ interface. The Burgers circuit was drawn around this misfit dislocation core.

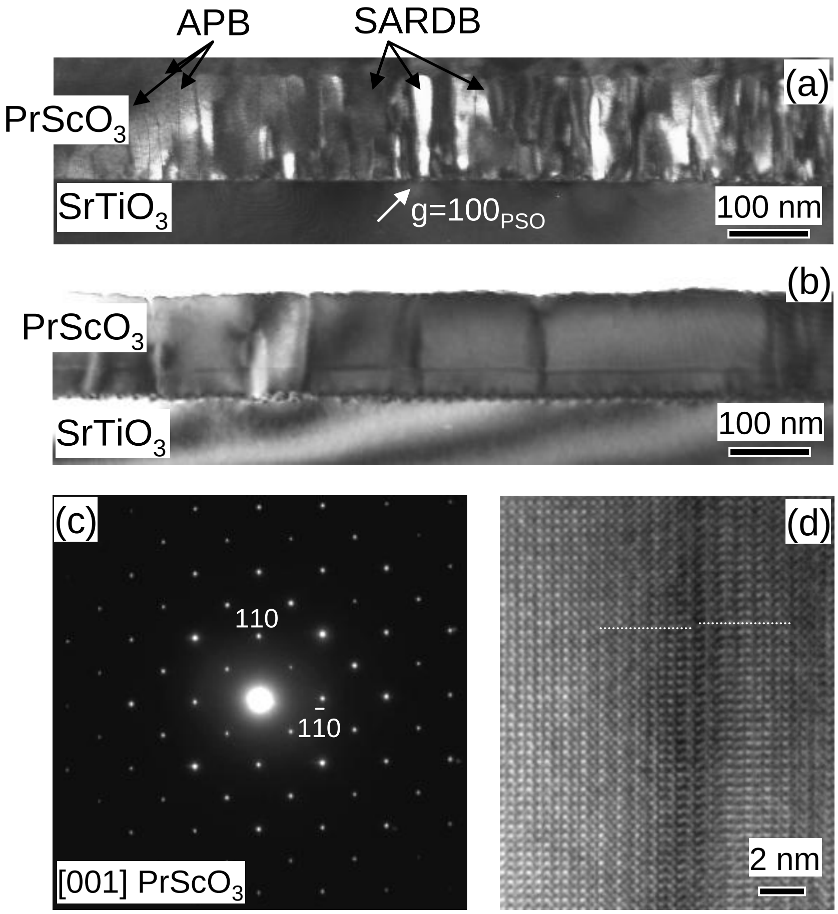

Fig. 5.4 (a) Dark-field image for 130 nm $PrScO_3$ thin films grown on 4° miscut $SrTiO_3$ substrates by direct growth. Antiphase boundary (APB) and small angle rotation domain boundaries (SARDB) are labeled in this micrograph. (b) The bright-field image for 100 nm $PrScO_3$ thin films grown on 4° miscut $SrTiO_3$ substrates by two-step growth. (c) The SAED pattern from $PrScO_3$ thin films showing there is only one type of domain. (d) The HRTEM micrograph for an antiphase boundary.

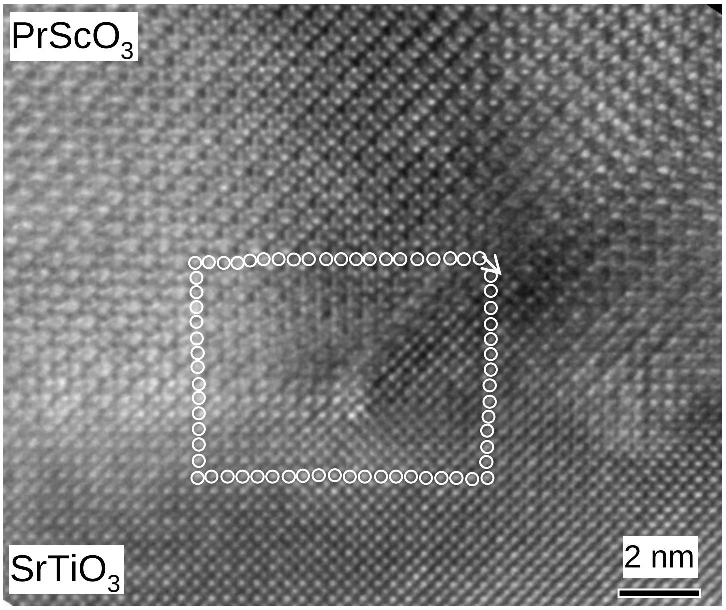

Fig. 5.5 The HRTEM image for a {011}-type anti-phase boundary bounded by a partial dislocation at the $PrScO_3$/$SrTiO_3$ interface.

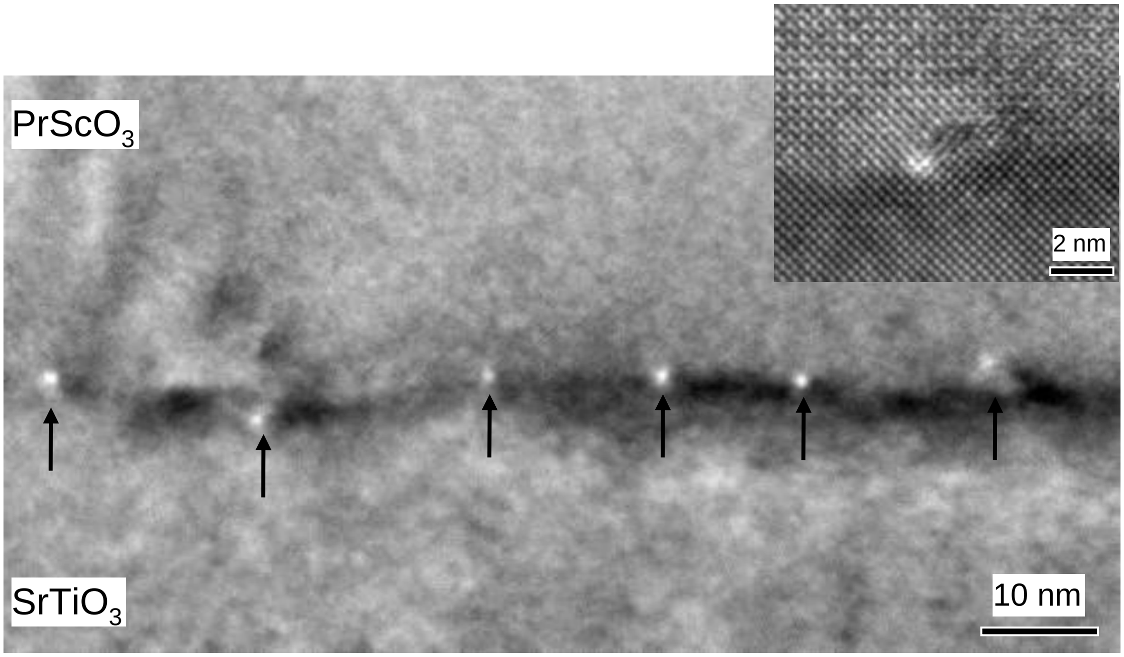

Fig. 5.6 The high-magnification image for periodic misfit dislocations at PrScO$_3$/SrTiO$_3$ interface on sample 100 nm PrScO$_3$ grown on 4° miscut SrTiO$_3$ substrate by two-step growth. Inset is the HRTEM image for a misfit dislocation.

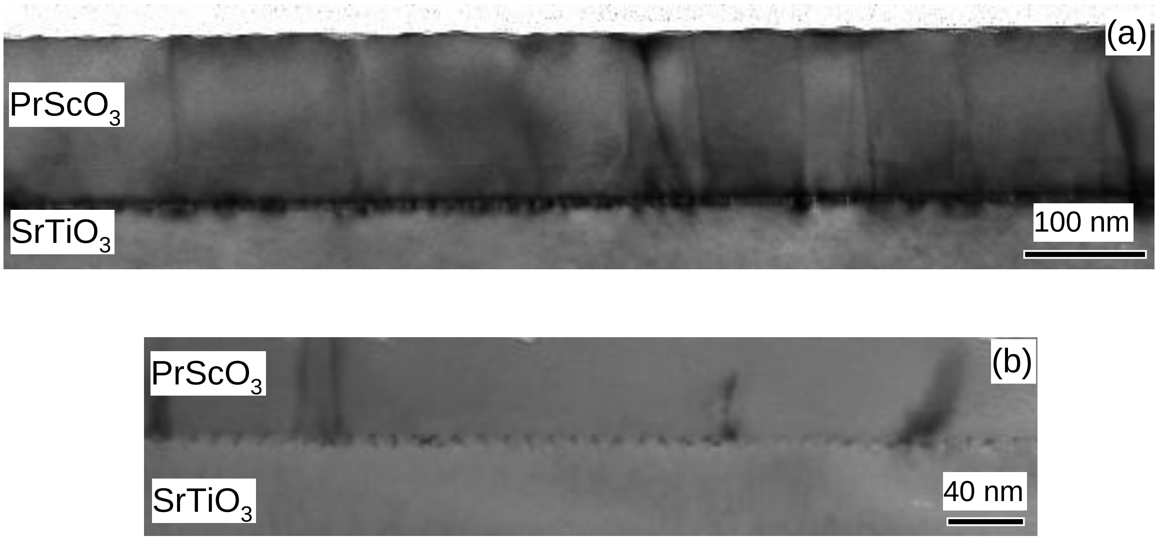

Fig. 5.7 (a) The bright-field image for 130 nm $PrScO_3$ thin film grown on 1° miscut $SrTiO_3$ substrate by two-step growth. (b) High-magnification image of periodic misfit dislocations at $PrScO_3/SrTiO_3$ interface.

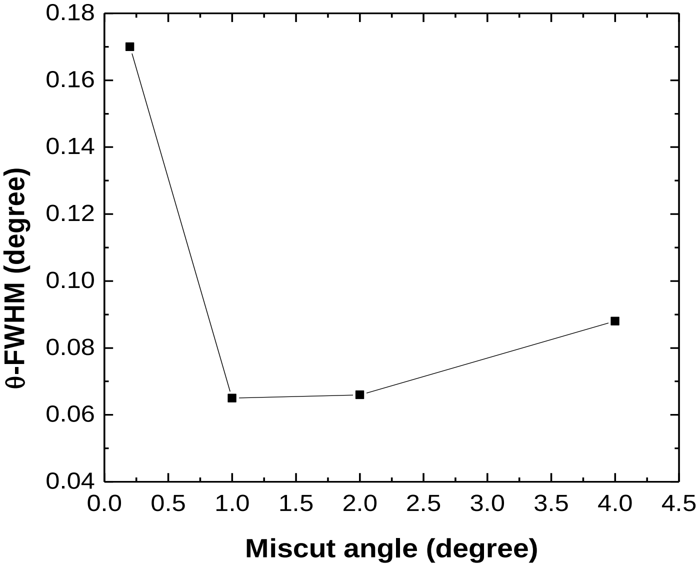

Fig. 5.8 The relationship between full-width at half maximum value of (220) pole in $PrScO_3$ thin films grown on miscut $SrTiO_3$ substrates and the miscut angle on $SrTiO_3$ substrates.

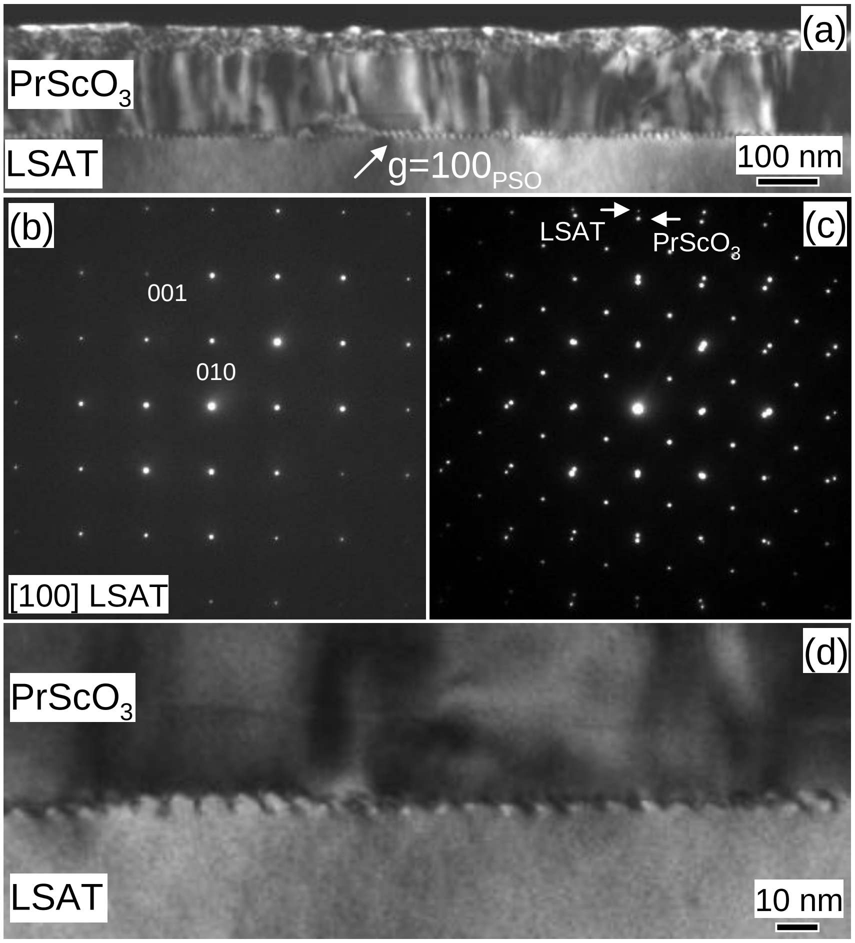

Fig. 5.9 (a) Dark field image of 100 nm $PrScO_3$ grown on 2° miscut LSAT substrate by two-step growth. (b) The SAED pattern from LSAT substrate. (c) SAED pattern taken from area covering the $PrScO_3$ thin film and LSAT substrate. (d) The high-magnification micrograph of periodic misfit dislocations generated at interface between $PrScO_3$ and LSAT substrate.

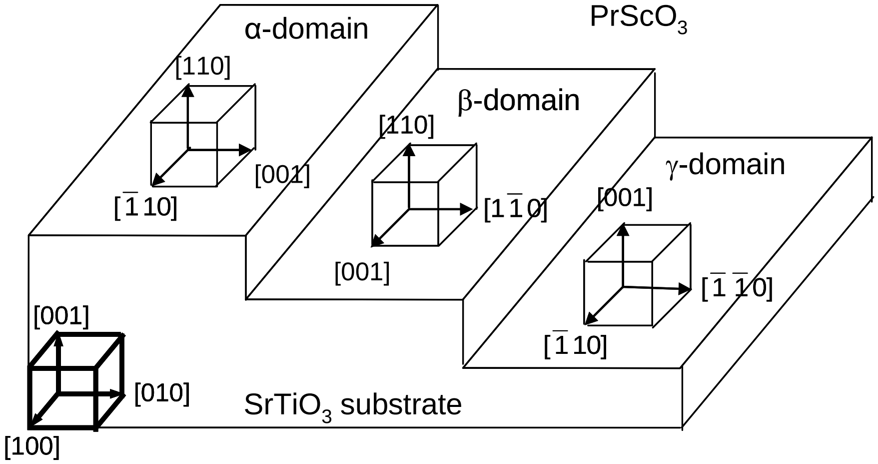

Fig. 5.10 A schematic showing the three different crystallographic domain configurations in $PrScO_3$ thin films grown on miscut $SrTiO_3$ substrate. The orientation relationship between different domains and substrate was explained in the text.

5.7. References:

[1] S. G. Lim, S. Kriventsov, T. N. Jackson, J. H. Haeni, D. G. Schlom, A. M. Balbashov, R. Uecker, P. Reiche, J. L. Freeouf, and G. Lucovsky, "Dielectric functions and optical bandgaps of high-k dielectrics for metal-oxide-semiconductor field-effect transistors by far ultraviolet spectroscopic ellipsometry," J. Appl. Phys., **91**, 4500 (2002).

[2] C. Zhao, T. Witters, B. Brijs, H. Bender, O. Richard, M. Caymax, T. Heeg, J. Schubert, V. V. Afanasev, A. Stesmans, and D. G. Schlom, "Ternary rare-earth metal oxide high-k layers on silicon oxide," Appl. Phys Lett., **86**, 132903 (2005).

[3] R. Thomas, P. Ehrhart, M. Luysberg, M. Boese, R. Waser, M. Roeckerath, E. Rije, J. Schubert, S. V. Elshocht, and M. Caymax, "Dysprosium scandate thin films as an alternate amorphous gate oxide prepared by metal-organic chemical vapor deposition," Appl. Phys. Lett., **89**, 232902 (2006).

[4] V. V. Afanasev, A. Stesmans, C. Zhao, M. Caymax, T. Heeg, J. Schubert, Y. Jia, D. G. Schlom, and G. Lucovsky, "Band alignment between (100) Si and complex rare earth/transition metal oxides," Appl. Phys. Lett., **85**, 5917 (2004).

[5] V. V. Afanasev, A. Stesmans, L. F. Edge, D. G. Schlom, T. Heeg, and J. Schubert, "Band alignment between (100) Si and amorphous $LaAlO_3$, $LaScO_3$, and Sc_2O_3: atomically abrupt versus interlayer-containing interfaces," Appl. Phys. Lett., **88**, 032104 (2006).

[6] M. Wagner, T. Heeg, J. Schubert, St. Lenk, S. Mantl, C. Zhao, M. Caymax, and S. De. Gendt, "Gadolinium scandate thin films as an alternative gate dielectric prepared by electron beam evaporation," Appl. Phys. Lett, **88**, 172901 (2006).

[7] K. H. Kim, D. B. Farmer, J. M. Lehn, P. Venkateswara Rao, and R. G. Gordon, "Atomic layer deposition of gadolinium scandate films with high dielectric constant and low leakage current," Appl. Phys. Lett., **89**, 133512 (2006).

[8] L. F. Edge, D. G. Schlom, S. Rivillon, Y. J. Chabal, M. P. Agustin, S. Stemmer, T. Lee, M. J. Kim, H. S. Craft, J. P. Maria, M. E. Hawley, B. Hollander, J. Schuber, and K. Eisenbeiser, "Thermal stability of amorphous $LaScO_3$ films on silicon," Appl. Phys. Lett., **89**, 062902 (2006).

[9] T. Heeg, J. Schubert, C. Buchal, E. Cicerrella, J. L. Freeouf, W. Tian, Y. Jia, and D. G. Schlom, "Growth and properties of epitaxial rare-earth scandate thin films," Appl. Phys. A: Mater. Sci. & Process., **83**, 103 (2006).

[10] H. M. Christen, G. E. Jellison, Jr, I. Ohkubo, S. Huang, M. E. Reeves, E. Cicerrella, J. L. Freeouf, Y. Jia, and D. G. Schlom, "Dielectric and optical properties of epitaxial rare-earth scandate films and their crystallization behavior," Appl. Phys. Lett., **88**, 262906 (2006).

[11] T. Heeg, M. Roeckerath, J. Schubert, W. Zander, C. Buchal, H. Y. Chen, C. L. Jia, Y. Jia, C. Adamo, and D. G. Schlom, "Epitaxial stabilized growth of orthorhombic $LuScO_3$ thin films," Appl. Phys. Lett., **90**, 192901 (2007).

[12] J. Schubert, O. Trithaveesak, A. Petraru, C. L. Jia, R. Uecker, P. Reiche, and D. G. Schlom, "Structural and optical properties of epitaxial $BaTiO_3$ thin films grown on $GdScO_3$ (110)", Appl. Phys. Lett., **82**, 3460 (2003).

[13] S. Karimoto, and M. Naito, "Electron doped infinite-layer thin films with T_c over 40 K grown on $DyScO_3$ substrate," Appl. Phys. Lett., **84**, 2136 (2004).

[14] J. H. Haeni, P. Irvin, W. Chang, R. Uecker, P. Reiche, Y. L. Li, S. Choudhury, W. Tian, M. E. Hawley, B. Craigo, A. K. Tagantsev, X. Q. Pan, S. K. Streiffer, L. Q. Chen, S. W. Kirchoefer, J. Levy, and D. G. Schlom, "Room-temperature ferroelectricity in strained $SrTiO_3$," Nature, **430**, 758 (2004).

[15] M. D. Biegalski, Y. Jia, D. G. Schlom, S. T. Mckinstry, S. K. Streiffer, V. Sherman, R. Uecker, and P. Reiche, "Relaxor ferroelectricity in strained epitaxial $SrTiO_3$ thin films on $DyScO_3$ substrates," Appl. Phys. Lett., **88**, 192907 (2006).

[16] M. D. Biegalski, J. H. Haeni, S. Trolier-Mckinstry, D. G. Schlom, C. D. Brandle, and A. J. Ven Graitis,"Thermal expansion of the new perovskite substrates $DyScO_3$ and $GdScO_3$," J. Mater. Res., **20**, 952 (2005).

[17] K. J. Choi, M. Biegalski, Y. L. Li, A. Sharan, J. Schubert, R. Uecker, P. Reiche, Y. B. Chen, X. Q. Pan, V. Gopalan, L. -Q. Chen, D. G. Schlom, and C. B. Eom, "Enhancement of ferroelectricity in strained $BaTiO_3$ thin films," Science, **306**, 1005 (2004).

[18] S. Geller, Acta Cryst. "Crystallographic studies of perovskite-like compounds. IV. Rare earth scandates, vanadites, galliates, orthochromites," Acta Cryst., **10**, 243 (1957).

[19] C. M. Folkman, R. R. Das, C. B. Eom, Y. B. Chen, and X. Q. Pan, "Single domain strain relaxed $PrScO_3$ template on miscut substrates," Appl. Phys. Lett., **89**, 221904, (2006).

[20] D. G. Schlom, L.-Q. Chen, C. B. Eom, K. M. Rabe, S. K. Streiffer, and J. M. Triscone, "Strain tuning of ferroelectric thin films," Annu. Rev. Res., **37**, 589 (2007).

[21] Y. B .Chen, M. B. Katz, X. Q. Pan, C. M. Folkman, R. R. Das, and C. B. Eom,"Microstructure and strain relaxation of epitaxial $PrScO_3$ thin fims grown on (001) $SrTiO_3$ substrates," Appl. Phys. Lett., **91**, 031902 (2007).

[22] C. Ratsch, J. Garcia, and R. E. Caflisch, "Influence of edge diffusion on the growth mode on vicinal surfaces," Appl. Phys. Lett., **87**, 141901 (2005).

[23] Q. Gan, R. A. Rao, and C. B. Eom, "Control of the growth and domain structure of epitaxial $SrRuO_3$ thin films by vicinal (001) $SrTiO_3$ substrates," Appl. Phys. Lett., **70**, 1962 (1997).

[24] J. C. Jiang, W. Tian, X. Pan, Q. Gan, and C. B. Eom, "Effects of miscut of the $SrTiO_3$ substrate on microstructures of the epitaxial $SrRuO_3$ thin films," Mater. Sci. & Engin. B, **56**, 152 (1998).

[25] S. D. Bu, M. K. Lee, C. B. Eom, W. Tian, X. Q. Pan, S. K. Streiffer, and J. J. Krajewski, "Perovskite phase stabilization in epitaxial $Pb(Mg_{1/3}Nb_{2/3})O_3$-$PbTiO_3$ films by deposition onto vicinal (001) $SrTiO_3$ substrates," Appl. Phys. Lett., **79**, 3482 (2001).

[26] J. M. Dekkers, G. Rijnders, S. Harkema, H. J. H. Smilde, H. Hilgenkamp, H. Rogalla, and D. H. A. Blank, "Monocrystalline $YBa_2Cu_3O_{7-x}$ thin films on vicinal $SrTiO_3$ (001) substrates," Appl. Phys. Lett, **83**, 5199 (2003).

[27] J. C. Jiang, and X. Q. Pan, "Structural phase transitions in epitaxial $SrRuO_3$ thin films," Philo. Mag. Lett., **80**, 271 (2000).

[28] H. P. Sun, W. Tian, X. Q. Pan, J. H. Haeni, and D. G. Schlom, "Evolution of dislocation arrays in epitaxial $BaTiO_3$ thin films grown on (100) $SrTiO_3$," Appl. Phys. Lett., **84**, 3298 (2004).

[29] T. Suzuki, Y. Nishi, and M. Fujimoto, "Analysis of misfit relaxation in heteroepitaxial $BaTiO_3$ thin films," Philos. Mag. A, **79**, 2461 (1999).

[30] D. Su, T. Yamada, V. O. Sherman, A. K. Tagantsev, P. Muralt, and N. Setter, "Annealing effect on dislocations in $SrTiO_3$/$LaAlO_3$ heterostructures," J. Appl. Phys., **101**, 064102 (2007).

CHAPTER 6

SUMMARY AND FUTURE WORK

The microstructure of strain-engineered and ferroelectric/crystallographic-domain-engineered perovskite oxide thin films has been studied by transmission electron microscopy (TEM). There are three major material systems studied in this thesis: 1) Ferroelectric domain-engineered $BiFeO_3$ thin films can be realized by means of miscut $SrTiO_3$ substrates. 2) Coherent/strain partially-relaxed $BaTiO_3$ and $SrRuO_3$ bottom electrodes were grown on small lattice-mismatched substrates, $GdScO_3$ and $DyScO_3$, by pulsed laser deposition. 3) Strain-relaxed, single-domain $PrScO_3$ templates were successfully grown on commercially available high angle (≥1°) miscut $SrTiO_3$ substrates. Several materials science issues surrounding these materials have been studied by TEM and phenomenological thermodynamic theory.

Ferroelectric domains in multiferroic $BiFeO_3$ thin films can be engineered via the employment of high-angle miscut $SrTiO_3$ substrates. $BiFeO_3$ thin films grown on low-angle miscut (miscut angle <1°) $SrTiO_3$ comprise the perovskite $BiFeO_3$ phase and the α-type Fe_2O_3 secondary phase. The orientation relationship between perovskite $BiFeO_3$ and the α-type Fe_2O_3 secondary phase was determined by electron diffraction. In addition, electron diffraction and high-resolution TEM show that the $BiFeO_3$ thin films grown on low-angle miscut $SrTiO_3$ substrates are composed of 109° and 71° ferroelectric domains while those grown on high-angle (4°) miscut $SrTiO_3$ substrates comprise only 71° ferroelectric lamellar domains. Ferroelectric hysteresis measurements show that the saturated spontaneous polarization in $BiFeO_3$ thin films grown on 4° miscut $SrTiO_3$ substrates is higher than that of $BiFeO_3$ thin films grown on 0.8° miscut $SrTiO_3$ substrates. This lower spontaneous polarization is related to domain pinning at the 71° and 109° ferroelectric domain boundaries. In addition, the domain width of 71° domains has a simple square root relation to thin film thickness. Compared with theoretical results, 71° and 109° domain energies can be extracted via a fitting parameter.

Strain-engineered $BaTiO_3$ thin films can be realized by means of newly developed substrates ($GdScO_3$ and $DyScO_3$) grown by Czochralski method. These substrates impose the compressive strain in $BaTiO_3$ thin films which are grown upon them. Crystallographic study shows that the lattice mismatches between $BaTiO_3$ and $GdScO_3$ and $DyScO_3$ substrates are as small as 0.5 and 1.2 %, respectively. Moreover, the thermal expansion coefficients in these substrates are closely matched to those of $BaTiO_3$. Because of the unique combination of these two properties, $BaTiO_3$ with $SrRuO_3$ electrodes can be grown coherently on $GdScO_3$ and $DyScO_3$ substrates. However, with increased thicknesses of the $BaTiO_3$ layer, strain-partially relaxed $BaTiO_3$ thin films grown on $DyScO_3$ substrate have also been observed. Strain relaxation in $BaTiO_3$/$SrRuO_3$ hetero-structures grown on $GdScO_3$, $DyScO_3$ and $SrTiO_3$ substrates is discussed by thermodynamic theory. Results show that the major factors determining the strain relaxation in hetero-structure are the thickness of each layer, as well as lattice mismatch between each layer and substrate. Spontaneous polarization in strained $BaTiO_3$ thin films grown on $GdScO_3$ substrates are triple those of its bulk counterpart, as observed in ferroelectric hysteresis measurements. In addition the Curie temperatures in coherent $BaTiO_3$ thin films grown on $GdScO_3$ and $DyScO_3$ substrates can be increased to 400 °C and 540 °C, respectively, compared with Curie temperature of 120 °C in its bulk counterpart. These enhanced ferroelectric properties were correlated with the observed microstructure.

$PrScO_3$, another rare-earth scandate substrate, provides tensile strain in coherent $BaTiO_3$ thin films. $PrScO_3$ single crystals, however, cannot be grown by conventional Czochralski method due to high melting temperature (2100 °C) and non-congruency at the melting temperature. Strain relaxed $PrScO_3$ template grown on $SrTiO_3$ substrates is an alternative to a bulk $PrScO_3$ substrate. In this work, strain relaxed, single domain $PrScO_3$ templates were grown on high-angle miscut $SrTiO_3$ substrates. In comparison to the $PrScO_3$ thin films grown on high-angle miscut $SrTiO_3$ substrates, there are six types of crystallographic domains in $PrScO_3$ thin films grown on low-angle miscut $SrTiO_3$ substrates. The orientation relationship between different crystallographic domains and the substrate is determined. The growth of preferential domain in $PrScO_3$ thin films on high-angle miscut $SrTiO_3$ substrates is discussed in terms of minimization of interfacial energy.

Future work will be focused on growing coherent $BaTiO_3$ thin films on high crystalline $PrScO_3$ templates. As predicted by thermodynamics calculation, coherent $BaTiO_3$ thin films grown on $PrScO_3$ templates show a spontaneous polarization in the a-b plane. It will be very interesting to characterize the ferroelectric domain structures in tensile strained $BaTiO_3$ thin films and to study the strain relaxation phenomena in this system. We expect to measure the dielectric constant, dielectric loss and dielectric tunability in these tensile strained $BaTiO_3$ films. To measure ferroelectric properties, we only need to use a top electrode because the spontaneous polarization is along the a-b plane. The top electrode used in electric characterization is inter-digital finger electrode. The corresponding metal electrode should be fabricated in a clean-room. As to the extension of the ferroelectric domain-engineered project, we expect to apply this method to other multiferroic materials, such as $BiMnO_3$ and $YMnO_3$. Previous results show that the spontaneous polarization in these materials ($< 10\ \mu C/cm^2$) is much smaller than that in $BiFeO_3$, but their magnetic properties are superior to those of $BiFeO_3$. An improvement in the ferroelectric properties of domain-engineered $BiMnO_3$ and $YMnO_3$ thin films can be expected. Combining good magnetic properties and enhanced ferroelectric property, $BiMnO_3$/$YMnO_3$ thin films can be developed for memory devices based on multiferroic properties. The long-term goal is to integrate these domain-engineered functional materials with Si-based semiconductor devices, such as dynamic random access memory, microelectronic devices and microelectromechanical systems (MEMS).